

Development and evaluation of 3D-printed  
anthropomorphic phantoms for application in diagnostic  
and interventional X-ray imaging

# Dissertation

zur Erlangung des Doktorgrades der Naturwissenschaften  
(Dr. rer. nat.)

der

Naturwissenschaftlichen Fakultät II  
Chemie, Physik und Mathematik

der Martin-Luther-Universität  
Halle-Wittenberg

vorgelegt von

**Frau Patrizia Kunert**

München, den 21. August 2023

Gutachter:

1. Prof. Dr. Detlef Reichert
2. Prof. Dr. Gunnar Brix
3. Prof. Dr. Klemens Zink

Tag der Verteidigung: 22. Februar 2024

Vorsitzende der Promotionskommission: Prof. Dr. Thorid Rabe

---

# Contents

<b>List of Figures</b>	<b>VI</b>
<b>List of Tables</b>	<b>VII</b>
<b>Abbreviations</b>	<b>IX</b>
<b>Abstract</b>	<b>XIII</b>
Zusammenfassung . . . . .	XIV
<b>1 Introduction</b>	<b>1</b>
1.1 Motivation . . . . .	1
1.1.1 Research aim . . . . .	2
1.2 State of the art . . . . .	2
<b>2 Theoretical background</b>	<b>5</b>
2.1 X-Rays . . . . .	5
2.2 Generation of X-rays . . . . .	6
2.2.1 Interaction of accelerated electrons with matter . . . . .	6
2.2.1.1 Bremsstrahlung . . . . .	6
2.2.1.2 Characteristic X-rays . . . . .	7
2.2.2 Stopping power . . . . .	7
2.2.3 X-ray tubes . . . . .	9
2.3 Radioactivity . . . . .	10
2.4 Interaction of photons with matter . . . . .	11
2.4.1 Photoelectric effect . . . . .	12
2.4.2 Compton scattering . . . . .	13
2.4.3 Rayleigh scattering . . . . .	14
2.4.4 Pair production . . . . .	15
2.5 Interaction of secondary electrons with matter . . . . .	15
2.6 Interaction of ionizing radiation with biological tissues . . . . .	16

2.7	Computed Tomography . . . . .	17
2.7.1	Hounsfield unit scale . . . . .	19
2.8	Dosimetry . . . . .	20
2.8.1	Fundamental dosimetry quantities . . . . .	20
2.8.2	Dosimeter . . . . .	23
2.8.2.1	Ionization chambers . . . . .	23
2.8.2.2	Thermoluminescence dosimetry . . . . .	24
2.9	Monte-Carlo methods . . . . .	26
2.10	Phantoms . . . . .	27
2.10.1	Standardized phantoms . . . . .	28
2.10.2	Anthropomorphic phantoms . . . . .	28
2.10.3	Computational phantoms . . . . .	29
2.11	3D-printing methods . . . . .	31
2.11.1	General workflow . . . . .	31
2.11.2	Stereolithography . . . . .	32
2.11.3	Fused deposition modelling . . . . .	33
2.11.4	Polyjet 3D-printing . . . . .	33
<b>3</b>	<b>Tissue equivalence of 3D-printing materials</b>	<b>35</b>
3.1	State of the art . . . . .	35
3.2	Materials and methods . . . . .	37
3.2.1	Choice of materials and sample preparations . . . . .	37
3.2.1.1	Hydroxyapatite-resin mixtures . . . . .	40
3.2.2	Investigation of attenuation properties . . . . .	41
3.2.2.1	Determination of apparent kerma attenuation coefficients . . . . .	42
3.2.3	Investigation of absorption properties . . . . .	43
3.2.4	TLD processing . . . . .	44
3.2.5	Monte-Carlo simulations for obtaining tissue reference values . . . . .	45
3.2.6	Conditions for tissue equivalence . . . . .	47
3.2.7	Validation process . . . . .	47
3.2.8	Analysis of CT densities . . . . .	48
3.2.8.1	Influence of printing settings . . . . .	49
3.3	Results . . . . .	50
3.3.1	Validation process for the assessment of the tissue equivalence . . . . .	50

3.3.2	Overview of attenuation and absorption properties . . . . .	52
3.3.2.1	Non-printed polymers and different manufacturers . . . . .	54
3.3.3	Individual evaluation of tissue equivalence . . . . .	55
3.3.4	Analysis of CT densities . . . . .	64
3.3.4.1	Influence of printing settings on CT densities of printed samples . . . . .	66
3.4	Discussion . . . . .	67
<b>4</b>	<b>Comparison of 3D-printed and conventionally produced phantom parts</b>	<b>71</b>
4.1	State of the art . . . . .	71
4.2	Materials and methods . . . . .	73
4.2.1	Reproduction of a conventional anthropomorphic female thorax phantom slice and breast add-ons . . . . .	73
4.2.2	Comparison of image contrasts and absorbed doses in CT . . . . .	76
4.3	Results . . . . .	78
4.3.1	Comparison of the geometry . . . . .	78
4.3.2	Comparison of image contrasts . . . . .	79
4.3.3	Comparison of absorbed doses . . . . .	81
4.4	Discussion . . . . .	81
<b>5</b>	<b>Individualized 3D-printed phantoms</b>	<b>85</b>
5.1	State of the art . . . . .	85
5.2	Production of a patient-specific breast phantom . . . . .	87
5.2.1	Materials and methods . . . . .	87
5.2.1.1	Imaging of the patient-specific breast phantom . . . . .	88
5.2.2	Results . . . . .	88
5.3	Production of an abdomen phantom of a female in 25. week of pregnancy . . . . .	90
5.3.1	Materials and methods . . . . .	90
5.3.1.1	Production of the phantom add-on . . . . .	90
5.3.1.2	Whole-body CT examination on the physical phantom of a pregnant female . . . . .	92
5.3.1.3	Simulation of the whole-body CT examination using computational phantoms . . . . .	94
5.3.2	Results . . . . .	98
5.3.2.1	Imaging properties of the physical phantom . . . . .	100

5.3.2.2	Dose estimation for a whole-body CT examination on physical and computational phantoms . . . . .	100
5.4	Discussion . . . . .	104
<b>6</b>	<b>Conclusion</b>	<b>107</b>
	<b>Bibliography</b>	<b>111</b>
<b>7</b>	<b>Appendix</b>	<b>127</b>
<b>8</b>	<b>Curriculum Vitae</b>	<b>129</b>
8.1	List of publications . . . . .	130
<b>9</b>	<b>Danksagung</b>	<b>131</b>

---

# List of Figures

2.1	The electromagnetic spectrum . . . . .	5
2.2	X-ray spectrum . . . . .	7
2.3	Stopping-power of electron radiation for aluminium . . . . .	8
2.4	Schematic X-ray tube . . . . .	9
2.5	Mass attenuation coefficients for aluminium . . . . .	12
2.6	Construction schema of a CT-scanner . . . . .	17
2.7	Thermoluminescence process . . . . .	25
2.8	Physical phantoms . . . . .	27
2.9	Computational phantoms . . . . .	29
2.10	3D-printing methods . . . . .	31
2.11	Workflow for 3D-printing . . . . .	32
3.1	Sample design for material characterization . . . . .	38
3.2	Elemental mass fraction of hydroxyapatite-resin mixtures . . . . .	41
3.3	Experimental setup for investigation of attenuation properties . . . . .	42
3.4	Experimental setup for investigation of absorption properties . . . . .	44
3.5	Cubic samples with different infill densities . . . . .	49
3.6	Validation results . . . . .	51
3.7	Overview of attenuation and absorption properties of 3D-printing materials and human tissues . . . . .	53
3.8	Analysis of lung tissue equivalence . . . . .	55
3.9	Linear correlation between mass densities and AKAC values . . . . .	56
3.10	Analysis of adipose tissue equivalence . . . . .	57
3.11	Analysis of muscle and bulk soft tissue equivalence . . . . .	58
3.12	Analysis of spongiosa equivalence . . . . .	60
3.13	Analysis of cortical bone equivalence . . . . .	61
3.14	Mean CT densities of investigated 3D-printing materials . . . . .	65
3.15	CT densities in dependence of different printing settings . . . . .	66

4.1	Production of a 3D-printed phantom slice . . . . .	74
4.2	Production of a 3D-printed breast add-on . . . . .	76
4.3	Phantom portion investigated in a CT examination . . . . .	77
4.4	Reproduced phantom parts . . . . .	78
4.5	CT images of reproduced phantom parts . . . . .	80
4.6	Comparison of dose values measured inside printed and conventionally produced phantom parts . . . . .	82
5.1	Production of a 3D-printed patient-specific breast phantom . . . . .	87
5.2	Patient-specific breast phantom . . . . .	89
5.3	Production of a 3D-printed phantom of a pregnant female . . . . .	91
5.4	Whole-body CT examination on a phantom of a pregnant female . .	93
5.5	Voxel phantoms of pregnant females . . . . .	97
5.6	Implementation of the UFPF25WK phantom . . . . .	98
5.7	3D-printed abdomen add-on of a female in 25. week of pregnancy . .	99
5.8	Organ doses for a whole-body examination on different phantoms of pregnant females . . . . .	102

---

# List of Tables

2.1	Radiation weighting factors . . . . .	22
2.2	Tissue weighting factors . . . . .	22
3.1	3D-printing filaments for the investigation of the tissue equivalence . . . . .	39
3.2	Elemental composition of simulated reference tissues . . . . .	46
3.3	Sample series for the investigation of the influence of printing settings on the CT densities of printed samples . . . . .	50
3.4	Summary of relative differences of attenuation and absorption values for 3D-printing materials and soft tissues . . . . .	63
3.5	Summary of relative differences of attenuation and absorption values for 3D-printing materials and bone compositions . . . . .	64
4.1	General printing settings for the production of a 3D-printed phantom slice . . . . .	74
4.2	Material-specific printing settings for the production of a 3D-printed phantom slice . . . . .	75
4.3	Mean CT densities of phantom parts . . . . .	81
5.1	Dose parameter for the whole-body examination on the phantom of a pregnant female . . . . .	93
5.2	Characterization of voxel phantoms . . . . .	96
5.3	Effective doses for a whole-body examination . . . . .	100
7.1	Print settings used for material samples for the investigation of tissue equivalence . . . . .	127
7.2	Organ doses for a whole-body CT examination on different phantoms of pregnant females . . . . .	128



---

# Abbreviations

**3D** three dimensional

**ABS** acrylonitrile butadine styrene

**AKAC** apparent Kerma attenuation coefficient

**Al** aluminium

**ALARA** as low as reasonable achievable

**AM** additive manufacturing

**Be** beryllium

**Ca** calcium

**CAD** computer aided design

**CPU** central processing units

**CT** computed tomography

**CTDI** computed tomography dose index

**Cu** copper

**DLP** dose length product

**DNA** deoxyribonucleic acid

**FBP** filtered back projection

**FDM** fused deposition modelling

**FOV** field of view

**FWHM** full width half maximum

**GSF** Gesellschaft für Strahlenforschung

**HIPS** high impact polystyrene

**HU** Hounsfield unit

**ICRP** International Commission on Radiological Protection

**ICRU** International Commission on Radiation Units and Measurements

**IR** iterative reconstruction

**Kerma** kinetic energy released per unit mass

**LET** linear energy transfer

**LiF** lithium fluoride

**MC** Monte-Carlo

**MR** magnetic resonance

**NIST** National Institute of Standards and Technology

**NURBS** non-uniform rational B-spline

**Pb** lead

**PE** polyethylene

**PET** positron emission tomography

**PETG** polyethylenterephthalat + glycole

**PLA** polylactide

**PMMA** polymethyl methacrylate

**PVA** polyvinyl alcohol

**ROI** region of Interest

**SLA** stereolithography

**SPECT** single photon emission computed tomography

**stl** standard tessellation language

**TLD** thermoluminescence dosimeter

**TPU** thermoplastic Polyurethane

**UV** ultraviolet

**W** tungsten



---

# Abstract

Because of their realistic imitation of the human body, anthropomorphic phantoms are essential in medical physics to estimate image quality and dose distributions. Conventional anthropomorphic phantoms do not represent persons with atypical body dimensions. Therefore, the approach to produce individualized phantoms by three dimensional (3D) printing methods is promising. This thesis aims to evaluate the quality of 3D-printed phantoms in several aspects on the example of X-rays typically used for diagnostic and interventional imaging.

In a preliminary study, a large number of samples printed with conventional fused deposition modelling (FDM) filaments and different print settings were characterized for their tissue equivalence in terms of attenuation and absorption of X-rays. Based on these results, phantom parts were produced and compared to conventionally produced anthropomorphic phantoms for their image quality and dose distribution in the example of a typical computed tomography (CT) examination. In the last step, individualized phantoms were produced. In example of the phantom of a pregnant female, which was constructed based on a computational mesh phantom, another validation step was performed by comparing measured dose distributions for a whole-body CT examination with simulation results on virtual pregnancy phantoms.

Except for cortical bone, materials with equivalent attenuation and absorption behaviour were found for all relevant kinds of tissues. The 3D-printed phantom parts were with exception of minor contrast differences equal to the conventional ones in their imaging and dose distribution properties. The dose distribution for a CT examination of a pregnant female measured in the 3D-printed replication of a virtual phantom could also be validated by computer simulations.

3D-printed phantoms are suited to quantify the image contrast and dose distribution as in human patients for diagnostic and interventional imaging. Therefore, the methods can be used for the production of phantoms with individualized anatomy to investigate specific issues in the field of radiation protection for vulnerable patient groups not adequately represented by conventional anthropomorphic phantoms.

## **Zusammenfassung**

Aufgrund ihrer realistischen Nachbildung des menschlichen Körpers sind anthropomorphe Phantome für die medizinische Physik essenziell zur realistischen Bestimmung von Bildqualität und Dosis-Verteilungen. Da konventionelle Phantome Personen mit außergewöhnlichen Körpermaßen nicht ausreichend repräsentieren ist der Ansatz der Herstellung individualisierter Phantome mittels 3D-Druck-Technologien vielversprechend. Ziel dieser Arbeit war es, die Qualität von 3D-gedruckten Phantomen in unterschiedlichen Aspekten am Beispiel für Röntgenanwendungen in der diagnostischen und interventionellen Bildgebung zu bewerten.

In einer anfänglichen Studie wurde eine große Anzahl an Proben, die mit unterschiedlichen konventionell erhältlichen FDM Materialien und unterschiedlichen Druckeinstellungen hergestellt wurden, auf ihre Gewebeäquivalenz hinsichtlich ihrer Schwächungs- und Absorptionseigenschaften untersucht. Aufbauend auf diesen Ergebnissen wurden anthropomorphe Phantomteile produziert und bezüglich ihrer Bildqualität und Dosisverteilung bei einer typischen CT-Untersuchung mit konventionell hergestellten Phantomen verglichen. Abschließend wurden individualisierte Phantome hergestellt, unter anderem das Phantom einer schwangeren Frau, welches auf der Anatomie eines virtuellen Phantoms basierte, wodurch die gemessene Dosisverteilung bei einer CT-Untersuchung mit Simulationsergebnissen an virtuellen Phantomen direkt verglichen werden konnte.

Bis auf kortikalen Knochen konnten für alle relevanten Gewebearten Materialien mit äquivalenten Eigenschaften in Schwächung und Absorption von Röntgenstrahlung gefunden werden. Die 3D-gedruckten Phantomteile lieferten bis auf kleinere Unterschiede im Gewebekontrast gleichwertige Ergebnisse bezüglich Bildqualität und Dosis wie die konventionell hergestellten, und können somit äquivalent zueinander verwendet werden. Die im 3D-gedruckten Schwangerschafts-Phantom gemessene Patientenexposition während einer CT-Untersuchung konnte ebenfalls mittels Simulationen am virtuellen Phantom mit gleicher Anatomie validiert werden.

3D-gedruckte Phantome sind gut geeignet, um die Bildqualität und Dosisverteilung im Patienten für Anwendungen in der diagnostischen und interventionellen Bildgebung zu quantifizieren. Diese Methoden können daher für die Herstellung von Phantomen mit individueller Anatomie verwendet werden, mit denen spezifische Fragestellungen zum Strahlenschutz von vulnerablen Patientengruppen, die von konventionellen Phantomen nicht repräsentiert werden, untersucht werden können.

---

# 1 Introduction

## 1.1 Motivation

The application of ionizing radiation for medical purposes requires adequate quality assurance of devices and methods and continuous improvement in efficiency and dose reduction to decrease the risks of radiation injury to the patients. For these tasks, phantoms are needed to replace the human body and to allow the direct measurement of image quality and absorbed dose.

Anthropomorphic phantoms are realistic imitations of human bodies in their anatomy and tissue composition. However, commercially available anthropomorphic phantoms represent standardized body sizes only. Especially overweighted and underweighted persons, children of different ages and body sizes, or pregnant persons in different states of gestation are not covered by these phantoms. Therefore, an adequate representation of this group of persons, which is subject to decisive radiation protection issues due to deviating imaging/treatment parameters or their sensitivity to harm due to ionizing radiation, is not possible with conventional anthropomorphic phantoms. In addition, anthropomorphic phantoms come with high acquisition costs (more than 10.000 €) and are rarely available in clinics and institutes.

To overcome this limitation 3D-printing technologies are promising for producing individualized anthropomorphic phantoms. The technologies allow the production of phantoms directly by researchers for low costs and in an acceptable time range tailored to specific anatomies or requirements. They may be suited to improve quality assurance and research regarding the application of ionizing radiation on vulnerable groups of patients not covered by conventional phantoms.

Similar to the conventional phantoms, the 3D-printed phantoms must meet the high requirements on the equivalence to the human body in terms of attenuation and absorption of ionizing radiation to ensure realistic results. Therefore, detailed quality assurance of the method of 3D-printed phantoms is necessary.

### 1.1.1 Research aim

This thesis aims to develop and to evaluate the possibilities for producing individualized phantoms with 3D-printing methods focusing on applications for diagnostic and interventional X-ray imaging. This includes the investigation of the tissue equivalence of commercially available 3D-printing materials in a preliminary study. Subsequently, the quality of 3D-printed phantom parts was assessed for a typical CT examination compared to conventional phantoms. Ultimately, individualized phantoms, i.e., a patient-specific breast phantom and the abdomen of a pregnant woman, were produced. For an additional validation step, the patient exposure during a typical CT examination, estimated with the phantom of a pregnant female, was compared with the dose estimations by Monte-Carlo (MC) simulations on similar computational phantoms.

Consequently, this thesis contains three main topics, organized in three chapters:

1. The tissue equivalence of 3D-printing materials,
2. the comparison of 3D-printed phantom parts with conventionally produced phantoms,
3. the development and quality assurance of individualized 3D-printed phantoms compared to simulated dose distributions in virtual reference phantoms.

This way, a comprehensive investigation of the quality of 3D-printed phantoms with a focus on applications of X-rays in the energy range typically used for diagnostic and interventional imaging is done, and general recommendations on the production methods for 3D-printed phantoms are given.

## 1.2 State of the art

Along with the boom of 3D-printing technologies in the maker community, starting around 2012, the technology has found its way into several fields of industry and science. For industry, 3D-printing offers the advantage of fast and cheap prototype production, improving development processes. Other application areas are medicine, biology, the space industry, the building industry, or the food industry [1–6].

In the field of medical physics, 3D-printing technologies are used for example for the production of bolus and beam modulators for radiotherapy individualized to the patient's anatomy [7, 8]. Another promising area of application is the production

of phantoms. Not surprisingly, the number of publications concerning 3D-printed phantoms has increased yearly since 2012.

The results of literature research concerning the thesis topics performed with the scientific databases Scopus and Google scholar are presented in the corresponding chapters.



---

## 2 Theoretical background

### 2.1 X-Rays

In 1895 a new kind of radiation was coincidentally discovered by Wilhelm C. Roentgen. It was detected in experiments with a vacuum tube when a fluorescence screen was activated through a cardboard shield. The ability to penetrate solid matter, depending on the density, was not known from any radiation so far. To distinguish the new kind of radiation from visible and UV light, he called it X-rays. Not long after that, Roentgen used X-rays to get a view into living bodies, which revolutionized medical diagnostics. Not surprisingly, he received the first physics Nobel prize in 1901 for his discovery [9].

Max von Laue's discovery of the interference of X-rays in crystals proved that they

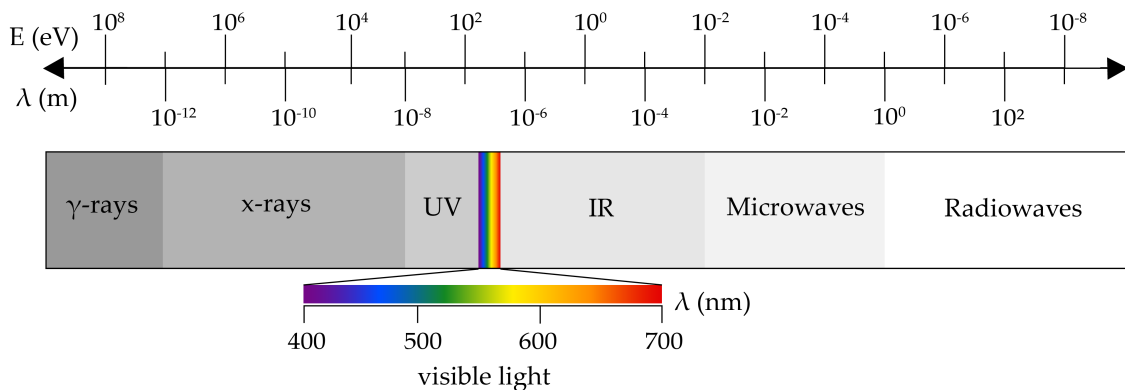


Figure 2.1: The electromagnetic spectrum with the typical energies and wavelengths.

belong to the electromagnetic wave spectrum [10]. In the electromagnetic spectrum X-rays are positioned between UV light and  $\gamma$ -radiation with wavelengths from 10 nm to 10 pm, as shown in Fig 2.1. In principle,  $\gamma$ -rays have the same wavelengths and cannot be distinguished from X-rays, depart from their origin. While X-rays arise from the interaction of accelerated electrons with a medium,  $\gamma$ -rays are released

in nuclear transformation processes of atoms. Both belong to the ionizing radiation, which is able to ionize atoms or molecules owing to its high energy.

According to Einstein's model of light quanta, called photons, the energy of one photon can be calculated with the Planck's constant  $h$ , the frequency  $\nu$ , the wavelength  $\lambda$  and the speed of light  $c$ : [11]

$$E = h \cdot \nu = h \cdot \frac{c}{\lambda} \quad (2.1)$$

## 2.2 Generation of X-rays

X-rays are typically generated in vacuum tubes, where accelerated electrons interact with anode materials. The physical background of this process and the general design of X-ray tubes are described in the following section.

### 2.2.1 Interaction of accelerated electrons with matter

The interactions between electrons and anode atoms are Coulomb interactions of the electrical field of the electron, either with the field of the atoms' inner-shell electrons or the Coulomb field of the nucleus. The type of interaction is determined by the atomic radius and the impact parameter that describes the distance between the asymptotic track of the electron and the interacting atom. Interactions are called hard collisions if impact parameters are of the same magnitude as the atomic radius. For impact parameters far above the atomic radius, interactions are called soft collisions.

#### 2.2.1.1 Bremsstrahlung

During deceleration of a charged particle (most prominent are electrons or positrons) in an electric field, e.g., the one of the atomic electrons or the nuclei of the anode material (the latter is the case when impact parameters are far below the atomic radius), the particle loses kinetic energy which is emitted as a photon, called bremsstrahlung. This process also occurs when charged particles change their direction, i.e., in the magnetic field of a synchrotron. The energy of the photon depends on the impact parameter. It can take on any values up to the total energy of the accelerated electron, which is the case when the electron loses its entire kinetic energy. Therefore, the energy distribution of the bremsstrahlung in the X-ray spectrum is continuously

with the highest energy equal to the electrons energy.

### 2.2.1.2 Characteristic X-rays

For the inelastic interaction of accelerated electrons with the inner-shell electrons of the anode material, there is either excitation or ionization of the interacting shell electron. Each atomic shell has its element-specific binding energy, with the lowest energy at the innermost shell. The excited state of the atom returns to a lower energy level by filling the free position in the inner shell with an outer-shell electron. The remaining energy is emitted in form of a photon, which is called characteristic radiation. The characteristic lines with individual energies are identified by the atomic orbitals they originated from, i.e., electrons falling from the L-shell to the K-shell emitting the K-alpha radiation. Those occur as discrete lines in the X-ray spectrum specific to the material. A full X-ray spectrum, consisting of bremsstrahlung and characteristic lines, is shown in Fig. 2.2.

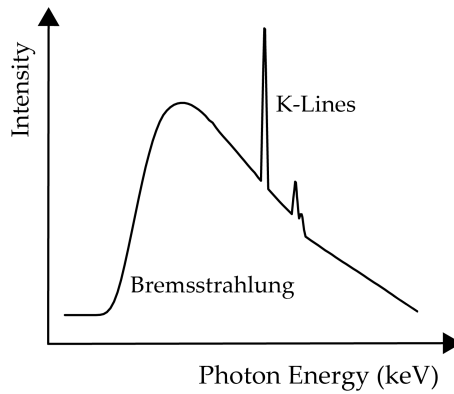


Figure 2.2: X-ray spectrum consisting of bremsstrahlung and characteristic X-rays.

### 2.2.2 Stopping power

The energy loss of the electrons, as it occurs during the generation of X-rays, can be described by the stopping power, which is the deposited energy per unit path length [12]. It is composed of a term for the interactions with the shell-electrons of the absorber material, the collision stopping power  $S_{\text{col}}$ , and one term for the production of bremsstrahlung, called radiation stopping power  $S_{\text{rad}}$ :

$$S_{\text{tot}} = \frac{dE}{dx} = S_{\text{col}} + S_{\text{rad}}. \quad (2.2)$$

To quantify the stopping power without the influence of the mass density  $\rho$  of the material, the mass stopping power is defined with:

$$\frac{S_{\text{tot}}}{\rho} = \frac{S_{\text{col}}}{\rho} + \frac{S_{\text{rad}}}{\rho}. \quad (2.3)$$

The collision stopping power can be expressed with the following formula:

$$S_{\text{col}} = \left( \frac{dE}{dx} \right)_{\text{col}} \propto \rho \cdot \frac{Z}{A} \cdot \frac{m_e}{E} \quad (2.4)$$

where  $m_e/E$  is the reciprocal mass-specific energy of the electron and  $Z/A$  the ratio between the atomic number and the mass number of the absorber material. For electrons with velocities close to the speed of light, a relativistic approach based on quantum theoretical assumptions is necessary [13].

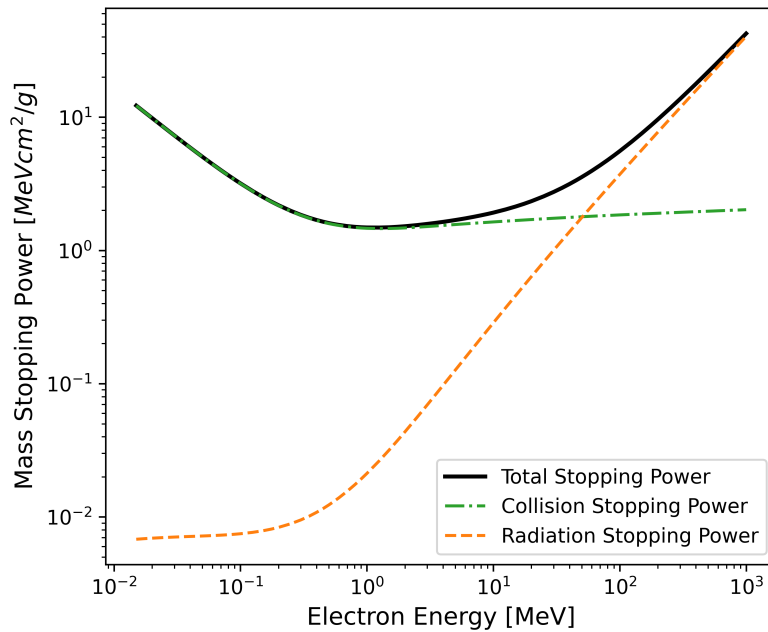


Figure 2.3: Collision and radiation stopping power of electrons as a function of the electron energy for the interaction with aluminium [14].

The radiation-stopping power is proportional to the electrons' energy  $E_{\text{kin}}$  because for high amounts of bremsstrahlung, low impact parameters need to be reached to get close to the nucleus. The proportionality to the squared atomic number,  $Z^2$ , shows the efficiency of heavier elements for the generation of bremsstrahlung. It is

described in detail with:

$$S_{\text{rad}} = \rho \cdot \frac{1}{u} \cdot r_e^2 \alpha \cdot \frac{Z^2}{A} \cdot E_{\text{kin}} (R_{\text{rad},n} + \frac{1}{Z} R_{\text{rad},e}). \quad (2.5)$$

$r_e$  is the classical electron radius,  $\alpha$  is the dimensionless fine-structure constant which quantifies the strength of the electromagnetic interaction between elementary charged particles, and  $R_{\text{rad}}$  is a rest term without any dimension in which  $n$  describes the radiation stopping power in the nucleus Coulomb field and  $e$  in the atomic electron field. The proportion of both terms of the mass stopping power as a function of the electrons' energy with a range from 1 keV to 1 GeV is shown for the example of aluminium (Al) in Fig. 2.3.

### 2.2.3 X-ray tubes

For specific utilizations, X-rays are typically generated in vacuum tubes as shown in Fig. 2.4. Electrons are generated in a heated cathode and accelerated with a

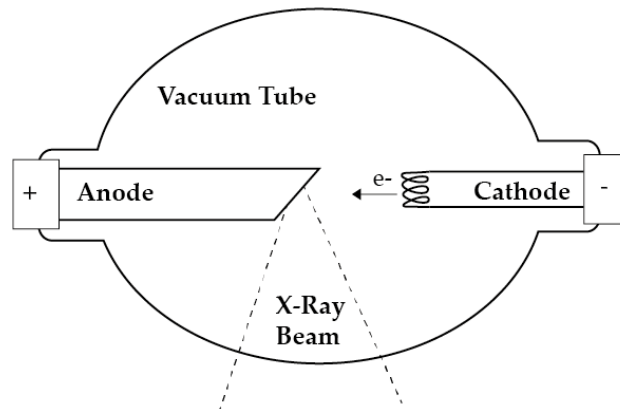


Figure 2.4: Schematic X-ray tube.

high voltage between the cathode and anode. By the abrupt deceleration in the field of the anode atoms, bremsstrahlung and characteristic X-rays are generated during the interaction processes preciously described. The anode has an angular shape that directs the X-ray beam perpendicular to an output window. Depending on the emission angle of the X-ray photons relative to the anode-cathode axis, the spectra show different energy distributions and intensities. This effect is known as Heel effect and is based on different attenuation of the photons depending on their pathways through the anode material.

Because of the low efficiency for the production of X-rays (around 99% of the energy of the electrons is transformed into heat), the anode needs a high melting point to be resistant. An ideal material for anodes is tungsten (W), which is heat resistant and offers because of the high atomic number also a good yield of bremsstrahlung. To improve the durability of the X-ray tube, which is massively affected by the heat, a water or oil cooling system or rotation of the anode is common [15].

## 2.3 Radioactivity

Although radioactive solutions, as used in nuclear medicine, are not part of the investigations in this study, a general background of radioactivity should be presented in the following to introduce all sources of ionizing radiation. For optimization of radiation protection, phantoms are also important tools in the field of nuclear medicine.

Different kinds of ionizing radiation occur during the radioactive decay of unstable atomic nuclei. An unstable state of a nucleus is reasoned in a disturbed neutron and proton equilibrium. Different decays are possible for the transition of a radionuclide  $X$  to another radionuclide  $Y$  or, in the end, a stable atom.

During the  $\alpha$ -decay (eq. 2.6) an  $\alpha$ -particle, which is identical to the nucleus of  ${}^4\text{He}$ , is ejected, while the mass number  $A$  of the radionuclide is reduced by four and the atomic number  $Z$  by two. In this process, additional energy  $\Delta E$  is emitted, resulting from the difference of the mass between the mother and the daughter nuclide.



During the  $\beta$ -decay, an electron  $e^-$  and an anti-neutrino  $\bar{\nu}_e$  ( $\beta^-$ -decay, eq. 2.7) or a positron  $e^+$  and a neutrino  $\nu_e$  ( $\beta^+$ -decay, eq. 2.8) are ejected, while the atomic number of the radionuclide is increased, respectively reduced by one.



The  $\gamma$ -decay (eq. 2.9) usually follows the  $\alpha$ - or  $\beta$ -decay when the nucleus is left in an excited state. During the transition from the excited state of the radionuclide  $X^*$

to the stable state  $X$ , a  $\gamma$ -particle is ejected, which is a photon with characteristic energy for the individual radionuclide.



Radioactive decay occurs stochastically. The half-life gives a measure for the activity of atoms, which describes the time when half of the radionuclides of a certain mass decayed. Because the energy range of  $\gamma$ -radiation overlaps with the energy range of X-rays in the electromagnetic spectrum (cf. Fig. 2.1), they cannot be distinguished from each other except by their origin.

## 2.4 Interaction of photons with matter

The initial intensity,  $I_0$ , of a beam of X-rays or  $\gamma$ -particles is attenuated if it passes through an absorber material. This behaviour is described by the material's linear attenuation coefficient  $\mu$ . For mono-energetic, thin X-ray beams, the intensity  $I(d)$  behind a homogeneous absorber material with the thickness  $d$  can be expressed with the following equation, known as Lambert-Beer's law:

$$I(d) = I_0 \cdot \exp(-\mu d). \quad (2.10)$$

For polyenergetic X-ray spectra and an inhomogeneous material, the element and energy dependence of  $\mu$  needs to be considered in the Lambert-Beer's law, which changes to

$$I(t) = \int_0^{E_{\max}} I_0(E) \cdot \exp\left(-\int_0^d \mu(E, x) dx\right) dE, \quad (2.11)$$

where  $E$  is the energy, and  $x$  is the beam direction. The quotient of  $\mu$  and the density of the material  $\rho$  is defined as the mass attenuation coefficient and gives the attenuation ability of a material independently from its density. This quantity is related to the absorption cross section  $\sigma_{\text{tot}}$  that describes the probability of an interaction between a photon and a particle in the absorber material:

$$\frac{\mu}{\rho} = \frac{\sigma_{\text{tot}}}{uA}, \quad (2.12)$$

where  $u$  is the atomic mass unit, and  $A$  is the mass number of the target material. There are four main interaction types for photon energies from  $10^{-3}$  to  $10^5$  MeV,

which can be described by their own cross sections. Those are namely the photoelectric effect  $\tau$ , the Compton scattering  $\sigma_c$ , the Rayleigh scattering  $\sigma_k$  and the pair production  $\kappa_{\text{pair}}$ :

$$\sigma_{\text{tot}} = \tau + \sigma_c + \sigma_k + \kappa_{\text{pair}}. \quad (2.13)$$

The different interaction processes can be distinguished in interactions of photons with the atomic electron shells of the absorber atoms that are dominating for diagnostic energy ranges (up to 140 keV) and interactions with the absorbers nucleus that are relevant only for energies above 1 MeV (cf. Fig. 2.5). Other effects like core photoelectric effects or triplet production with bound electrons are possible for photon energies in higher MeV ranges. Those effects will be neglected in the following. (The explanations refer to the excellent overview of radiation physics given in [16].)

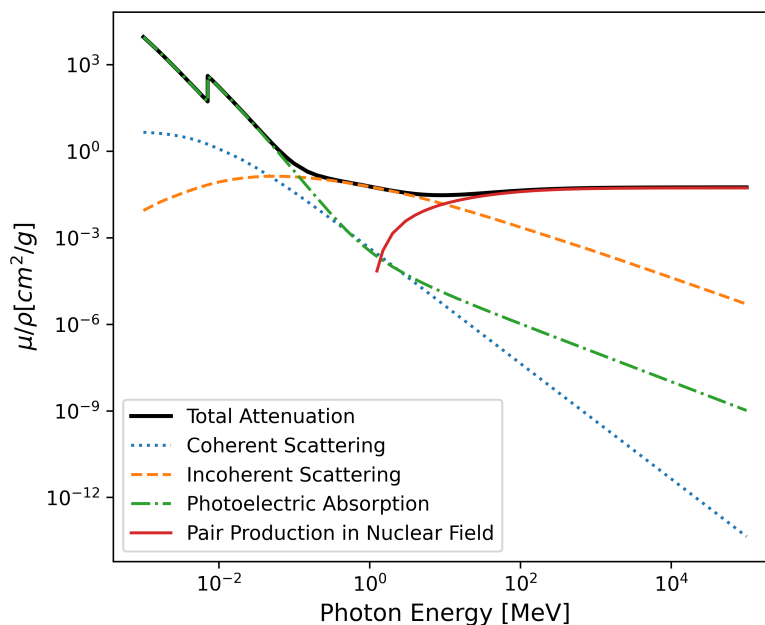


Figure 2.5: Mass attenuation coefficients and the single interaction cross sections as a function of the photon energy for aluminium [17].

### 2.4.1 Photoelectric effect

The photoelectric effect occurs for an interaction of a photon with an atomic electron of the absorber atoms. During this, the whole energy of the photon is transferred to a bound electron of one of the inner shells of the target atom. If the transferred

energy is equal to or larger than the specific binding energy of the electron, it will be released from the atomic compound. The excess energy is transferred into kinetic energy of the electron. The released electron is also called a secondary particle.

The photo attenuation coefficient  $\tau$  describes the probability for a photoelectric interaction. The probability of a photoelectric interaction increases with the absorber's mass density and electron density. With further theoretical assumptions, the latter can be expressed as proportional to the atomic number  $Z$ , with an exponent of 4 for lighter elements and 4.5 for elements with high atomic numbers for photo interactions with the K-shell [17, 18]. Additionally, there is an energy dependence of the photo interaction with  $1/E_\gamma^3$  for photons below 511 keV and with  $1/E_\gamma$  for photons significantly above 511 keV. These relationships define the relevant energy range for diagnostic imaging with X-rays. Owing to the high  $Z$ - and  $E$ -dependence, the contrast between different materials is the best for photons with energies below 100 keV. The absorption probability becomes maximum for photon energies  $E_\gamma$  equal to the binding energies of the electrons. For this reason, there are typically absorption edges for the energy dependence of the photo interaction coefficient, as shown for the example of Al in Fig. 2.5. In total, the proportionality of  $\tau$  to the relevant quantities can be summarized to:

$$\tau \propto \rho \frac{Z^n}{A \cdot E_\gamma^m}, \quad (2.14)$$

with the mass number  $A$ , and the exponents  $n=4-4.5$  and  $m=1$  or  $3$ .

## 2.4.2 Compton scattering

The Compton effect describes an inelastic scattering process of a photon and a nearly free electron of the outer atomic shell of the absorber atoms. In this process, the photon transfers energy to the electron, which is released as a secondary particle (called Compton electron) from the atomic field. In consequence, the kinetic energy of the photon (called Compton photon) is decreased, and its moving direction is changed. The remaining energy minus the electrons binding energy is translated into kinetic energy of the electron after the scattering process. The estimation of the probability for a Compton interaction, described by the Compton coefficient  $\sigma_c$ , needs a detailed analysis under consideration of relativistic quantum theory that was done by Klein and Nishina [19]. Simplified, the probability for Compton interactions is approximately independent of the material of the absorber because

it is proportional to  $Z/A$ , which is equal to  $1/2$  for most stable and light elements. Moreover, the energy dependence can be expressed with  $1/E_\gamma^n$  with  $n=0.5 - 1$ . In summary, the probability can be estimated with the following relationship:

$$\sigma_c \propto \rho \cdot \frac{Z}{A} \cdot \frac{1}{E_\gamma^n} \propto \rho \cdot \frac{1}{2} \cdot \frac{1}{E_\gamma^n}. \quad (2.15)$$

For the scattering direction of the Compton photon, angles between  $\phi = 0^\circ$  and  $\phi = 180^\circ$  are possible, which means no scattering for  $0^\circ$  and total backscattering of the photon for  $180^\circ$ . The probability of backscattering of the Compton photon decreases with higher photon energies. In general, the energy transmitted from the photon to the Compton electron increases with the scattering angle of the Compton photon. In the case of a total backscattering of the photon, the electron's energy becomes maximum and the photon's energy minimum. This context can be expressed with the following equation that describes the energy relation between the initial photon and Compton photon:

$$E'_\gamma = \frac{E_\gamma}{1 + \frac{E_\gamma}{m_0c^2}(1 - \cos\phi)}, \quad (2.16)$$

where  $E'_\gamma$  is the remaining energy of the Compton photon,  $E_\gamma$  the initial energy of the photon,  $E = m_0c^2$  is the rest mass-energy of an electron and  $\phi$  the photons scattering angle [16]. For human tissues, the Compton effect is the dominating interaction effect for the range of diagnostic and therapeutic energies between 100 keV and 30 MeV.

### 2.4.3 Rayleigh scattering

Elastic scattering processes between photons and bound electrons of the absorber atoms are called Rayleigh or incoherent scattering. In this interaction type, no energy transfer to the electron occurs, and the electron remains in the atomic compound. However, the atomic compound is stimulated to forced vibrations equal to the photon's frequency. The absorbed energy is irradiated back so that there is no energy loss for the photon but a change of direction. The probability for incoherent scattering, described by the incoherent scattering coefficient  $\sigma_k$  is anti-proportional to the quadratic photons energy  $E_\gamma$  and proportional to the density  $\rho$  and the quotient of  $Z^{2.5}/A$  of the absorber material and can be summarized to:

$$\sigma_k \propto \rho \cdot \frac{Z^{2.5}}{A \cdot E_\gamma^2} \propto \rho \cdot \frac{Z^{1.5}}{E_\gamma^2} \quad (2.17)$$

In human tissues, the Rayleigh scattering contributes to the attenuation only for photon energies below 20 keV [20].

#### 2.4.4 Pair production

For photon energies higher or equal to twice the rest mass energy of an electron (1022 keV), there is the possibility for spontaneous production of an electron-positron pair during the interaction of the photon with the Coulomb field of the atomic nucleus. The probability for this effect, described by the pair production cross section  $\kappa_{\text{pair}}$ , increases with the photon energy on a logarithmic scale.

$$\kappa_{\text{pair}} \propto \log(E_\gamma) \tag{2.18}$$

For photon energies above 10 MeV and materials with high atomic numbers, the pair production becomes the primary interaction process. Consequently, for diagnostic X-ray qualities as used in the context of this thesis, it is irrelevant.

### 2.5 Interaction of secondary electrons with matter

Unlike photons, charged particles are surrounded by an electrical field. This leads to a significantly increased probability of interaction with atoms and explains the generally lower range of particle radiation like  $\beta$ - or  $\alpha$ -radiation in matter compared to photons. Electrons are the main secondary particles that arise during the interaction of photons with matter described previously. The general physics for energy deposition during the interaction of electrons with matter are described in section 2.2.2. The relevant interaction process for secondary electrons as they occur for the application of X-rays in diagnostic and interventional imaging is the interaction with the field of atomic electrons. Therefore, the energy deposition can be described by the collision stopping power  $S_{\text{col}}$ . The total energy loss of one interaction is minimal compared to the initial electron energy. Many interactions and constant energy deposition to the surrounding material over all path lengths occur until an electron stops. The single interaction steps are deterministic.

## **2.6 Interaction of ionizing radiation with biological tissues**

Eukaryote cells, which are the smallest functional subunit of human tissues, are complicated systems built of complex organelles in a cell plasma surrounded by a lipid bilayer membrane. The cell plasma consists to a large extent of water but contains also metabolites and other relevant substances such as acids, glucose and fats. The nucleus contains the deoxyribonucleic acid (DNA), which is built of specific sequences of bases (Adenine, Guanine, Thymine and Cytosine) arranged in a helical double-strand structure. The DNA includes the genetic information and blueprints for the production of proteins and enzymes that are decisive for the cell metabolism. Because the nucleus is the only organelle available only once in the cell, possible damage is most drastic here.

For the irradiation of a cell, it has to be separated between direct and indirect effects. The direct interaction of ionizing particles with the DNA strands can lead to damages like breaks of either one or even both DNA strands. Direct effects are unavoidable. However, the probability is small because of the comparatively low target volume of the nucleus. More often, interactions are located in the cell plasma, followed by indirect effects on the DNA. Those indirect effects are subject to several previous steps. The first step includes the physical interaction processes between the ionizing particle and an atom or molecule in the cell compound. Consequently, ionized or excited atoms and molecules are left, leading to forming radicals. Those are highly reactive and are bound in the following step to the metabolites. In the last step, this can also lead to modifications of the DNA, like aberrations of chromosomes or breaks in the DNA strands. The indirect effects can be affected, for example, by the oxygen concentration in the cell [21].

The cells have sophisticated repair mechanisms to fix damages in the DNA. With this, smaller defects, e.g. by the daily impact of natural ionizing background radiation, can be fixed. Nevertheless, the repair mechanisms are not infallible, and the probability of wrong repaired or missed DNA damages increases with higher amounts of ionizing radiation, owing to higher numbers of defects.

Based on these effects, it needs to be distinguished between tissue reactions and stochastic radiation effects on biological matter [22]. Tissue reactions occur for high doses of ionizing radiation that lead to total damage of cell organelles and, following on this, to the cells' death. On a higher level, this means a necrosis of the irradiated

tissues, the development of radiation sickness or even death of the irradiated person. Those effects underlie tissue-specific thresholds for doses and increase linearly with the dose. In contrast, stochastic effects describe the random occurrence of unfixed DNA damages without direct influence on the cell. This is not subject to any threshold dose and occurs randomly for any amount of radiation. Consequently, those DNA damages may lead to malignant changes in the cell and uncontrolled growth of tumours, even years after the irradiation. Moreover, damage to gonads can also affect the descendants of the irradiated person. Therefore, the application of ionizing radiation on humans has to be as low as reasonable achievable (ALARA).

## 2.7 Computed Tomography

Computed tomography (CT) allows the generation of sectional images of human bodies by combining various X-ray projection datasets with computer algorithms. This way, internal structures are visible without overlap, as they occur in conventional X-ray projection images. The irradiation from multiple directions is typically done by rotating X-ray tube and detector systems. Modern scanners (3<sup>rd</sup>-generation) consist of an X-ray tube with a fan opening angle of 40 to 60° and a detector array with 500 - 800 single detectors on the opposite rotating around a patient table, as shown in Fig. 2.6.

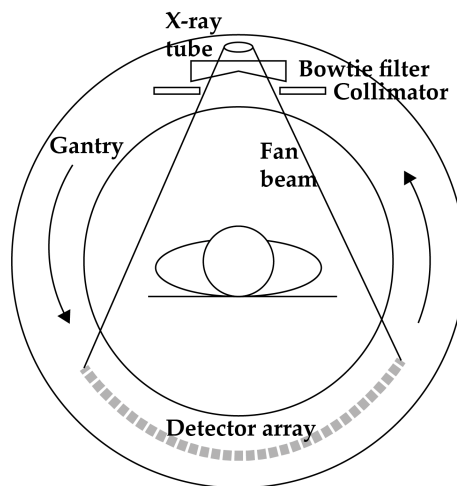


Figure 2.6: General construction of a conventional 3<sup>rd</sup>-generation CT-scanner.

While previous CT-scanners had only one detector row, modern scanners can collect the data for multiple slices with several rows of detector elements next to

each other. The collimator behind the X-ray source reduces the X-ray field to the relevant slice in the case of a single slice CT or to the range of active detector elements in the case of a multi-slice CT. With a translational movement of the patients' table, different body regions can be scanned either with a sequential or a helical mode [23].

In contrast to the sequential mode, also known as axial mode, where cross sectional images are obtained step by step with one rotation of the X-ray tube for each increment of the patients table, in the helical mode, also known as spiral mode, the patients table is moved continuous during constant rotation of the X-ray tube. This leads to helical projection data that are translated to cross sectional images in a separate step. The pitch factor  $p$  describes the ratio between the table feed per tube rotation  $d$  and the total collimation, i.e. the number of scanned slices  $N$  multiplied with the nominal slice thickness  $T$ :

$$p = \frac{d}{N \cdot T}. \quad (2.19)$$

The nominal slice thickness is the full width half maximum (FWHM) of the slice sensitivity profile, which is for sequential scan mode a rectangular function that is widened to a bell-shaped curve by the table movement in the helical mode [24, 25]. Typical tube voltages for CT-imaging are in the range of 70 to 140 kV. The spectrum is usually strongly filtered to eliminate low energy photons that do not contribute to the image contrast but lead to unnecessary dose in the patient. Additionally, a beam shaping filter is applied, often denoted because of its shape as bowtie filter, to decrease the dose to the patient's peripheries and to optimize the homogeneity of photons at the detector.

The fundamental mathematical problem in CT-imaging is the reconstruction of attenuation values for every single 3D volume element, called voxel, using the projections recorded for each gantry angle. This problem has been addressed by Johann Radon for the first time [26]. It is usually solved by filtered back projection (FBP) or by iterative reconstruction (IR) methods, as described elsewhere [27, 28].

The radiation exposure for a typical CT examination can be described with the computed tomography dose index (CTDI), which is the integrated dose in the  $z$ -direction to a rectangular profile of the nominal slice with a thickness  $T$ .

$$CTDI = \frac{1}{T} \cdot \int_{-\infty}^{+\infty} D(z) \cdot dz \quad (2.20)$$

The CTDI measured in a cylindrical polymethyl methacrylate (PMMA) phantom with one central and four peripheral holes able to accommodate a pencil ionization chamber is called  $CTDI_w$  (CTDI phantom shown in Fig. 2.9). It is a measure for the dose during a CT scan. This quantity is given by the following relation:

$$CTDI_w = \frac{1}{3}CTDI_{100,c} + \frac{2}{3}CTDI_{100,p}, \quad (2.21)$$

where  $CTDI_{100,c}$  is the CTDI over a scan length of 100 mm in the center and  $CTDI_{100,p}$  the average of the four values measured in the periphery. For helical CT scans, the  $CTDI_{vol}$  is a more suited quantity, which relates the  $CTDI_w$  to the pitch factor  $p$ .

$$CTDI_{vol} = \frac{CTDI_w}{p} \quad (2.22)$$

By a multiplication of the  $CTDI_{vol}$  with the total scan length  $L$  the dose length product (DLP) is given, which describes the total radiation exposure of the X-ray tube during the CT examination:

$$DLP = CTDI_{vol} \cdot L. \quad (2.23)$$

### 2.7.1 Hounsfield unit scale

Firstly, the mass attenuation coefficients for X-rays in matter show a general energy dependence (cf. Fig 2.5). Secondly, the energy spectrum of an X-ray tube depends on the tube voltage, the anode material and the additional filtration. Thirdly, every detector has a unique energy response. Therefore, the attenuation values recorded with a CT-scanner are integrated values over spectra, which are not necessarily equal. This makes a comparison of images of different scanner types impossible. A solution is the Hounsfield unit (HU) scale, on which linear attenuation values  $\mu$  are normalized to the attenuation values of water,  $\mu_{water}$ , and air,  $\mu_{air}$ , (in the following referred to as CT density with the unit HU):

$$CT\ density(\mu) = \frac{\mu - \mu_{water}}{\mu_{water} - \mu_{air}} \cdot 1000. \quad (2.24)$$

Each CT-scanner is calibrated to  $\mu_{air} = 0$ . With this, the CT density of air is  $-1000$  HU and  $0$  HU for water. The general HU scale is limited for human tissues to values from  $-1000$  to  $3000$  HU. The Compton effect dominates in the relevant energy range for light elements. Thus, the CT densities becomes approximately energy in-

dependent, and HU images are comparable for different CT devices. Yet, for bones with heavier elements, like calcium (Ca), this applies less.

The CT densities are represented in grey values. Owing to the humans' limited distinguishability of grey values, only a selected range of CT densities can be illustrated simultaneously. By choosing the level, i.e. a certain center and the width of the visible range, different contrasts can be visualized and adapted to the tissue of interest. [29]

## 2.8 Dosimetry

Dosimetry is a meteorological discipline focusing on quantifying energy deposition of ionizing radiation to matter. For this reason, different quantities to quantify doses were defined, which can be measured using different physical concepts described in the following.

### 2.8.1 Fundamental dosimetry quantities

Historically, a huge number of quantities was defined to describe the absorption of ionizing radiation by a medium or a body. They can be divided into physically defined quantities and protective quantities. In the following, an introduction to the most relevant quantities is given [12].

The general radiation exposure of a body is described by the fluence  $\phi$  that is the number of particles  $dN$  per cross-sectional area  $da$ , perpendicular to the initial direction of the particle

$$\phi = \frac{dN}{da}. \quad (2.25)$$

A small energy is deposited in the medium during each interaction  $i$  of an ionizing particle and an absorber atom. This is a stochastic quantity and is called energy deposit  $\epsilon_i$ :

$$\epsilon_i = \epsilon_{\text{in}} - \epsilon_{\text{out}} + Q. \quad (2.26)$$

It is given by the energy of the incident particle of the interaction,  $\epsilon_{\text{in}}$ , the total energy of all charged and uncharged ionizing particles leaving the interaction,  $\epsilon_{\text{out}}$ , and the differences in the rest energies of the nucleus and other particles participating in the interaction process,  $Q$ . The sum over all energy deposits is the energy imparted

$\epsilon$ :

$$\epsilon = \sum_i \epsilon_i, \quad (2.27)$$

which can be taken over single or multiple energy-deposition events, meaning that only one primary particle trajectory or several independent trajectories would be included. The mean energy imparted  $\bar{\epsilon}$  describes the energy released to a total volume by subtracting the mean radiation energy,  $R_{\text{in}}$ , of all charged and uncharged ionizing particles entering, with the mean energy,  $R_{\text{out}}$ , of particles leaving the volume.  $\sum Q$  is again the change of all rest energies:

$$\bar{\epsilon} = R_{\text{in}} - R_{\text{out}} + \sum Q. \quad (2.28)$$

The unit of the energy is Joule (J). The mean energy imparted  $d\bar{\epsilon}$  divided by the mass  $dm$  of the irradiated matter defines the absorbed dose  $D$ , whose unit J/kg is called Gray (Gy).

$$D = \frac{d\bar{\epsilon}}{dm} \quad (2.29)$$

To consider the energy transferred from photons or neutrons to charged secondary particles only, there is another dosimetry quantity called kinetic energy released per unit mass (Kerma) ( $K$ ). It is calculated by the mean sum of the transferred kinetic energies to the charged secondary particles,  $dE_{\text{tr}}$ , divided by the mass of the irradiated volume  $dm$ :

$$K = \frac{dE_{\text{tr}}}{dm}. \quad (2.30)$$

The time-differential quantity of the absorbed dose and the Kerma is the absorbed dose-rate, respectively Kerma-rate given in Gy/s.

Based on these physical quantities some protective quantities to directly rate the impact of ionizing radiation on human bodies were developed by the International Commission on Radiological Protection (ICRP) [30, 31].

For this, the kind of ionizing radiation and the different sensitivity of organs and tissues needs to be considered. To consider the type of radiation the radiation weighting factor  $w_R$  was defined. This was done for  $\gamma$ ,  $\beta^+$ ,  $\beta^-$  and  $\alpha$ - radiation based on two different models. The first model was based on experimental data of the relative biological effectiveness for low doses of various types of radiation [32]. The other model estimated the factors by the theoretical model of the linear energy transfer (LET), which is the linear rate of energy loss of charged particle radiation per unit length of path through an absorber material. High LET-radiation, like

alpha particles, causes major damage over a short distance compared to low-LET radiation like  $\gamma$  or electron radiation [33]. Both approaches lead to compatible weighting factors, listed in table 2.1.

The equivalent dose  $H_T$  for irradiation of an organ or tissue  $T$  is the summation of

Table 2.1: Radiation weighting factors [33].

Radiation type	$w_R$
Photons	1
Electrons	1
Protons, $E > 2$ MeV	5
Alpha particles	20

all types of involved kind of radiations,  $R$ , multiplied by the average absorbed dose in the volume of the specific organ  $D_T$

$$H_T = \sum_R w_R D_T. \quad (2.31)$$

With the tissue weighting factor  $w_T$ , the radiation sensitivity of different organs or tissues can be considered. The sum over all specified tissues and organs, i.e. for total body irradiation, is  $\sum_T w_T = 1$ , while sensitive organs or tissues like the active bone marrow have the highest fractions to the effective dose. These factors were developed based on radiobiological and epidemiological findings and are well summarized in literature [30, 33]. The currently recommended values for  $w_T$  are summarized in Table 2.2. The effective dose  $ED$  can be calculated by the sum of

Table 2.2: Tissue weighting factors [30].

Organs	$w_T$
active bone-marrow, colon, lung, stomach, breast, remaining tissues <sup>a</sup>	0.12
gonads	0.08
bladder, oesophagus, liver, thyroid	0.04
bone surface, brain, salivary glands, skin	0.01

<sup>a</sup>remaining tissues: adrenals, extrathoratic region, gall bladder, heart, kidneys, lymphatic nodes, muscle, oral mucosa, pancreas, prostate, small intestine, spleen, thymus, uterus.

the equivalent dose of all irradiated organs or tissues

$$ED = \sum_{\text{T}} w_{\text{T}} \sum_{\text{R}} w_{\text{R}} D_{\text{T,R}} = \sum_{\text{T}} w_{\text{T}} H_{\text{T}}. \quad (2.32)$$

With this quantity, the direct health effects of ionizing radiation can be estimated. In principle, the unit of the equivalent and effective dose is Gy as for the physical quantities. However, the unit for the protective quantities is called Sievert (Sv) for a better distinction.

## 2.8.2 Dosimeter

The measurement of the physical dosimetry quantities described above is possible by several methods making use of the interaction of ionizing particles with gas, solids, semiconductors or films. The dosimetry with ionization chambers and thermoluminescence dosimeters is introduced in the following sections as it is primarily employed in this thesis.

### 2.8.2.1 Ionization chambers

Ionization chambers are most common for clinical dosimetry because of the well-known physical concepts, the possibility for absolute dosimetry, and the high accuracy over a broad energy range. In gas-filled chambers, the charge carrier, produced by the interactions of ionizing radiation and gas atoms, are measured using the principle of a capacitor. For this, a voltage is applied between two electrodes to collect the positive ions and negative electrons.

Decisive for exact dosimetry is the usage of the chamber in the right voltage range. A correct dose can only be detected if all charge carriers originating from the ionizing radiation are collected by the electrodes. For too low operating voltages, free charge carriers tend to recombine and are thus not collected by the electrodes, which results in a lower signal. For very high voltages, the probability of further interactions of free charge carriers with the gas atoms increases, which will raise the signal.

There are multiple types of ionization chambers, for example, parallel, cylindrical or spherical chambers. For clinical applications, cylindrical chambers are most suitable because of their rotational symmetry. The active volume ranges from several cm<sup>3</sup> for detecting the background radiation to 0.1 cm<sup>3</sup> for, e.g. in-vivo dosimetry on patients during therapy. Most ionization chambers contain ambient air under atmospheric

pressure. However, using noble gases like Xenon under higher pressures can increase the counting efficiency. [34]

The response of each chamber type depends on factors like for example the radiation quality, the irradiation direction, or the field size when the chamber is not irradiated completely. Therefore, each ionization chamber must be calibrated with a well-defined reference radiation [35]. With this, the individual calibration factors  $N_d$  or  $N_k$  for converting the chamber signal  $M$  to either dose in water,  $D_w$ , or air Kerma,  $K_a$ , are determined. To correct for deviations from the calibration conditions, correction factors, e.g., for deviating temperature ( $k_T$ ), atmospheric pressure ( $k_p$ ), or radiation quality ( $k_Q$ ), are necessary, which are included in the corrected chamber signal  $M_{\text{corr}}$  [36].

$$\begin{aligned} D_w &= M_{\text{corr}} \cdot N_d, \\ K_a &= M_{\text{corr}} \cdot N_k. \end{aligned} \tag{2.33}$$

Depending on the aim of application, e.g. measuring doses inside a medium or air, other concepts and correction factors need to be considered to ensure accurate dosimetry by ionization chambers. The theoretical concepts are described with the concept of charged particle equilibrium or in the Bragg-Gray cavity theory, which is beyond the scope of this work and summarized elsewhere [37, 38].

### 2.8.2.2 Thermoluminescence dosimetry

Thermoluminescence dosimeter (TLD) save the deposited energy of ionizing radiation and emits it in form of visible light after a heating process. A typical material for TLDs is lithium fluoride (LiF) dotted with magnesium or titanium [39]. The phenomenon of thermoluminescence can be described with the well-established band theory that will be outlined in a simplified form in the following.

An electronic band structure is formed in a crystal lattice through overlapping orbitals of single atoms. Instead of strict energy levels like in the atomic model, those bands are broader but divided by forbidden zones called band gaps. The electrons included in the bands are no longer assigned to the individual atoms but to the crystal association. The last band fully filled with electrons is called the valence band. The band above is the conduction band. With the absorption of energy equal or higher than the gap energy, e.g. by interaction with ionizing radiation, electrons of the valence band can pass into the conduction band, leaving an electron hole in

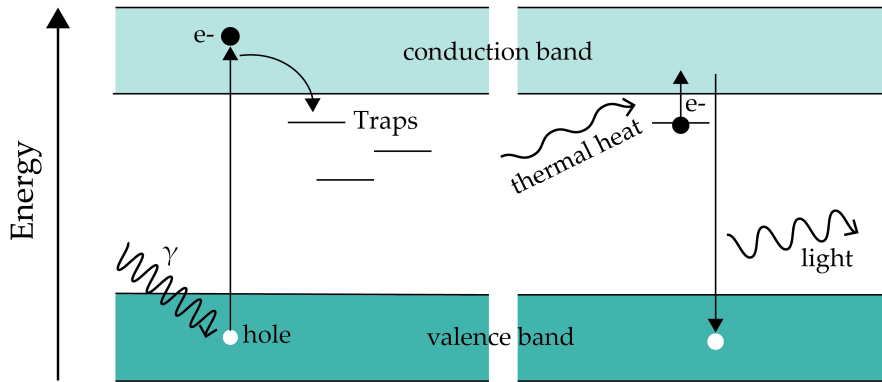


Figure 2.7: Schematic depiction of the thermoluminescence process. The first step shows the stimulation of the electron into the conduction band with ionizing radiation. The second step shows the heat-induced transition of the electron, caught by the trap, back into the valence band under the emission of visible light.

the valence band. If the crystal lattice is disturbed by defects or foreign atoms, additional energy levels in the band gap arise. Those extra levels, called traps, can catch free electrons of the conduction band. The electrons are collected by those traps instead of directly returning into the valence band. These energy states are semi-stable, meaning electrons can only leave the traps and combine with holes in the valence band after absorption of additional energy. In thermoluminescence the additional energy is provided by heat. Different temperatures are necessary to release the electrons from the traps depending on the energy level. With the transmission of an electron from the conduction to the valence band, visible light is emitted (cf. Fig. 2.7).

This signal is collected in a TLD-reader with a photomultiplier, where charge carriers are generated by the light. The temperature-dependent signal is saved as a heat curve. The total number of generated charge carriers is proportional to the intensity of the light and also proportional to the exposure dose.

Thermoluminescence dosimetry is only a relative method because every TL-crystal acts differently to the same amount of radiation because of differences in defects or energy levels. This makes an additional calibration step for every crystal and radiation quality necessary, for which a reference dose is measured using an absolute dosimeter.

## 2.9 Monte-Carlo methods

Even if a first Monte-Carlo (MC) approach was used in 1777 for the analogue determination of  $\pi$  [40], the development of computers was essential for the use of MC simulations in advanced applications. In 1945, when the first electronic computer was available, the development of a thermonuclear computational method based on random processes in connection with the secret project of the atomic bomb at the Los Alamos laboratories started. Based on Enrico Fermi's primary developments, which were already done in the 1930s, the MC method was further developed and established by Stanislaw Ulan, John von Neumann and Nicholas Metropolis for neutron transport problems in the years after the war [41]. They named it after Monaco's famous casino district, Monte-Carlo, owing to the statistical approach it is based on. In principle, by using MC methods, any case of numerical problem can be solved based on random number sampling. Especially for the simulation of particle trajectories MC simulations are well suited. This way, events can be evoked by a set of probability distributions, where the parameter of the interacting particles, like the position or velocity of the next step, are generated.[42].

For the simulation of uncharged ionizing particles in a geometric set-up, this means sampling the typical interaction processes for, e.g. photons, like photoelectric absorption, Rayleigh and Compton scattering or pair building under consideration of the mean free path length of the particles and the differential cross sections for the interaction processes.

Charged particles have much lower mean free path lengths and undergo with this much more interaction processes, which increases the computational effort. Therefore, hard and soft collisions of these particles are considered separately. For soft collisions, charged particles transfer energy continuously to the surrounding matter. In contrast, hard collisions are simulated under consideration of the stopping powers, just like in the case of uncharged particles.

The corresponding cross sections are included from established databases (e.g., provided by the National Institute of Standards and Technology (NIST) [14, 17]) into the MC codes for all of these processes. Owing to the material dependency of cross sections, the surrounding geometry in MC simulations should be described with its elemental composition as accurate as possible [43].

Because MC methods follow the Gaussian distribution, the more events are sampled, the closer the result approximates to the mean. The standard deviation  $\sigma$  of

the mean increases with the number of simulated events  $N$  [44]:

$$\sigma \propto \frac{1}{\sqrt{N}}. \quad (2.34)$$

MC simulations are nowadays often used for the prediction of dose distribution in patients [45] because they offer much higher accuracy in comparison to other analytical methods [46].

## 2.10 Phantoms

For the medical application of ionizing radiation on humans, the ALARA principle has to be followed. Consequently, the functionalities of imaging and therapy systems have to be verified, and a frequent quality assurance is required. Furthermore, there is a constant aim to improve systems and methods in general, leading to better image qualities, dose reduction, or higher efficacy of therapies.

For these tasks, different phantoms are necessary to imitate the human body and to enable realistic imaging contrast and dose measurements. Phantoms must replicate realistically the interaction of ionizing radiation with bodies by imitating the beam-scattering, widening and hardening effects. Different concepts for phantoms are described in the following.

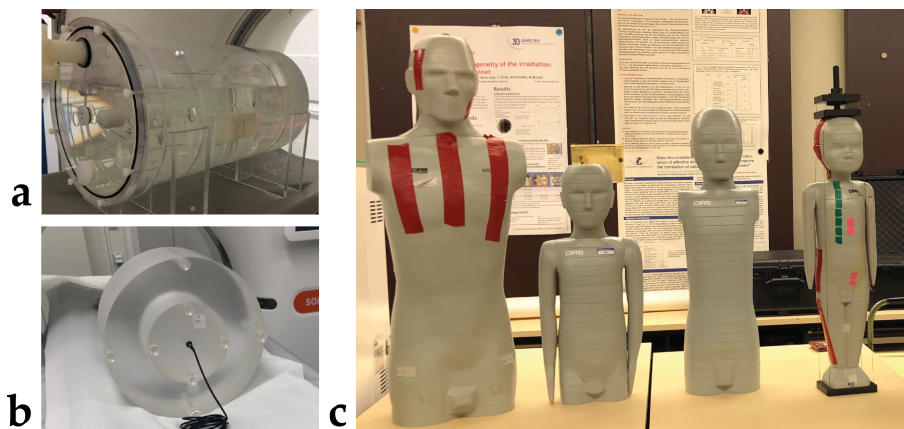


Figure 2.8: a) Phantom filled with water, b) CTDI phantom, c) antropomorphic phantom family

### **2.10.1 Standardized phantoms**

In clinics, standardized phantoms are used to perform quality assurance tests under strict requirements. Such phantoms are broadly available because quality assurance tests must be performed in every clinical unit. However, they represent the human body at least only approximately, for example, with water or PMMA as tissue equivalent material either in cubic or cylindrical shapes. Examples are presented in Fig. 2.9 a and b, where a simplified water phantom is shown beside a CTDI phantom. In radiation therapy units, a 3D-water tank phantom is typically used for the flexible measurement of dose distributions. The CTDI phantom fulfils the recommendations for the well-defined protocol to measure the dose during a CT-scan, as described in section 2.7. To assess the image quality regarding noise, the contrast sensitivity or the spatial resolution of imaging devices, other phantoms are available that include inserts with different contrast spots or sets of lines [47, 48].

### **2.10.2 Anthropomorphic phantoms**

Especially to investigate patient imaging modalities and internal dose distributions thoroughly, more realistic phantoms are required. Anthropomorphic phantoms are characterized by their realistic body shape and are made of tissue-equivalent materials, representing different organs. Full human body-phantom contain at least different materials for skeleton, lungs and average soft tissues. Because imaging or treatment parameter and the absorbed doses depend on size, weight, age, and gender, there is a need for female, male and children phantoms in various sizes. Different commercially available anthropomorphic phantoms are shown in Fig. 2.9 c. By inserting TLDs, the dose corresponding to target and risk organs can be directly measured.

Different manufacturers are providing anthropomorphic phantoms. The Rando phantoms (Alderson; RSD phantoms, Carson, California, USA) and the CIRS atom family (CIRS atom; CIRS inc., Norfolk, Virginia, USA) are common examples of anthropomorphic phantoms. While Rando phantoms exist only for an adult male and female version [49], CIRS offers a newborn, a 1-year, a 5-year and a 10-year-old paediatric phantom as well [50]. Both phantom types are designed in 2.5 to 3 cm thick slices that allow easy handling for inserting TLD or other dosimeters. While Alderson used a real human skeleton for their Rando phantom in the past, they now use synthetic tissue-equivalent and polymer mouldings and foams for bones, muscle

and lung tissues. CIRS uses epoxy-resin-based tissue equivalents. Both manufacturers ensure the tissue equivalence over a wide range of energy levels in their phantoms, following the recommendations of the International Commission on Radiation Units and Measurements (ICRU) [51].

### 2.10.3 Computational phantoms

With upcoming computing technologies, more often MC simulations were done in alternative to measurements to estimate patient doses. Apart from saving time and effort for preparations, experiments and evaluations, the simulation of any imaginable setup, every radiation source, internal and external exposition can be realized in this way.

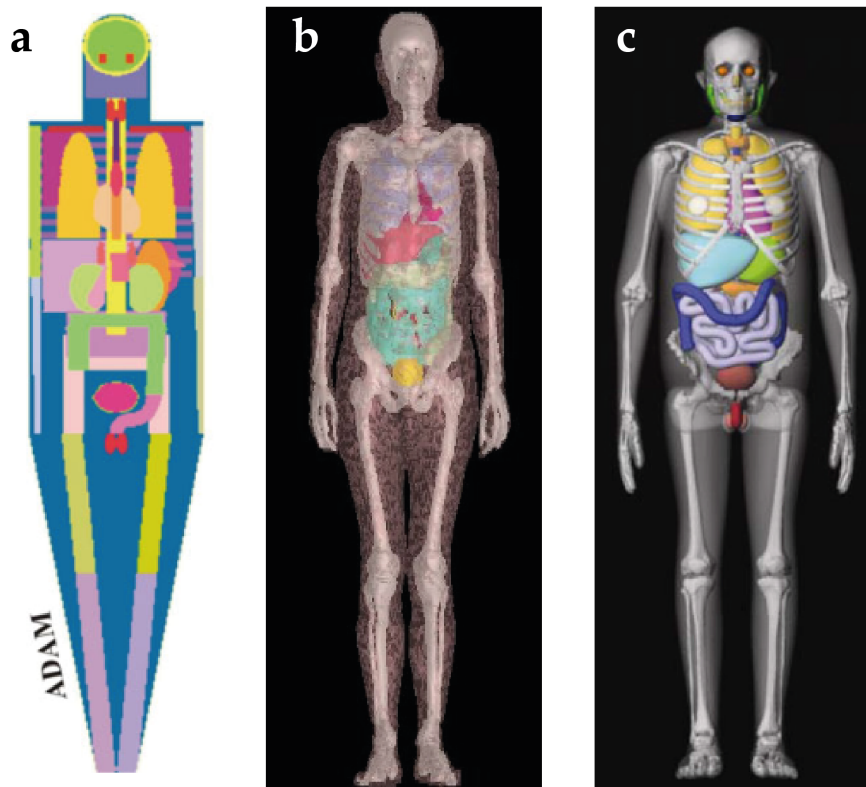


Figure 2.9: a) stylized MIRAD-5 Adam phantom [52] b) Gesellschaft für Strahlenforschung (GSF)-voxel phantom, Godwin [53] c) University Florida hybrid male phantom [54]

To simulate the interaction of human bodies with ionizing particles, computational phantoms are needed that represent the shape as well as different organs of a

human realistically. For this task, the tissues must be simulated with equal densities and elemental compositions.

The history of computational phantoms started in the 1960s and went a constant development until today [55, 56]. The first computational phantoms were stylized phantoms, where the body is composed of different geometrical shapes. Those phantoms were developed at Oak Ridge National Laboratory and are known as MIRD-5 phantoms (cf. Fig 2.9 a) [57]. In further editions, the number of organs considered grew to a detailed body phantom. With those phantoms, dose calculations for all fields of radiation physics were possible even with less powerful computers. Their era was from the 1960s to the 90s, but they are still used today, for example, in simplified CT dose reporting systems.

With the increase in computing power and availability of tomographic images of the human body, the development of more realistic phantoms became possible in the 1980s when the first voxel phantoms were designed (cf. Fig. 2.9 b). They are based on CT- or magnetic resonance (MR)-imaging data, from which the organs could be segmented in form of voxels. Each voxel is filled with a particular tissue, which is defined by the elemental composition and density. A first family of voxel phantoms was developed at the Gesellschaft für Strahlenforschung (GSF) [58]. Many other phantoms followed, such as the ICRP reference computational phantoms [59]. The most detailed voxel phantoms, e.g. the VIP-Man, consist of more than 3.7 billion voxels and more than 1400 organs and tissues [60]. However, those phantoms are limited to change their dimensions and size. More realistic modification would be associated with a lot of effort by segmenting a new voxel phantom from other tomographic images. Additionally, if it comes to the 4th dimension, when considering motion, voxel phantoms reach their limits.

In the 2000s, first mesh phantoms were developed using non-uniform rational B-spline (NURBS) modelling technologies or polygon surfaces. The closed surfaces with control points offer the ability to deform the objects. With this, cardiac and respiratory motions, based on tomographic data, can be modelled. Another advantage is that holes or gaps in wall organs that may be present in voxel phantoms because of the given voxel size can be closed in mesh phantoms. A hybrid phantom family, consisting of a voxel and a polygon mesh version, was developed by the University of Florida (cf. Fig. 2.9 c) [54].

## 2.11 3D-printing methods

3D-printing methods are, in their basic principle, a layer-wise construction of 3D objects with selective material deposition. The decisive advantage of the so called additive manufacturing (AM) methods compared to conventional manufacturing methods, such as milling or moulding, is the fast, easy and cheap production process, as it is required particularly in the model or prototype development. The following section gives an overview of the most common 3D-printing technologies and describes the general workflow [61].

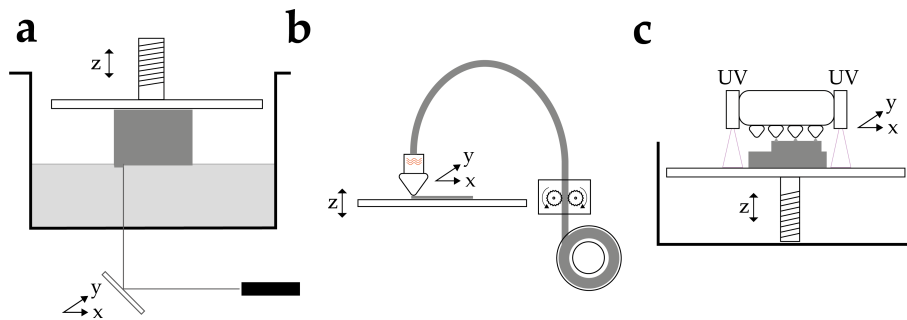


Figure 2.10: a) Stereolithography b) Fused Deposition Modelling c) Inkjet 3D-printing

### 2.11.1 General workflow

Three-dimensional objects can be constructed digitally by using computer aided design (CAD) software. Those offer different geometric modelling concepts, either with edge, surface or volume modelling (cf. Fig. 2.11 a). With a combination of those concepts, even complex models can be designed.

For 3D-printing, models need to be converted in the first step into surface models. This is possible with the standard tessellation language (stl) interface, in which surfaces are described by a tessellation with triangles (cf. Fig. 2.11 b). If each corner point of each triangle belongs to three other triangles, the unity of the surface is secured. On the other side, by a definition of a unit normal, relative to the arrangement of the corners, surfaces can be defined as inner or outer surfaces [62]. This concept unites crucial fundamentals for 3D-printing processes because objects with open or overlapped surfaces are not printable.

For the 3D-printing process itself, the input data need to be converted into a numerical control language that translates the information of the 3D objects into instructions for the 3D-printer (cf. Fig. 2.11 c). Owing to the layer-wise workflow of the printer, this process is called slicing and the file format is known as gcode. It includes information for the print head's movement, the object's slice thickness or other printing settings. It is typical for all 3D-printing methods that for complicated objects, e.g. overhangs, a support structure has to be printed and removed from the finished object.

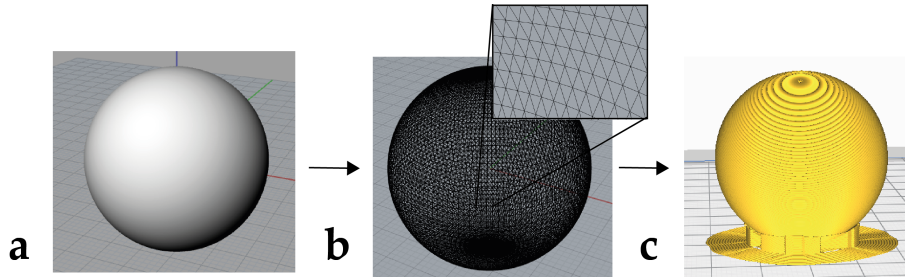


Figure 2.11: a) First step: geometric model of a sphere in a CAD program b) Second step: tessellation of the spheric surface with triangles and export as stl file c) Third step: slicing process, with the addition of necessary support structure and generation of the instructions for the 3D-printer as gcode

### 2.11.2 Stereolithography

Stereolithography (SLA) (as shown in Fig. 2.10 a.) is based on the targeted polymerization of a photosensitive resin by selective irradiation with an ultraviolet (UV) laser. For this process, the laser is directed by an adjustable mirror system along the contour of the 3D object on a platform in a resin vat. The resin solidifies at the exposed areas during the deposition with UV-light. For each layer of the object, the platform moves in the z-direction out of the resin vat. The finished object can be removed from the platform. However, some post-processing and the removal of excess resin is necessary [63].

An advantage of SLA is the high printing resolution, with 50 to 100  $\mu\text{m}$  in each direction for standard systems [64], or 5-10  $\mu\text{m}$  for special micro SLA printer [65]. The used materials are typically resins, which are mixtures of monomers, usually acrylate or methacrylate-based, a diluent to achieve the best viscosity for the processing, a chain-transfer agent to control the formation of polymer networks with properties conducting to a high quality in the printing result and a photoinitiator

that initiates the polymerization process [66]. With the addition of ceramic powders to the resin and a sintering process after printing, the production of ceramic objects is also possible using SLA [67]. In general, only one material can be processed in time, and the build volume is relatively small. These are limiting factors for the production of complex phantoms.

### 2.11.3 Fused deposition modelling

During the fused deposition modelling (FDM) method, a thermoplastic material, provided in form of a plastic wire, called filament, is melted into a thermoelastic state and deposited in strands by the movement of the print head in the x- and y-direction on a build plate corresponding to the instructions of the gcode, as shown in Fig. 2.10 b. For each layer of the object, the print bed is moved in the z-direction. The printing resolution is with 50 to 200  $\mu\text{m}$  relatively large, and a rough surface is typical for FDM printed objects [68]. In principle, the processing of every kind of thermoplastic material is possible, and many different manufacturers provide filaments for low costs. Additionally, there are a lot of different composite materials, which contain a large amount of powders of stone or metals, or wooden or carbon fibers. FDM printers are available at different price ranges from 100 € for desktop models to up to several 10.000 € for industrial machines. The latter also provides the possibility to produce two or more different kinds of materials in one step, which is advantageous for producing detailed anthropomorphic phantoms.

The FDM method was used in the further context of this thesis because the advantages exceed those of the other methods for phantoms suited for diagnostic X-ray applications.

### 2.11.4 Polyjet 3D-printing

Polyjet 3D-printing is an additive manufacturing method based on the principle of inkjet technology. Polyjet printers come with several inkjet heads that deposit tiny drops of a photopolymer material. The irradiation with UV light from a lamp directly included in the print head immediately solidifies the droplets. With the movement of the print layer in z-direction, it is possible to build a 3D object layer by layer (cf. Fig. 2.10 c).

The printing resolution typically ranges from 5  $\mu\text{m}$  to 200  $\mu\text{m}$  [69]. In addition, it is the fastest AM method presented in this context. However, polyjet printing is

also the most cost-intensive method, with machine prices of over 10.000 €. Polyjet printers offer the possibility for the multi-material processing of up to seven different materials with different colors or properties to realize detailed anatomical models or functional prototypes with, e.g., flexible parts included. Materials need to be purchased directly from the manufacturer for relatively high costs because there is no market for secondary products.

---

## 3 Tissue equivalence of 3D-printing materials

A fundamental part of this thesis is the characterization of 3D-printing materials to find suitable equivalents for all relevant tissues that can be used for the production of phantoms. For this reason, a larger number of different commercially available filaments was investigated for the attenuation as well as absorption properties in measurements, and compared to the properties of different human tissues, determined with MC simulations. In addition, alternative materials for the imitation of cortical bones and the influence of different printing settings on the absorption properties of printed samples were investigated. Parts of this chapter were published elsewhere [70, 71].

### 3.1 State of the art

The aspect of the tissue equivalence of 3D-printing materials was already investigated in previous studies with a focus on different materials, radiation qualities and kinds of tissues. Most previous studies focused on analysing materials for the FDM technology.

Different concepts were used to investigate the tissue equivalence in terms of attenuation behaviour. A popular approach was the analysis of the CT densities, measured in HU. For typical 3D-printable thermoplastic materials, as used for the FDM technology, the CT densities range between -80 HU and 340 HU [72], which is close to typical CT densities of soft tissues. Also, lower CT densities can be realised by reducing the infill density of the printed objects. The infill density gives the amount of material printed in the inner of 3D objects, for which different structures are provided in the slicing software. This way, it is possible to realise CT values of -800 HU in printed samples, which is equivalent to lung tissue [73]. Another study found infill densities between 30 and 50 % the best for the imitation of lung tissue

[74]. However, an increase in the standard deviation of the CT densities was recognised for this method.

In principle, there is a linear correlation between the infill density and the CT density as found in several studies [74–76]. With this relationship, it is also possible to imitate several CT densities with one single material only by adjusting the infill density to the required CT contrasts [73, 77]. Composite materials, including metal or stone powders, have much higher CT densities with values of up to 7200 HU [78]. Nevertheless, these values are even too high for imitating cortical bones with CT densities up to 2000 HU [79].

Another approach for investigating the attenuation behaviour is the measurement of the attenuation coefficients themselves. It was found that polylactide (PLA) and chlorinated polyethylene (PE) are similar to muscle tissue in their attenuation behaviour. In contrast, acrylonitrile butadiene styrene (ABS), Nylon and polyvinyl alcohol (PVA) are similar to adipose tissue for X-ray energies typically used for diagnostic imaging [80–82]. Furthermore, a wooden composite filament was found to be soft tissue equivalent, as well as thermoplastic Polyurethane (TPU) concerning their mass attenuation coefficients [83]. With a focus on equivalents for breast tissues beside typical FDM materials, resins typically used for SLA were investigated as well, showing that resin materials have good agreement to the glandular tissue [82]. An equivalent printing material that imitates cortical bone correctly in its attenuation behaviour was not found in any study. Instead, different concepts for the correct imitation of cortical bones were developed, for example, the production of new composite filaments, using ABS and Bismuth powder [84] or  $\text{CaTiO}_3$  [85], or the mixture of PLA and metal filaments directly in the printing process using a dual material printer [86].

In summary, a range of studies investigated tissue equivalence in terms of the attenuation behaviours of different materials using individual concepts and radiation qualities. This makes a general comparison of the results difficult. In addition, it was indicated that there are also some differences in the attenuation behaviour depending on the materials manufacturer, the 3D-printer itself, or the printing settings [80, 87]. Therefore more intensive investigations are recommended. Also, the filaments market is still growing, and there are materials yet to be characterised for their tissue equivalence. Especially with the focus on finding tissue equivalents for cortical bone, the broad range of different composite materials should be investigated in more detail.

While the attenuation behaviour was already investigated by using different concepts and radiation qualities, only minor focus was on the absorption of X-rays in 3D-printing materials until now. For therapeutic radiation qualities, the water equivalence of PLA in terms of dose absorption was shown [88]. In contrast, there are no studies investigating the tissue equivalence regarding the absorption properties of 3D-printing materials for X-ray qualities typically used for diagnostic imaging. Because realistic absorption properties are essential for phantoms aimed in determining dose distribution, it is crucial to be investigated for 3D-printing materials before starting the production of phantoms.

For this reason, this chapter of the thesis provides a detailed analysis of the tissue equivalence of a broad range of different commercially available 3D-printing materials for both relevant properties, the attenuation and absorption behaviour of X-rays. This way, a guideline for possible materials that can be used in 3D-printed phantoms suited for both clinical purposes (the assessments of image qualities and the measurement of dose distributions) is provided. In addition, the influence of different printing settings on these properties was investigated.

## **3.2 Materials and methods**

### **3.2.1 Choice of materials and sample preparations**

In total, 20 different commercially available filaments were chosen to be investigated for their tissue equivalence. They are summarized in Tab. 3.1 together with the recommended processing temperature ranges and the mass density measured for the fully printed samples (100 % infill density). Besides classical thermoplastic materials, different composite materials containing wood, carbon fibres, metal, or stone powders were considered. For two materials, either a conventionally produced material (in case of PMMA) or different manufacturers and colors (in case of PLA) were additionally considered for the attenuation analysis.

For each material, samples of in total six plates with dimensions of  $30 \times 40 \times 3.5 \text{ mm}^3$  were printed with 100 % infill density, as shown in Fig. 3.1 a. Because of the expected higher attenuation behaviour of metal-composite filament samples, the thickness of these sample plates was decreased to 2 mm. All sample plates were printed on a conventional desktop FDM 3D-printer (Ultimaker 2+; Ultimaker B.V.; Geldermansen, Netherlands) with a 0.6 mm nozzle and the slicing was performed in Cura 4.3.0 (Ul-

timaker B.V.; Geldermansen, Netherlands). The ideal processing settings, e.g. the

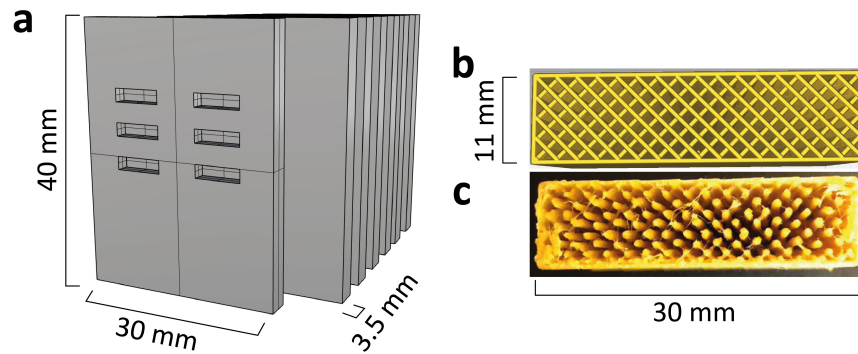


Figure 3.1: a) Sample design for the investigation of attenuation and absorption properties of 3D-printing materials printed with 100 % infill density consisting of 7 plates, one with cavities for the accommodation of TLDs. b) The line infill structure for the investigation of lung tissue equivalence as represented in the slicing software (in example of the sample printed with 35 % infill density). c) The actual printing structure in the finished sample with 35 % infill density.

printing temperature and the optimal build plate adhesion (e.g., if a heated build plate or additional adhesion layer was necessary) were tested during a temperature tower test print based on the manufacturers' instructions [89]. The printing speed varied between 15 mm/s (Moldlay) and 40 mm/s (e.g., PLA and PMMA). The layer height for each sample was 0.1 mm. The individual printing settings are summarized in the Appendix in Tab. 7.1.

For PLA, samples with different infill densities (25 to 45 %, in 5 % steps) were produced to investigate possible settings for lung tissue equivalents. The samples were printed with a line structure (cf. in Fig 3.1 b) that offers in contrast to other infill styles a comparatively homogeneous material distribution. An image of the actual printed structure inside the sample is shown in Fig. 3.1 c, for which some inaccuracy occurred. In total, three plates with two different thicknesses (two with 11 mm and one with 22 mm) were printed for each infill density. This way, the influence of the boundaries (which are inevitably printed with 100 % density to ensure the general stability of the printed objects) was minimized because no combination of different sample plates was necessary to obtain different sample thicknesses in the following experiments. All samples with reduced infill density were printed in two different orientations on the print bed, one printed with the air ducts of the infill structure parallel and one with the air ducts orthogonal to the beam direction.

Table 3.1: Conventional FDM materials investigated for their tissue equivalence given with their typical processing temperatures as well as the mass density of the printed samples with 100 % infill density.

<b>Sample name</b>	<b>Material/Mixture</b>	<b>Manufacturer</b>	<b>Processing temperature °C</b>	<b>Mass density g/cm<sup>3</sup></b>
ABS	Acrylonitrile butadine styrene	Avistron	220-250	$1.01 \pm 0.02$
Carbonfil	Polyethylenetherepthalat + 20 % carbonfibers	FormFutura	230-265	$1.16 \pm 0.02$
Copperfil	PLA + copper powder	ColorFabb	195-220	$3.34 \pm 0.02$
Easywood	PLA + 40 % wood particles	FormFutura	200-240	$1.16 \pm 0.02$
HIPS	High impact polystyrene	3ntr	220-260	$0.95 \pm 0.02$
Laybrick	Co-polymers + chalk	Polymaker	165-210	$1.19 \pm 0.02$
Moldlay	unknown	Layfilaments	170-180	$1.1 \pm 0.02$
Nylon	Nylon	Taulman 3D	225-235	$1.05 \pm 0.02$
PC Max	Polycarbonate	Polymaker	250-270	$1.16 \pm 0.02$
PETG	Polyethyleneterephthalat + glycole	Filamentworld	195-225	$1.23 \pm 0.02$
PLA	Polylactide	Filamentworld, Avistron	190-220	$1.21 \pm 0.02$
PMMA	Polymethylmethacrylate	Material4Print	230-250	$1.12 \pm 0.02$
PMMA	Polymethylmethacrylate	NKV Kunststoffe	conventionally produced	$1.18 \pm 0.02$
Polyflex	Thermoplastic polyurethane	Polymaker	220-235	$1.17 \pm 0.02$
Pure	PLA + 60 % ecological fibers	Aprinta Pro	190-220	$1.21 \pm 0.02$
PVA	Polyvinyl alcohol	FormFutura	200-240	$1.17 \pm 0.02$
Concrete	PLA + 50 % concrete powder	FormFutura	200-240	$1.57 \pm 0.03$
Potteryclay	PLA + 50 % clay powder	FormFutura	200-240	$1.51 \pm 0.03$
Granite	PLA + 50 % granite powder	FormFutura	200-240	$1.54 \pm 0.03$
Stainless Steel	PLA + steel powder	ProtoPasta	195-220	$2.22 \pm 0.06$
Terracotta	PLA + 50 % terracotta powder	FormFutura	200-240	$1.53 \pm 0.03$

For each material and infill density, an additional plate was printed, which includes several rectangular inserts with dimensions of  $2 \times 2 \times 7 \text{ mm}^3$  as shown in Fig. 3.1 a. Those are intended for the insertion of TLDs. The chosen sample design allows the investigation of the attenuation and absorption properties of the printing materials in two different experimental set-ups with different combinations of printed plates. As an example of a non-printed material, the same samples as shown in Fig. 3.1 a were cut from a conventionally produced PMMA plate. However, the thickness was 4.7 mm instead of 3.5 mm.

#### 3.2.1.1 Hydroxyapatite-resin mixtures

Because of the lack of commercially available 3D-printable equivalents for cortical bones detected during the literature research, an alternative<sup>3</sup> approach for imitating cortical bones besides the field of 3D-printing methods was additionally investigated in this thesis.

A main component of bones and teeth is hydroxyapatite, which can be reproduced synthetically in form of a powder [90]. This powder is suitable for mixing with epoxy resins that are widespread materials for the conventional production of phantoms [91]. For this reason, different mixtures of hydroxyapatite powders and epoxy resins were also taken into account to investigate their bone equivalence in terms of their attenuation behaviour.

Corresponding to the best accordance in the elemental composition to adult cortical bone [92], or newborn cortical bone [93], as shown in Fig. 3.2, mixtures with fractions of 30 %, 40 % and 50 % hydroxyapatite were produced. Those samples are referred to in the following as Apatit30, Apatit40, and Apatit50, respectively.

In the first step, the epoxy resin (SKresin 3221; HOCK, Regen, Germany) was mixed with a mass fraction of 30 % of the hardener (Epohard 3200) for five minutes. In the next step, the hydroxyapatite powder (Acros organics; Waltham, Massachusetts, USA) was added with the respective mass fractions to obtain the three different mixtures characterized in Fig. 3.2. Each mixture was stirred for several minutes to obtain the most homogeneous samples possible. In the last step, the mixtures were filled rapidly into silicone moulds of the same size as the printed sample plates. All samples were cured for one week. After removing the sample plates from the moulds, the surfaces were milled to obtain a more even structure. The mass density of the finished samples was  $1.25 \pm 0.02$ ,  $1.4 \pm 0.02$ , and  $1.53 \pm 0.02 \text{ g/cm}^3$  for Apatit30, Apatit40, and Apatit50 respectively.

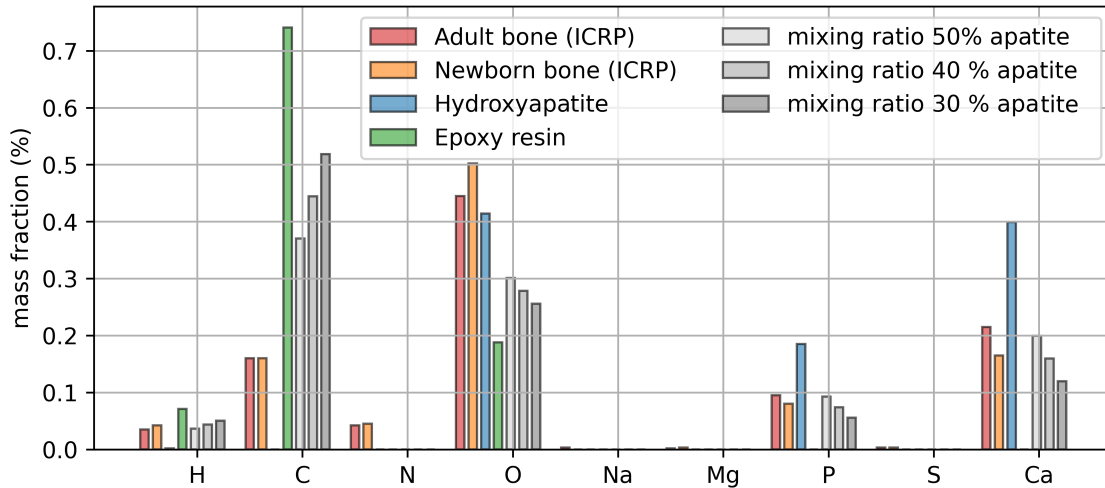


Figure 3.2: Elemental mass fractions of cortical bone compositions and different hydroxyapatite and epoxy resin mixtures.

### 3.2.2 Investigation of attenuation properties

For each material, attenuation curves were ascertained by measuring the transmission of X-rays through different combinations of the (printed) sample plates (to achieve samples with different total thicknesses  $d$ ). The measurements were performed with an industrial X-ray tube (ISOVOLT 400/10; Seifert, Ahrensburg, Germany) with a W anode and internal filtration of 7 mm beryllium (Be). A narrow beam was realized with a circular collimator with an opening of 2.4 mm that was mounted in front of the X-ray tube. It was built of a 2.0 mm lead (Pb) layer as well as a 1.8 mm copper (Cu) layer and a 1.2 mm Al layer to eliminate possible characteristic radiation of the Pb layer. Additionally, an Al filter of 2.5 mm thickness was used to filter low-energetic photons from the investigated spectra. The investigated radiation qualities are characterized by tube voltages of 70, 80, 100, 120 and 140 kV, and first Al half value layers of 0.25, 0.28, 0.35, 0.43, 0.51 cm, respectively. Those are close to typical reference radiation qualities [94] and cover the whole energy range typically used for diagnostic imaging.

The 3D-printed sample plates were located in front of the X-ray tube. An ionization chamber (M2333; PTW, Freiburg, Germany) connected to a dosimeter (UNIDOS E; PTW-Freiburg, Freiburg, Germany) was placed at a distance of 51 cm in the centre of the narrow beam. The chamber was placed on a tripod in 128 cm height above the floor, which was shielded by a Pb plate to minimize the influence of scattered radiation. The general experimental setup is shown in Fig. 3.3.

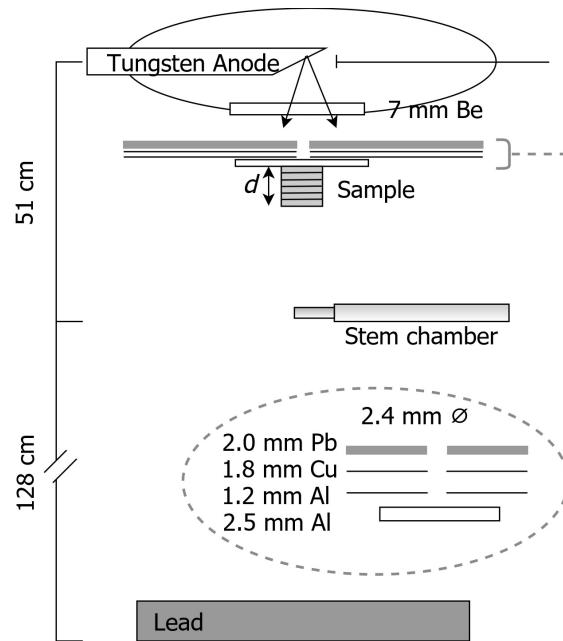


Figure 3.3: Narrow beam setup for the measurement of X-ray transmission through printed sample materials of the thickness  $d$ .

The air kerma rate  $K_a(d)$  for each combination of sample plates was measured for a tube current of 10 mA and 3 minutes. Each measurement was repeated three times, while the mean value was used for further analysis and the standard deviation for uncertainty analysis. Before starting the measurement session, the ionization chamber was subjected to temperature, pressure and background correction. All dose values were corrected by the radiation quality correction factor  $k_q$  of the used ionization chamber (determined at an official calibration institute) approximated to the investigated radiation qualities by the tube voltage.

### 3.2.2.1 Determination of apparent kerma attenuation coefficients

Following the Lambert-Beer law, attenuation curves for monoenergetic radiation can be described with a mono-exponential function (Eq. 2.10). In contrast, the radiation qualities used in the described experiments were broad X-ray spectra. Owing to this, the measured curves can only be described approximately with mono-exponential functions. The Lambert-Beer law also defines the attenuation of the photon fluence  $\phi$ , while the air Kerma  $K_a$  was measured in the experiment. For this reason, the determined exponential coefficients are called apparent Kerma attenuation co-

efficient (AKAC) in the following. A connection between the photon fluence and the Kerma is given by the energy-dependent fluence-to-kerma conversion coefficient  $\alpha(E)$  [95]. A relationship between the Kerma transmission and the AKAC can be described with:

$$\frac{K_a(d)}{K_a(0)} = \frac{\int_{E_0}^{E_{\max}} \phi(d, E) \cdot \alpha(E) dE}{\int_{E_0}^{E_{\max}} \phi(0, E) \cdot \alpha(E) dE} \approx \exp(-AKAC \cdot d), \quad (3.1)$$

where  $E$  describes the photon energy. Because  $\alpha$  depends only slightly on the energy for the considered energy range, this is an appropriate approximation.

Accordingly, for the following evaluations, exponential functions were fitted on the measured, respectively simulated transmission data with a linear least squares algorithm (weighted by the standard deviation of the measured, respectively simulated transmission values) using the software SciPy [96].

The samples with reduced infill densities have been treated separately because the fully printed boundaries (as shown in Fig. 3.1 b and c) have an influence on the attenuation parameters. Without a correction, the AKACs for the investigated samples would have been overestimated. To assess the AKAC for the inner structure only,  $AKAC_i$ , the following relationship between the transmission of X-rays for the two samples with different total thicknesses ( $d_1, d_2$ ) but equal boundary thickness ( $d_b$ ) was used. The X-ray transmission is affected by a coefficient for both the fully printed boundaries  $AKAC_b$  and the coefficient for the inner structure  $AKAC_i$ :

$$\frac{T(d_1)}{T(d_2)} = \frac{\exp(-2AKAC_b d_b - AKAC_i d_{i1})}{\exp(-2AKAC_b d_b - AKAC_i d_{i2})}. \quad (3.2)$$

$d_{i1}$  and  $d_{i2}$  are the respective thicknesses of the inner structure. This results in the following relationship for  $AKAC_i$ :

$$AKAC_i = \frac{\ln(T(d_1)/T(d_2))}{(d_{i2} - d_{i1})}. \quad (3.3)$$

### 3.2.3 Investigation of absorption properties

To investigate the absorption properties of the printed material samples, the dose inside the materials was measured with TLDs. For this reason, six LiF TLD rods (TLD-100; Bicron-Harshaw, Cleveland, Ohio, USA) of the size  $1 \times 1 \times 6 \text{ mm}^3$  were inserted in the middle of the stack of all printed plates using the designated plate with the cavities (as shown in Fig. 3.1). Then, the whole material stack, including

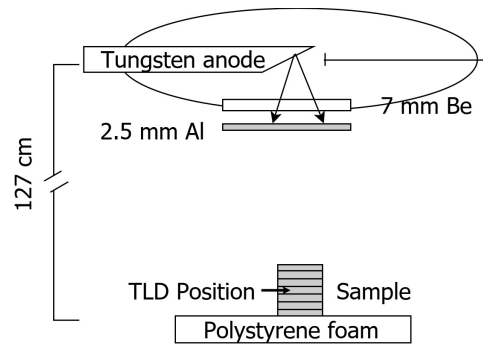


Figure 3.4: Wide beam setup for the measurement of the absorbed dose inside the printed sample materials with TLDs.

the TLDs, was irradiated in the centre of a wide X-ray beam using only the internal Be and a 2.5 mm Al filtration, as shown in Fig. 3.4. The same radiation qualities as for the attenuation analysis were investigated. The sample stack was placed on a low-density polystyrene foam to avoid backscattering from the floor. The distance between the focus of the X-ray tube and the material stack was 127 cm. Irradiation was performed for a tube current of 10 mA and a time of 2 min. For each measurement, a new set of TLDs was inserted. For the following evaluations, the mean dose of all six TLDs was used, and the standard deviation was used for uncertainty analysis.

### 3.2.4 TLD processing

All TLDs used for measurements in this thesis were subjected to the following steps: For a preparatory step, the dosimeters were annealed before the measurements to remove any residual signal in a TLD-oven (TLDO 1321, PTW, Freiburg, Germany) according to the standardized protocol: heating up to 400 °C, holding for 20 minutes, cooling down to 100 °C, holding for 10 minutes, cooling down to 45 °C. After that, they were subjected to ionizing radiation in the actual measurements. Five days after the irradiation, the TLDs were pre-annealed (heated up to 100°C, held for 10 minutes, and cooled down to 45°C). The luminescence signal was scanned with a Harshaw TLD 5500 reader (Thermo Fischer Scientific, Waltham, Massachusetts, USA) at a temperature of 300°C (reached with a heating rate of 15 °C/s) for an acquisition time of 20 s.

Each TLD-crystal was individually calibrated by irradiation with an X-ray tube (Isovolt 400) for the same radiation qualities as used in the experiments. The cali-

bration dose (dose in water,  $D_W$ ) was assessed with a stem chamber (M2331) and the dosimeter (UNIDOS E). A temperature and pressure correction of the chamber was performed before irradiation, as well as a radiation quality correction of the measured dose by using the chamber's radiation quality correction term  $k_q$ , interpolated to the used tube voltages. The same TLD-protocol used for the experimental measurements was followed for the calibration step.

### 3.2.5 Monte-Carlo simulations for obtaining tissue reference values

The respective AKAC and dose values for human tissues were generated with MC simulations. Therefore, both experimental setups described above were simulated in the geant4 toolkit (Geant4 10.5; Geant4 Collaboration, [97]). All simulations were performed on a Linux virtual machine with 40 central processing units (CPU) (Intel® Xeon® CPU E5-2687W v3 @ 3.10 GHz; Intel, Santa Clara, California, USA), using initial photon energies according to the spectra of the experiments calculated with the software xpecgen [98]. Rayleigh scattering was neglected in the simulations, which has no further influence on the attenuation behaviour (cf. section 2.4.3). The sample materials were exchanged to the reference tissues, for which mass densities and elemental compositions are given in table 3.2 [92, 93]. In this context, bulk soft tissue is a general substitute for soft tissues, as proposed in ICRP publication 89, e.g., for glands, trachea or the uterus.

For obtaining simulated AKAC values, the kerma transmission of photons was received by scoring the energy-dependent photon fluence  $\phi$  and transferring it with the kerma conversion coefficients  $\alpha$  into the air Kerma  $K_a$  according to the following relationship:

$$K_a = \sum_E \phi(E) \cdot \alpha(E). \quad (3.4)$$

For each material, tissues with the same thickness as the printed samples were simulated to achieve comparable attenuation curves on which exponential curves were fitted according to eq. 3.1. Each simulation was done with  $10^8$  initial particles, for which the relative error was below 1%. A single simulation took around 1 h.

The absorbed dose values inside the reference tissues were directly scored in a simulated LiF TLD crystal (located in the middle of the tissue) with the dose deposit scorers implemented in the geant4 code. Considering the wide X-ray field, in this case, more initial particles and, consequently, longer simulation time was needed to

achieve statistically stable results. The beam angle was set to  $10^\circ$  (instead of  $20^\circ$  as in the real X-ray tube) to decrease the computing time, which did not influence the results. Additionally, only one instead of six TLDs was simulated with a size of  $12 \times 6 \times 1 \text{ mm}^3$ . For these simulations,  $10^9$  initial photons were simulated (with a computation time of around 4 h), for which relative errors below 5% were achieved. Each simulation was repeated six times and mean values were used for further evaluations. The respective tissues were simulated for each material with the same thickness as the sample stacks in the experiments. Because simulated dose values depend on simulation parameter like the particle flux, for a numerical comparison of the simulated and measured dose values, simulated values need to be scaled. Therefore,  $D'_{\text{sim}}$  values were calculated with a calibration factor, determined by the air Kerma measured in the experimental setup,  $K_{\text{meas}}$ , and the air Kerma simulated for the same setup under consideration of the conditions previously described,  $K_{\text{sim}}$ :

$$D'_{\text{sim}} = D_{\text{sim}} \cdot \frac{K_{\text{meas}}}{K_{\text{sim}}}. \quad (3.5)$$

Table 3.2: Mass densities and atomic compositions of simulated reference tissues.

Tissue	Mass density g/cm <sup>3</sup>	H	C	N	O	Na	Mg	P	S	Cl	K	Ca
Lung <sup>a</sup>	0.38	10.5	8.3	2.3	77.9	0.2	0.1	0.2	0.3	0.2	0.0	0.0
Adipose <sup>b</sup>	0.95	11.4	59.8	0.7	27.8	0.1	0.0	0.0	0.1	0.1	0.0	0.0
Skeletal muscle <sup>b</sup>	1.05	10.2	14.3	3.4	71.0	0.1	0.0	0.2	0.3	0.1	0.4	0.0
Bulk soft <sup>b</sup>	1.03	10.5	25.6	2.7	60.2	0.1	0.0	0.2	0.3	0.2	0.2	0.0
Cortical bone <sup>b</sup>	1.92	3.4	15.5	4.2	43.5	0.1	0.2	10.3	0.3	0.0	0.0	22.5
Spongiosa <sup>a</sup>	1.31	7.8	24.8	3.9	52.5	0.1	0.2	3.4	0.3	0.0	0.1	6.8
Cartilage <sup>b</sup>	1.1	9.6	9.9	2.2	74.4	0.5	0.0	2.2	0.9	0.3	0.0	0.0
Glandular breast <sup>b</sup>	1.04	10.2	18.4	67.7	3.7	0.0	0.0	0.0	0.0	0.0	0.0	0.0
Fetal cortical bone <sup>c</sup>	1.58	5.2	14.3	3.9	51.7	0.1	0.1	7.7	0.2	0.1	0.0	16.7

<sup>a</sup>[93]

<sup>b</sup>[92]

<sup>c</sup>[99]

### 3.2.6 Conditions for tissue equivalence

To rate the tissue equivalence of the materials, relative differences,  $\delta$  (%), between material and tissue properties were calculated, considering simulated values  $v_{\text{sim}}$  on reference tissues and measured values  $v_{\text{meas}}$  on 3D-printed samples:

$$\delta = \left( \frac{v_{\text{meas}}}{v_{\text{sim}}} - 1 \right) \cdot 100. \quad (3.6)$$

The criteria for tissue equivalence was set to  $\delta \leq \pm 5\%$  because of the uncertainties affecting measurements, i.e., the correct placement of the ionization chamber in the focus of the pencil beam, uncertainties of TLDs and ionization chambers, or instability of the X-ray tube.

### 3.2.7 Validation process

For a general validation process of the experimental and computational methods, detailed investigations on PMMA were performed. PMMA was chosen because it is characterized as a well-defined water substitute. In this process, a comparison of the attenuation behaviour of printed and conventionally produced PMMA samples was made.

For the AKAC values, an independent validation was performed by a comparison to reference values based on literature data of the NIST database [17]. For this process, a conversion of the provided mono-energetic attenuation values into AKAC values was necessary, as described in the following:

For each energy bin of the X-ray spectra used for the simulations,  $E$ , the individual attenuation coefficients provided by NIST,  $\mu(E)$ , were collected for the elemental composition of PMMA ( $C_5O_2H_8$ ). With the density of PMMA,  $\rho$ , the photon fluence,  $\phi$ , (provided by the spectral data of xpecgen), and the kerma conversion coefficients,  $\alpha$ , mean kerma transmission ratios were determined for different PMMA thicknesses  $d$  with the following relationship:

$$T = \frac{K_a(d)}{K_a(0)} = \frac{\sum_E (\alpha(E) \cdot \phi(E) \cdot \exp(-\rho \cdot \mu(E) \cdot d))}{\sum_E (\alpha(E) \cdot \phi(E))}. \quad (3.7)$$

On the attenuation curves determined with this relationship, the AKAC values were specified by monoexponential fits according to eq. 3.1.

To validate the simulation methods, AKAC values were also determined on the

simulated transmission of X-rays through PMMA, simulated with the corresponding elemental composition and density ( $1.18 \text{ g/cm}^3$ ).

The influence of beam hardening effects on the AKAC values was investigated in a separate step for the example of cortical bone as a tissue with high density and atomic number  $Z$  (as provided in Tab. 3.2). In lack of a well-defined cortical bone equivalent material that can be used for measurements, this was only performed for the simulation by comparing the simulated values with the NIST-based values.

The validation with literature-based reference values was impossible for the absorbed dose values because they depend on the specified setup and radiation qualities used in the experiments. Hence, the validation step was limited to comparing measured and simulated values only, which was also done for the example of PMMA.

The energy dependence of  $\delta$  was also validated for the examples of PLA and PMMA, for which  $\delta$  between simulated material and tissue values were calculated.

#### 3.2.8 Analysis of CT densities

In addition to the analysis of the tissue equivalence as described above, the CT densities of the various FDM filament and epoxy-resin samples were also analysed. One slice of each material sample set was scanned in an axial scan mode on a clinical CT device (GE BrightSpeed 16; General Electrics, Boston, Massachusetts, USA) with 100 kV tube voltage and 200 mA tube current (slice thickness, 0.63 mm; voxel size  $0.19 \times 0.19 \times 0.63 \text{ mm}^3$ ). The homogeneity of the CT images of the relatively small objects in air was previously secured by a comparison to CT density measurements of selected samples in a water phantom.

The CT density of each sample was measured with the software ImageJ [100] on iteratively reconstructed images (standard convolution kernel) in rectangular region of Interest (ROI)s. For an uncertainty analysis, the standard deviation of CT densities over the respective ROI was used. This is directly affected by the infill density and printing accuracy and is therefore a measure for the homogeneity of printed samples. The CT densities of all samples were compared to typical CT densities of relevant kinds of tissues [101, 102].

### 3.2.8.1 Influence of printing settings

To investigate the influence of several printing settings on the CT density of printed samples, cubic samples with  $3 \times 3 \times 3 \text{ cm}^3$  were printed on an industrial FDM printer (3ntr A2 V4, 3ntr, Oleggio, Italy) with PLA (snowwhite PLA, filamentworld) and a 0.6 mm nozzle with various settings in the Cura slicing software. Furthermore, the samples were printed without wall lines and top and bottom surfaces, as shown in Fig. 3.5, to exclude a possible influence of those lines.

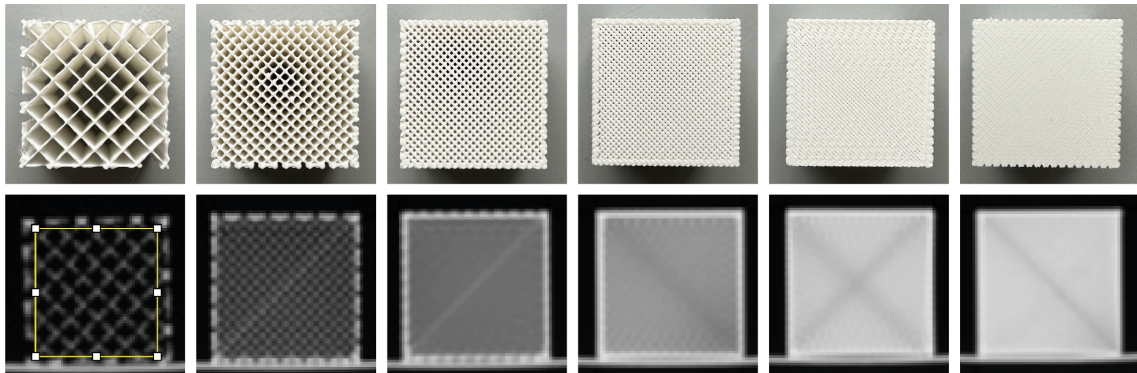


Figure 3.5: Upper row: cubic samples of series 3 with different infill densities (15 %, 35 %, 55 %, 75 %, 95 % and 100 %) printed without boundaries and surfaces. Lower row: CT images and the ROI used to estimate the CT densities and standard deviations (center -350 HU, width 1300 HU). The artefacts are reasoned in the printing scheme.

Besides the infill density, for which the same line infill structure as previously used was chosen, the influence of the print speed, the layer thickness and the location on the build plate were investigated. It was distinguished between two production modes: for the parallel mode, all samples were printed in one step with, in consequence, different locations on the print bed. For the serial mode, all samples were printed one after the other at the same location. The dependence on the distance from the centre was further characterized by samples printed on a diagonal line from the top left to the bottom right going through the centre of the build plate. The samples used to investigate the lung tissue equivalence (cf. section 3.2.1) printed on a different 3D-printer (Ultimaker 2+) were also considered in this analysis. The exact printing settings for each sample series are summarized in Tab. 3.3. All series were scanned on the same CT device (GE Brightspeed) and with the same settings as used for the investigation of CT densities as described in section 3.2.8.

Table 3.3: Cubic sample series with different printing settings for investigating the influence on the CT densities.

Series Nr.	Infill densities	Print Speed	Layer Height	Processing Mode	Printer	Distance from the print bed center (x-, y-direction)
	%	mm/s	mm			cm
Series 1	15, 25, 35, 45, 55, 65, 75, 85, 95, 100	80	0.2	parallel	3ntr	(-6.3, 6.3), (0, 6.3), (6.3, 6.3), (-6.3, 0), (0,0), (6.3, 0), (-6.3, -6.3) (0, -6.3), (6.3, -6.3), (-6.3, -12.72), respectively for the different infill densities
Series 2	15, 25, 35, 45, 55, 65, 75, 85, 95, 100	40	0.2	parallel	3ntr	as above
Series 3	15, 35, 55, 75, 95, 100	40	0.2	serial	3ntr	(0,0)
Series 4	25,30,35,40,45	30	0.1	serial	UM2+	(0,0)
Series 5	100	20, 40, 60, 80	0.2	serial	3ntr	(0,0)
Series 6	100	20, 40, 60, 80	0.1	serial	3ntr	(0,0)
Series 7	100	60	0.1	diagonal	3ntr	(-12.7, 12.7), (-6.3, 6.3), (0,0), (6.3, -6.3), (12.7, -12.7)

## 3.3 Results

### 3.3.1 Validation process for the assessment of the tissue equivalence

The general attenuation curves, as they were measured on all investigated materials for the determination of the AKAC values, are shown for each radiation quality for the example of unprinted PMMA in Fig. 3.6 a. The linear dependence between kerma transmission and absorber thickness  $d$  in the semi-logarithmic scale proves the good approximation with a mono-exponential function for the used radiation qualities (even if they were spectral and not mono-energetic). This proves the approximation for the determination of AKAC values in equation 3.1 for the example of a low-density material.

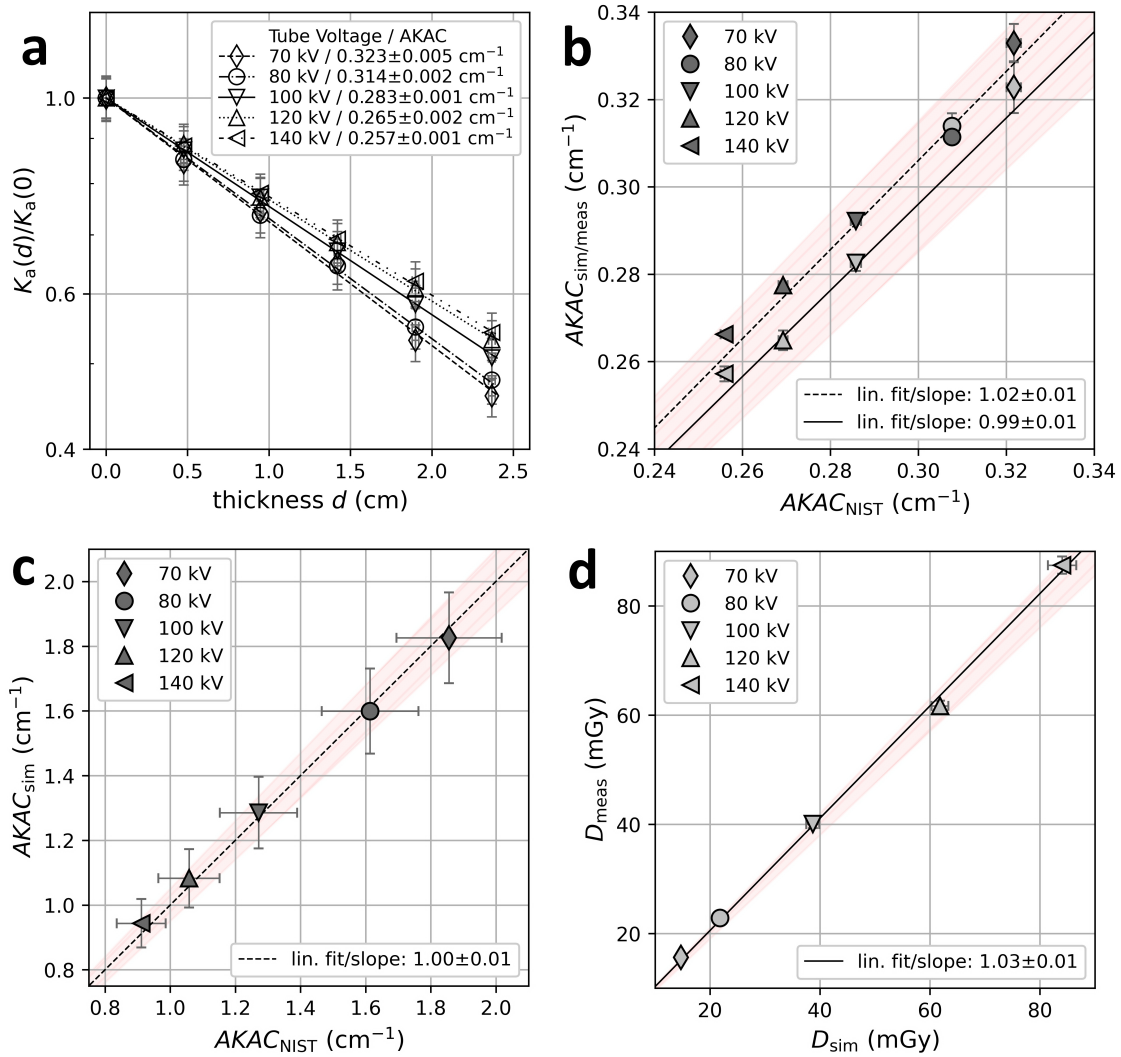


Figure 3.6: Validation results. a) shows the transmission curves on PMMA, the lines represent exponential regressions in order to determine the AKAC values b) shows the linear correlation of simulated (dark symbols), respectively measured (light symbols) AKAC values with NIST-based values for the example of PMMA. c) shows the linear correlation between simulated AKAC values and NIST based values for the example of cortical bone. d) shows the linear correlation between the measured absorbed dose and the dose simulated inside PMMA. All values are given with their standard errors. The red areas represent regions of  $\pm 5\%$  difference from the line of identity.

The AKAC values themselves were validated by a comparison of the values obtained in measurements respectively simulations with the NIST based reference data, as shown in Fig. 3.6 b. The linear regression analysis of both simulated

and measured values for all investigated energies shows the high agreement with the literature-based values. The regression slope indicates that simulated values are averaged over all investigated radiation qualities 2% larger than the NIST-based values, while measured AKAC values are 1% lower. Considering the various uncertainties for simulation and measurement methods, this is an excellent agreement, which proves the simulated values to be suitable reference values for assessing the tissue equivalence of materials.

The previously mentioned beam-hardening effects on the attenuation curves and the AKAC values were investigated for the example of cortical bone in detail. The linear correlation of the AKAC values determined from simulated transmission curves on the cortical bone composition and for the reference NIST-based values is shown in Fig. 3.6c. There is an almost perfect agreement of the values (with a linear regression slope of  $1.00 \pm 0.01$ ), which proves the suitability method for the determination of AKAC values also for the high-density materials. However, owing to more significant deviations from the mono-exponential function, the approximation with the Lambert-Beer law leads to larger uncertainties for the exponential fit-coefficients, i.e. the AKAC values. This is visible in larger error bars for both simulated and NIST-based values.

Also, the measurement and simulation methods for obtaining the dose inside tissues and materials were validated on the example of PMMA. Because no literature-based values are available for the specific experimental setup, a comparison between both simulated and measured dose values serves as validation. The measured values tend to be 3% higher than the simulated values, as shown in the linear regression analysis in Fig. 3.6d. However, this is below 5%, which is an acceptable agreement because of the general uncertainties of both methods. For post-calibration, this difference was considered in the simulated values for further evaluation.

### 3.3.2 Overview of attenuation and absorption properties

The attenuation and absorption properties of all investigated materials and tissues are summarized in Fig. 3.7 for a representative tube voltage of 100 kV. The AKACs of the investigated printing materials cover a broad range between  $0.5 \text{ cm}^{-1}$  for PLA samples with decreased infill density and  $10.2 \text{ cm}^{-1}$  for the metal-filled composite filaments. As expected, the AKAC increases with higher infill densities and a higher amount of hydroxyapatite in the epoxy resin samples.

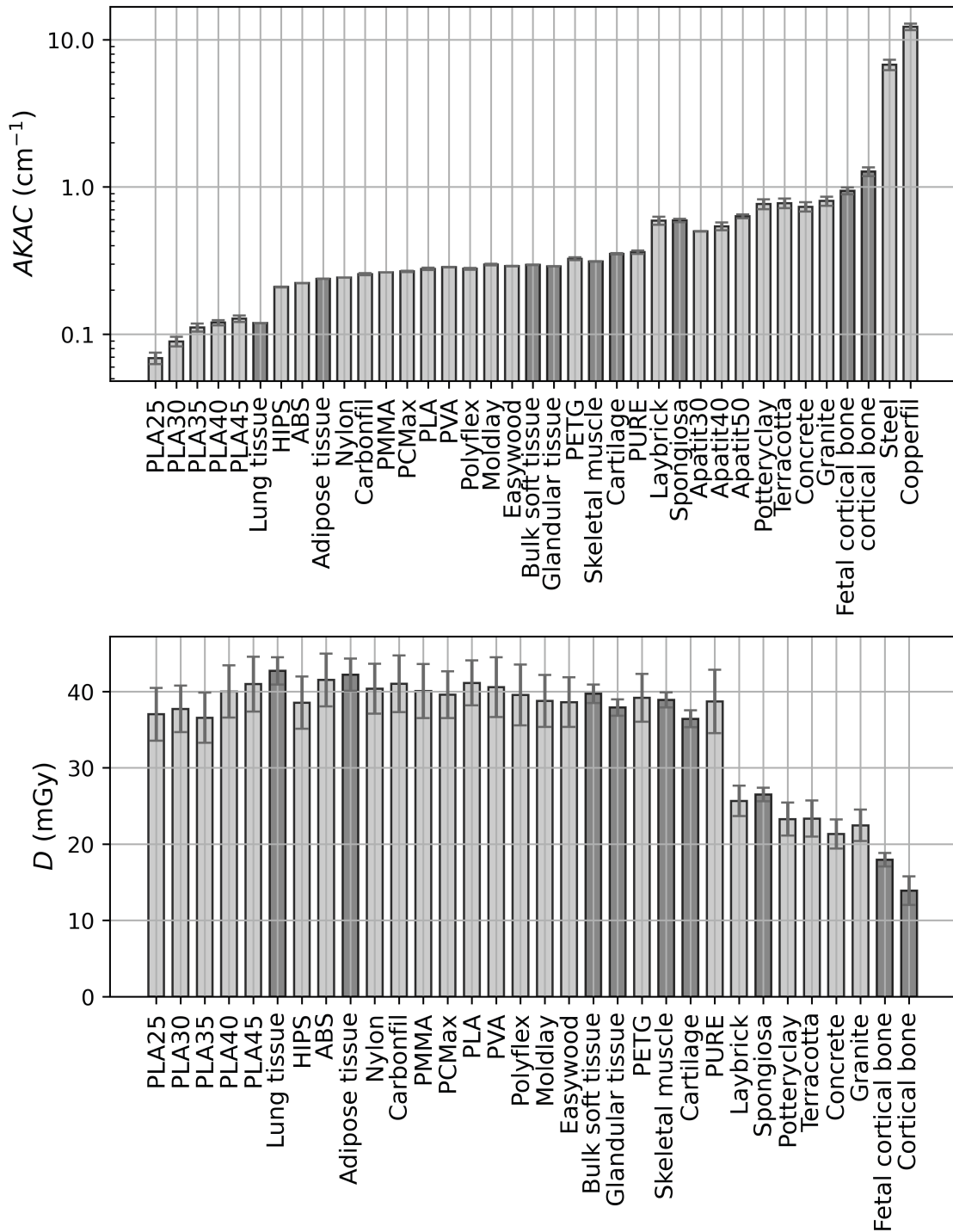


Figure 3.7: Above: AKACs determined for investigated 3D-printing materials in measurements (light grey bars) and for tissues in MC simulations (dark grey bars) on a logarithmic scale for a tube voltage of 100 kV. The errorbars give the standard deviation of the exponential fit coefficient. Below: Absorbed doses in printing materials (light grey bars) and tissues (dark grey bars) for a tube voltage of 100 kV. The errorbars give the standard deviations of individual TLDs, respectively, simulation runs.

The AKACs of all considered tissues cover a similar range as the investigated materials, except for cortical bone, which is neither similar to the stone nor the metal-filled materials.

The doses measured inside most printed samples are between 20 and 40 mGy for the representative tube voltage of 100 kV and similar to the dose simulated in soft tissues and spongiosa. There is generally less variation in the measured values because the dose depends not directly on the mass density unlike the attenuation behaviour. The dose simulated in cortical bones is markedly lower, e.g., at 15 mGy for adult cortical bone. In contrast, the doses measured inside the printed samples made of metal-filled filament are still much lower, with 7.2 mGy in the case of the stainless steel material and 2.1 mGy in the copper-filled material. These values are not presented in Fig. 3.7 reasoned by the significantly different sample depth in which the dose was measured compared to the other samples (3.4 mm instead of 13 mm for non-metal samples).

#### 3.3.2.1 Non-printed polymers and different manufacturers

Whether there is a difference between the attenuation behaviour of 3D-printed samples and conventionally produced material samples was investigated for the example of PMMA. Therefore, AKAC values determined for 3D-printed PMMA samples were compared with AKAC values of conventionally produced PMMA plates.

The mass density has a critical influence on the attenuation behaviour. The density of conventional PMMA samples is  $1.18 \pm 0.2 \text{ g/cm}^3$ . In contrast, the density is significantly lower for the printed samples ( $1.12 \pm 0.2 \text{ g/cm}^3$ ). Consequently, the AKAC of the printed sample is about  $6 \pm 0.01 \%$  lower than for the conventional samples. Nevertheless, the AKAC normalized by the mass density is the same for both PMMA samples under consideration of the uncertainties. This indicates no relevant difference in the elemental composition of both PMMA types. The only critical influence for this example is the mass density, which is influenced by the printing settings.

Another possible difference might be between filament materials of different manufacturers or colors. This effect was investigated in example of PLA filaments (golden PLA [Filamentworld], transparent PLA [Avistron]). The mass density of fully printed samples is within the uncertainties equal for both PLA filaments. Consequently, the AKACs are also equivalent to each other. Therefore, there seems to be no relevant difference in the elemental composition owing to the color particles in

these filaments. However, a more detailed analysis considering more manufacturers and colors is recommended.

### 3.3.3 Individual evaluation of tissue equivalence

For a more detailed evaluation of the tissue equivalence, the relative differences  $\delta$  between measured AKAC respectively, dose values for the printed samples and the simulated values on reference tissues will be discussed in the following section for all investigated tube voltages (70-140 kV). The energy dependence of the tissue equivalence is presented for the five most relevant tissues (lung, adipose, skeletal muscle, spongiosa and adult cortical bone) for chosen materials in the following. Besides a summary of these results, the analysis results for the other investigated tissues (glandular tissue, cartilage and fetal cortical bone) are presented in Tab. 3.4 and 3.5 below.

#### Lung tissue

For lung tissue, the  $\delta$  for both properties are shown in Fig. 3.8.

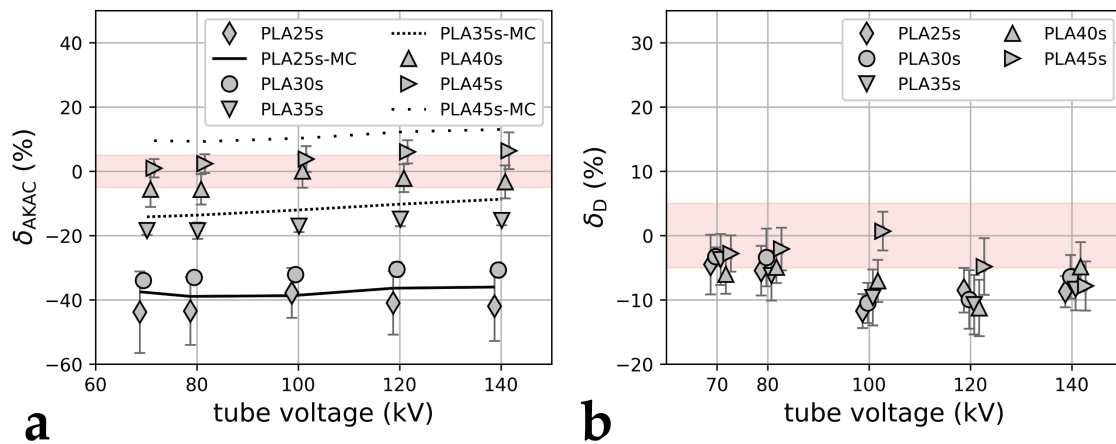


Figure 3.8: Relative differences,  $\delta$ , of AKAC and dose values measured on printed materials with low infill densities and simulated reference values on lung tissue in dependence of the tube voltage. The lines represent the  $\delta$  of values simulated on the elemental composition of PLA with the respective mass density of the sample (but homogeneous material distribution). The red area demonstrates a difference of  $\pm 5\%$ , for which tissue equivalence was assumed. The errors were determined with Gaussian error propagation.

The PLA samples with 40 and 45% infill density are within the range of tissue equivalence for the AKAC values over the whole energy range. The samples with lower infill densities show a significantly lower attenuation behaviour than the simulated lung tissue. The doses inside all printed samples are equal to each other when considering the uncertainties, which was expected by the physical definition of the dose that is independent of the mass density. All samples are scarce within the range of tissue equivalence for this property with  $\delta$  of  $-5\%$ . For both properties, there is no significant energy dependence.

A discrepancy is shown for the  $\delta$  of attenuation values of the simulated material values, for whose the same mass density of the printed material samples was considered, however, with a homogeneous material distribution instead of the line structure (data are represented by lines in Fig. 3.8 a). The simulated material values show up to 10% higher attenuation values than the ones measured on actual samples with the inhomogeneous material distribution. To analyse whether this issue depends on differences in the mass density or the inner structure of the printed samples itself, the linear correlations of the mass density, respectively, the AKAC values of the printed samples with the corresponding infill density are shown in Fig. 3.9.

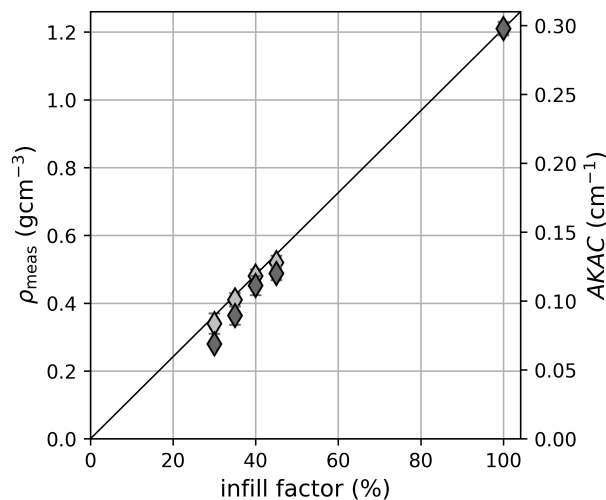


Figure 3.9: Linear correlation between mass densities (light symbols on the left axis), respectively AKAC values (measured for 100 kV tube voltages, dark symbols on the right axis) with the nominal infill densities measured on PLA samples with reduced infill density. The linear function shows the line of identity. Errorbars give standard deviations.

There is a perfect linear correlation between the mass density and the infill factor.

Nevertheless, the measured AKAC values do not correlate exactly with the mass density and are slightly lower than what would have been expected when the mass density has the only impact on the attenuation behaviour.

For this reason, the attenuation behaviour may be not only impaired by the mass density itself but also by the inhomogeneous infill structures in the pencil beam setup. This assumption is supported by the result of AKAC values measured on samples aligned with the infill structure parallel instead of perpendicular to the beam direction, which are up to 10 % lower.

### Adipose tissue

The results of investigations for the adipose tissue equivalent materials are shown in Fig. 3.10.

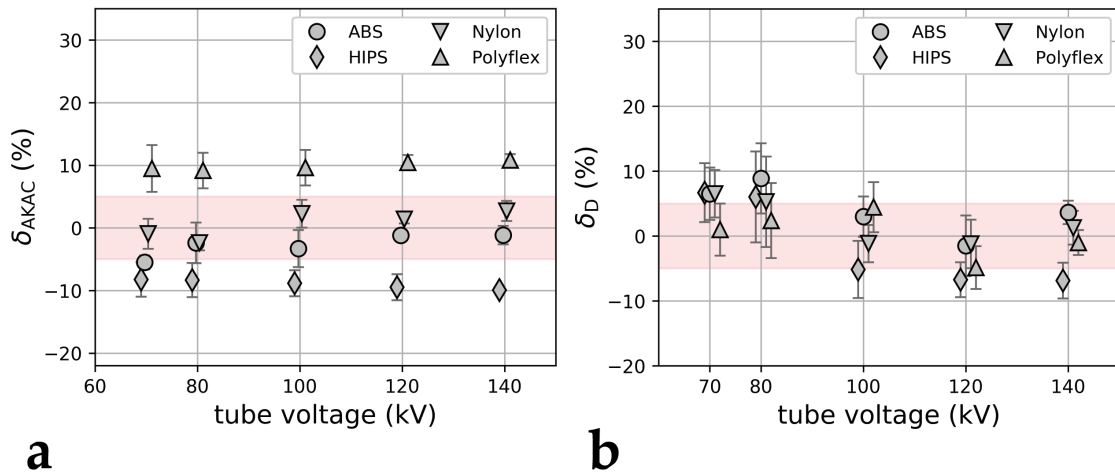


Figure 3.10: Relative differences,  $\delta$ , of AKAC and dose values measured on selected printing materials and simulated on adipose tissue in dependence of the tube voltage. The red area demonstrates a difference of  $\pm 5\%$ , for which tissue equivalence was assumed. The errors were determined with Gaussian error propagation.

The  $\delta$  for AKAC values of two materials, ABS and Nylon, are within the range of tissue equivalence over the whole investigated energy range. Polyflex shows a slightly higher and high impact polystyrene (HIPS) a slightly lower ( $\delta \leq \pm 10\%$ ) attenuation behaviour than adipose tissue. However, in terms of the absorption behaviour, all four materials fulfil the condition of tissue equivalence for all tube voltages, as shown in Fig. 3.10 b. Furthermore, the  $\delta$  of all materials considered have no distinct energy dependence for both properties.

### Skeletal muscle and bulk soft tissue

Because of the similarity of skeletal muscle and bulk soft tissue in their atomic composition and density, the same materials were included in a closer examination of the tissue equivalence for both. The  $\delta$  for the AKAC and absorbed doses are presented in Fig. 3.11 a and b for muscle, respectively c and d for bulk soft tissue.

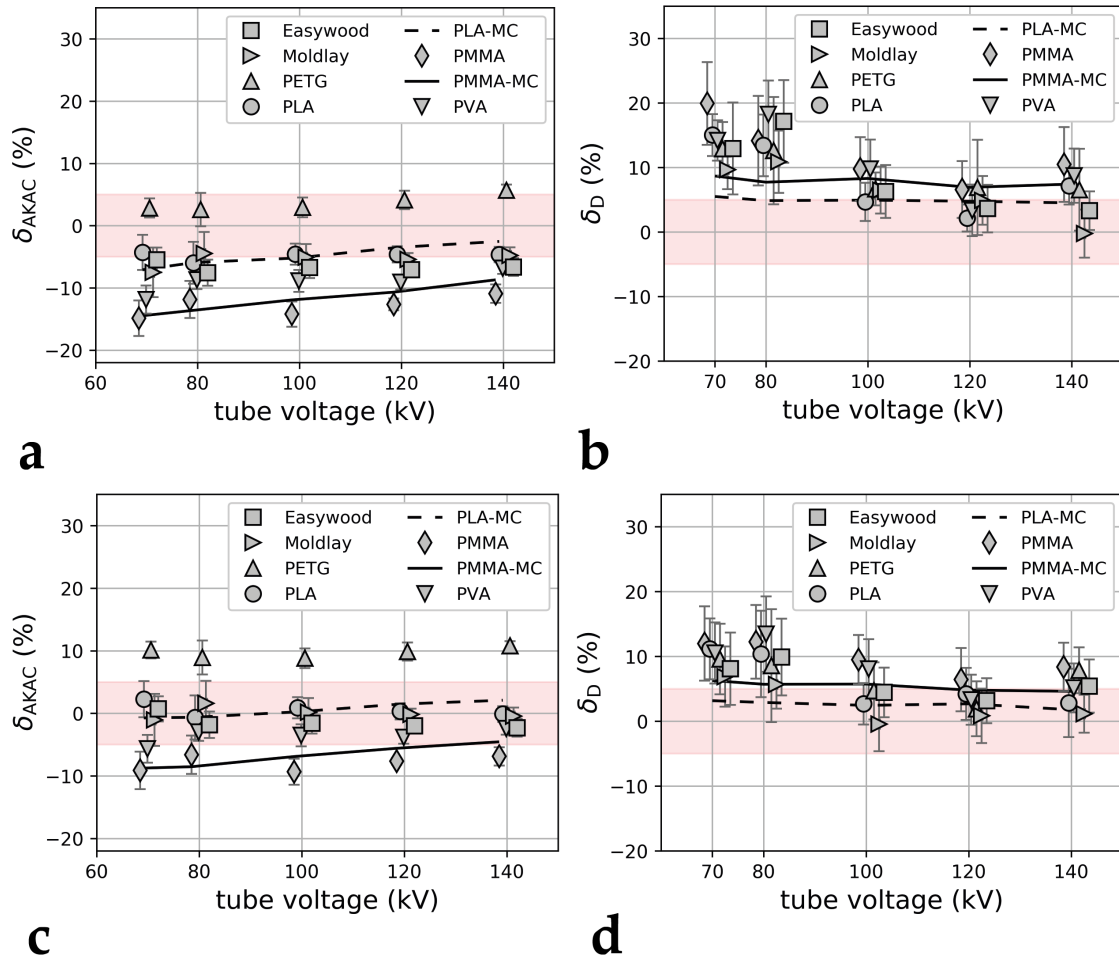


Figure 3.11: Relative differences,  $\delta$ , of AKAC and dose values measured on selected printing materials and simulated on skeletal muscle (a and b) and bulk soft tissues (c and d) in dependence of the tube voltage. The lines represent  $\delta$  between values simulated for the individual material composition and density and the individual tissue for additional validation of the energy dependence. The red area demonstrates a difference of  $\pm 5\%$ , for which tissue equivalence was assumed. The errors were determined with Gaussian error propagation.

This analysis shows that the four materials, Easywood, Moldlay, PLA, and PVA,

have very similar AKAC values and thus similar attenuation behaviours. All of these are in the range of tissue equivalence for both kinds of tissues for all investigated radiation qualities. However, the AKAC values for bulk soft tissue are around 5% lower in comparison to muscle tissue but still in the range of tissue equivalence. In contrast, polyethylenterephthalat + glycole (PETG) is a material equivalent to skeletal muscle that shows slightly higher attenuation behaviour (Fig. 3.11 a). Compared to the other materials shown, PMMA has the lowest attenuation behaviour and is not in the range of tissue equivalence, neither for muscle nor for bulk soft tissue. All materials considered have a slight energy dependence of  $\delta$  between measured and simulated doses, as shown in Fig. 3.11 b and d, with larger absolute  $\delta$  for lower energies.

Under consideration of the uncertainties, the dose measured in all materials is equal to each other. For bulk soft tissue, all materials show equivalent dose absorption properties over the whole energy range. In the case of muscle tissue, the  $\delta$  are in the range of +5% only for tube voltages above 100 kV. The reference simulations on PMMA and PLA shown as lines in both plots confirm the  $\delta$  of measured values on the materials for both properties and tissues but show a less distinct energy dependence in the case of the  $\delta$  for dose values. Taking this into account, as well as the non-negligible uncertainties of the methods, it can be assumed that PLA and other materials are equivalent to muscle tissue in case of the absorption behaviour also for the energy range below 100 kV. In summary, several materials, e.g. Easywood, PLA, and others, have similar behaviours. All these materials are possible equivalent materials for bulk soft tissue in both relevant properties. The slightly larger attenuation behaviour of muscle tissue in comparison to bulk soft tissue was represented with these materials and additionally by PETG under consideration of the general uncertainties.

### **Spongiosa**

Composite materials, including stone powder, were considered in detail for the investigation of equivalents for spongiosa (and cortical bone) owing to their generally higher attenuation behaviour in comparison to the non-composite polymer materials.

The  $\delta$  for both properties, the attenuation and absorption of X-rays, are shown for spongiosa in Fig. 3.12. The  $\delta$  between the AKAC values of stone-filled materials and spongiosa, as shown in Fig. 3.12 a, show a slight energy dependence with higher

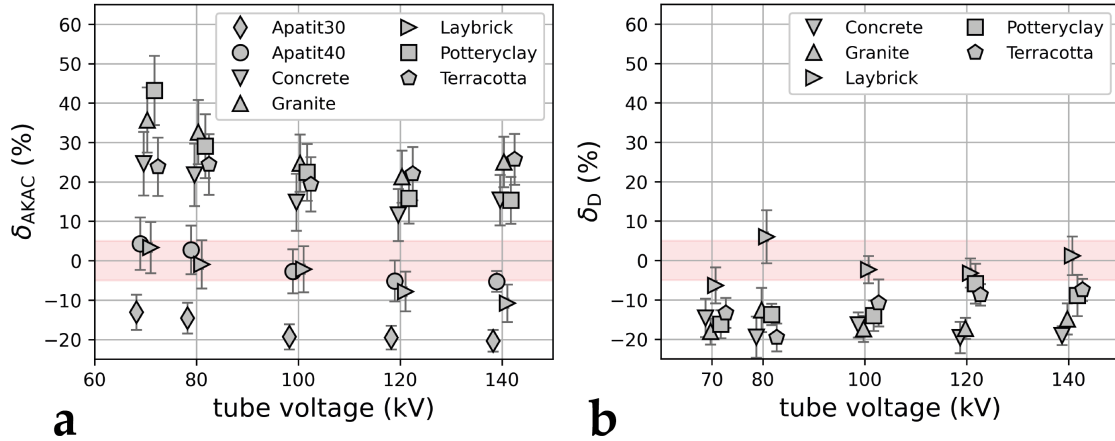


Figure 3.12: Relative differences,  $\delta$ , of AKAC and dose values measured on selected printing materials and resin mixtures and simulated on spongiosa in dependence of the tube voltage. The red area demonstrates a difference of  $\pm 5\%$ , for which tissue equivalence was assumed. The errors were determined with Gaussian error propagation.

differences for lower tube voltages. This indicates some differences in the atomic composition between the materials and spongiosa that lead to larger absolute  $\delta$  for lower tube voltages because of the high influence of the photo effect in this energy range. Potteryclay, Concrete, Terracotta, and Granite have, in principle, similar attenuation behaviour with each other, which might be reasoned by the fact that they are from the same manufacturer and might have no significant difference in their mass fractions of added powders. Nevertheless, all of them have distinct higher AKAC values than spongiosa and are no candidates for tissue equivalents.

In contrast, Laybrick complies with the condition for tissue equivalence for the whole investigated energy range and shows a less distinct energy dependence. Additionally, the results for the resin and hydroxyapatite mixtures (with hydroxyapatite mass fractions of 30 and 40 %) were analysed as possible spongiosa equivalents. Finally, Apatit40 shows the same attenuation behaviour as Laybrick and is also suited to imitate the attenuation behaviour of spongiosa. In contrast, the AKAC values of Apatit30 are significantly lower than those of spongiosa.

For the  $\delta$  between measured and simulated doses, the energy dependence is less distinct than for the AKAC for all considered materials. The absorbed dose inside the stone-filled materials is significantly lower than in spongiosa bone. However, the dose inside Laybrick is equivalent. Therefore, Laybrick is a suitable tissue equivalent material in both aspects. The absorption behaviour of resin mixtures was not

investigated.

### Cortical bone

In addition to stone-filled materials and hydroxyapatite samples for the investigation of tissue-equivalent materials for cortical bones, the metal-filled samples were also considered as candidates. The  $\delta$  for both, AKAC and absorbed dose stand out to have the highest energy dependence in comparison to the other tissues, which can also be explained by larger differences in the elemental composition and the big influence of the atomic number  $Z$  on the photoelectric cross-section (cf. Fig. 3.13). This is visible in the much larger  $\delta$  for lower tube voltages, respectively energies of X-ray photons. None of the investigated materials is even in a similar range to cortical bone, neither for the AKAC nor for the dose values.

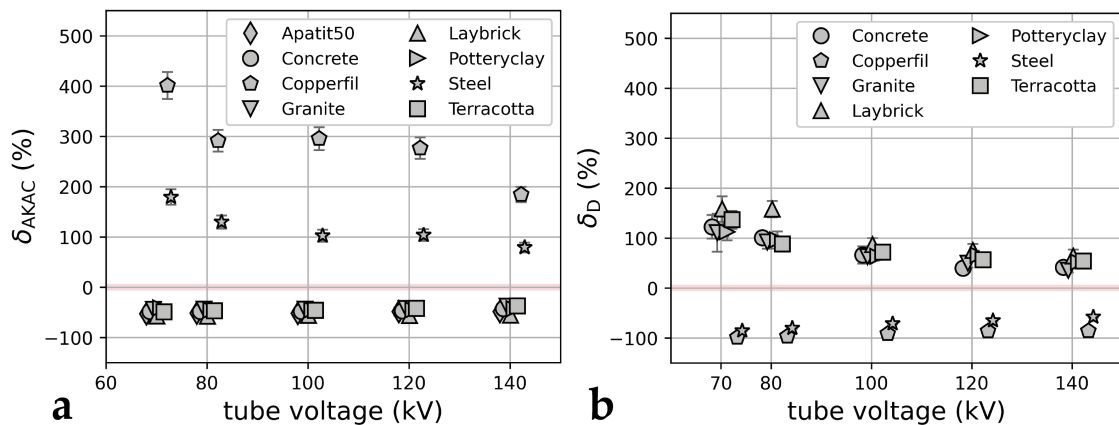


Figure 3.13: Relative differences,  $\delta$ , of AKAC and dose values measured on selected composite material and resin mixtures and simulated values on cortical bone in dependence of the tube voltage. The red area demonstrates a difference of  $\pm 5\%$ , for which tissue equivalence was assumed.

The stone materials are too low in their attenuation behaviour, and the metal filaments are magnitudes larger. Apatit50 shows a similar attenuation behaviour to the stone-filled materials and is also no suitable cortical bone equivalent material. The dose values are lower in metal filaments than in cortical bone and higher in printed stone materials. In general, the absolute  $\delta$  for the dose analysis are much smaller than for the analysis of the AKAC values in the case of the stone-filled materials.

#### Further relevant tissues

Because of the relevance for the further chapters of this thesis, some more specific kinds of tissues were also investigated to characterise the best tissue equivalent materials. The mean results of  $\delta$  for all investigated tube voltages and both properties are presented in Tab. 3.4 for soft tissues. The results for bone compositions are summarized in Tab. 3.5 for a representative tube voltage of 100 kV because of the more significant energy dependence. The energy dependence of  $\delta$  is not presented in detail because similar behaviours as for the previously investigated soft tissues, and bone compositions were found.

Glandular tissue is of particular interest for breast phantoms. Therefore it was investigated even if it is very similar to bulk soft tissue in density and atomic composition. Because of the minimal lower attenuation behaviour compared to the bulk soft tissue, PMMA is also suited as a tissue equivalent material for glandular tissue in addition to the materials already characterised as bulk soft tissue equivalents for both properties under consideration of the uncertainties.

Cartilage has a slightly higher AKAC than muscle, bulk soft tissue, and glandular tissue, while the absorbed dose is lower. Consequently, the materials found to be equivalent to soft tissues are not suited to represent cartilage and show mean  $\delta$  of up to  $-19\%$ . Pure and PETG are materials with slightly higher attenuation behaviour. However, only Pure is in the range of tissue equivalence for AKAC values. The dose inside these materials is higher than in the simulated cartilage tissue. Nevertheless, the absolute  $\delta$  were below  $10\%$ . The same yields for the  $\delta$  of AKAC between PETG and cartilage. In summary, none of the investigated materials shows tissue equivalence in both properties for this tissue, but the two materials mentioned fulfil the conditions for tissue equivalence the best and are under consideration of the uncertainties within a range of  $\delta < \pm 10\%$  which is sufficient for many applications. Fetal cortical bones are characterised by a lower density and lower amount of Ca in comparison to adult cortical bones. Consequently, AKAC values are lower and the absorbed doses higher. Nevertheless, the stone- and metal-filled printing materials are also unsuitable tissue equivalents. However, the absolute  $\delta$  for both properties for fetal cortical bone are lower than for adult cortical bone.

Table 3.4: Relative differences (%),  $\delta$ , between measured properties (AKAC, dose, mass density) on printed materials (averaged over all tube voltages, errors are standard deviations of the mean) and simulated on tissues. Mean values were chosen because the energy dependence can be neglected for these tissues and materials. For each tissue, only selected materials are shown. For bold materials, the requirements for tissue equivalence are fulfilled for both AKAC and dose.

<b>Adipose Tissue</b>	<i>AKAC</i>	<i>D</i>	$\rho$	<b>Lung tissue</b>	<i>AKAC</i>	<i>D</i>	$\rho$	<b>Cartilage</b>	<i>AKAC</i>	<i>D</i>	$\rho$
HIPS	$-8.9 \pm 1.0$	$-4.5 \pm 5.6$	$-0.1 \pm 2.1$	PLA25	$-41.6 \pm 2.2$	$-7.8 \pm 2.6$	$-26.3 \pm 4.7$	PURE	$-1.0 \pm 2.2$	$8.0 \pm 1.8$	$10.0 \pm 1.5$
<b>ABS</b>	$-2.7 \pm 1.6$	$0.8 \pm 3.0$	$6.6 \pm 1.8$	PLA30	$-32.0 \pm 1.3$	$-6.7 \pm 3.1$	$-26.3 \pm 4.7$	PETG	$-7.6 \pm 2.2$	$10.5 \pm 3.6$	$11.8 \pm 1.5$
<b>Nylon</b>	$0.6 \pm 2.0$	$0.2 \pm 4.0$	$10.5 \pm 1.8$	PLA35	$-16.8 \pm 1.5$	$-7.7 \pm 2.5$	$7.9 \pm 4.7$	Easywood	$-17.2 \pm 8.9$	$7.5 \pm 3.0$	$5.5 \pm 1.5$
Carbonfil	$10.4 \pm 2.6$	$-0.7 \pm 3.1$	$22.1 \pm 2.1$	<b>PLA40</b>	$-3.3 \pm 2.2$	$-6.8 \pm 2.4$	$26.3 \pm 4.5$	PLA	$-14.2 \pm 1.5$	$10.7 \pm 3.8$	$10 \pm 1.5$
PMMA	$13.4 \pm 2.2$	$-0.2 \pm 2.4$	$17.9 \pm 2.0$	<b>PLA45</b>	$4.0 \pm 2.1$	$-5.8 \pm 2.3$	$36.8 \pm 4.5$	PVA	$-19.1 \pm 2.2$	$10.8 \pm 3.6$	$6.4 \pm 1.5$
PLA	$24.1 \pm 3.4$	$-3.7 \pm 2.4$	$27.4 \pm 2.2$								
Polyflex	$9.9 \pm 0.6$	$-2.8 \pm 3.0$	$22.6 \pm 2.2$								
<b>Bulk soft tissue</b>	<i>AKAC</i>	<i>D</i>	$\rho$	<b>Skeletal muscle</b>	<i>AKAC</i>	<i>D</i>	$\rho$	<b>Glandular tissue</b>	<i>AKAC</i>	<i>D</i>	$\rho$
Carbonfil	$-10.8 \pm 1.8$	$6.4 \pm 4.3$	$12.6 \pm 1.9$	Carbonfil	$-10.8 \pm 1.8$	$6.4 \pm 4.3$	$12.6 \pm 1.9$	Carbonfil	$-9.1 \pm 1.7$	$5.4 \pm 6.7$	$11.5 \pm 1.8$
PMMA	$-7.9 \pm 1.1$	$6.3 \pm 2.5$	$8.7 \pm 1.8$	PMMA	$-12.9 \pm 1.5$	$7.1 \pm 3.2$	$6.7 \pm 1.8$	<b>PMMA</b>	$-5.7 \pm 1.0$	$4.2 \pm 5.1$	$7.7 \pm 1.8$
PCMax	$-9.0 \pm 1.3$	$4.9 \pm 2.9$	$12.6 \pm 1.8$	PCMax	$-13.9 \pm 1.6$	$7.3 \pm 3.8$	$10.5 \pm 1.8$	PCMax	$-6.2 \pm 1.2$	$2.2 \pm 3.9$	$11.5 \pm 1.8$
<b>PLA</b>	$0.5 \pm 1.0$	$2.0 \pm 2.9$	$17.5 \pm 2.0$	<b>PLA</b>	$-4.8 \pm 0.6$	$5.3 \pm 4.8$	$15.2 \pm 2.0$	<b>PLA</b>	$4.7 \pm 2.1$	$2.6 \pm 5.0$	$16.3 \pm 2.0$
<b>PVA</b>	$-3.8 \pm 1.1$	$3.5 \pm 2.4$	$13.5 \pm 2.1$	PVA	$-9.1 \pm 1.6$	$6.1 \pm 3.4$	$11.3 \pm 2.1$	<b>PVA</b>	$-1.9 \pm 1.0$	$2.7 \pm 5.1$	$12.4 \pm 2.0$
Polyflex	$-19.5 \pm 1.9$	$4.1 \pm 4.2$	$13.1 \pm 2.0$	Polyflex	$-15.9 \pm 2.7$	$6.9 \pm 4.1$	$11.0 \pm 2.0$	Polyflex	$-9.4 \pm 2.2$	$4.0 \pm 5.1$	$12.0 \pm 1.9$
<b>Moldlay</b>	$0.0 \pm 0.9$	$-0.6 \pm 3.2$	$6.4 \pm 1.8$	<b>Moldlay</b>	$-5.5 \pm 1.1$	$3.3 \pm 3.8$	$4.4 \pm 1.8$	<b>Moldlay</b>	$2.0 \pm 1.0$	$0.75 \pm 4.8$	$5.4 \pm 1.8$
<b>Easywood</b>	$-1.4 \pm 1.1$	$2.4 \pm 1.5$	$12.6 \pm 1.8$	Easywood	$-6.7 \pm 0.7$	$5.0 \pm 4.6$	$10.5 \pm 1.8$	<b>Easywood</b>	$0.5 \pm 1.3$	$-0.4 \pm 3.8$	$11.5 \pm 1.8$
PETG	$9.7 \pm 0.7$	$3.2 \pm 2.3$	$19.4 \pm 1.9$	<b>PETG</b>	$3.6 \pm 1.2$	$6.1 \pm 2.7$	$17.1 \pm 1.9$	PETG	$12.2 \pm 1.4$	$2.5 \pm 5.1$	$18.3 \pm 1.8$
PURE	$18.2 \pm 4.1$	$-0.3 \pm 2.2$	$17.5 \pm 1.9$	PURE	$11.6 \pm 3.3$	$1.1 \pm 2.4$	$15.2 \pm 1.9$	PURE	$20.7 \pm 4.3$	$0.1 \pm 3.0$	$16.3 \pm 1.8$

Table 3.5: Relative differences (%),  $\delta$ , between measured properties (AKAC, dose, mass density) on printed materials (for a representative tube voltage of 100 kV, errors were determined by Gaussian error propagation) and simulated on different bone compositions. Because energy dependence cannot be neglected, results are only presented for one tube voltage. For each composition, only selected materials are shown. For bold materials, the requirements for tissue equivalence are fulfilled for both AKAC and dose.

<b>Adult cortical bone</b>	<i>AKAC</i>	<i>D</i>	$\rho$	<b>Fetal cortical bone</b>	<i>AKAC</i>	<i>D</i>	$\rho$
Laybrick	-55.8 ± 5.0	84.0 ± 12.4	-38.2 ± 1.0	Laybrick	-41.1 ± 0.7	59.0 ± 21.2	-24.9 ± 0.8
Concrete	-48.2 ± 5.7	65.2 ± 16.6	-18.0 ± 1.5	Concrete	-28.1 ± 2.0	29.0 ± 14.9	-0.6 ± 1.1
Granite	-43.7 ± 6.3	61.5 ± 12.5	-19.9 ± 1.5	Granite	-11.8 ± 22.0	37.4 ± 16.8	-2.5 ± 1.2
Apatit40	-58.8 ± 5.7		-27.1 ± 1.5	Apatit40	-40.1 ± 4.6		-11.4 ± 1.5
Apatit50	-51.9 ± 6.9		-20.3 ± 1.5	Apatit50	-32.8 ± 4.8		-3.2 ± 1.5
Steel	102 ± 12	-71.2 ± 12	15.6 ± 3.1				
Copperfil	295 ± 23	-91.6 ± 0.3	74.0 ± 0.9				
<b>Spongiosa</b>	<i>AKAC</i>	<i>D</i>	$\rho$				
<b>Laybrick</b>	-3.7 ± 5.0	-0.9 ± 4.2	-9.1 ± 1.5				
Granite	27.9 ± 5.4	-16.01 ± 2.0	17.6 ± 2.3				
Concrete	17.6 ± 4.8	-17.8 ± 2.0	19.8 ± 2.3				
Pottery clay	25.2 ± 10.3	-11.7 ± 3.7	15.3 ± 2.3				
Terracotta	23.1 ± 2.2	-12.0 ± 4.2	16.8 ± 2.3				
Apatit40	-1.2 ± 4.0	±	±				

### 3.3.4 Analysis of CT densities

The individual CT densities of all investigated materials for a scan with 100 kV tube voltage are shown in Fig. 3.14 together with the typical CT density range for the relevant human tissues. In general, the CT densities of the materials behave as the AKAC values determined in the previous analysis, where PLA samples with reduced infill densities showed the lowest values and stone- and metal-filled material samples the highest values. The CT density of the metal filaments stainless steel and copperfil exceed the HU scale with CT densities higher than 3000 HU and are therefore not shown in the diagram. Additionally, these samples lead to extensive artefacts in the CT images.

In principle, the findings of the previous analysis are confirmed when comparing the CT densities of material samples and human tissues. However, reference values for CT densities of human tissues are much broader defined than the reference values received from the tissue compositions summarized in Tab. 3.2. For example, for cortical bones, a wide range of CT densities occur naturally in human bodies. The lower area of this range is covered by stone-filled materials and resin mixtures with 40 and 50 % hydroxyapatite. However, CT densities higher than 1000 HU and lower than 2000 HU, as they occur for some bone regions, are not covered by any material. According to the previous results, there is consequently no suited tissue equivalent material for this kind of bones.

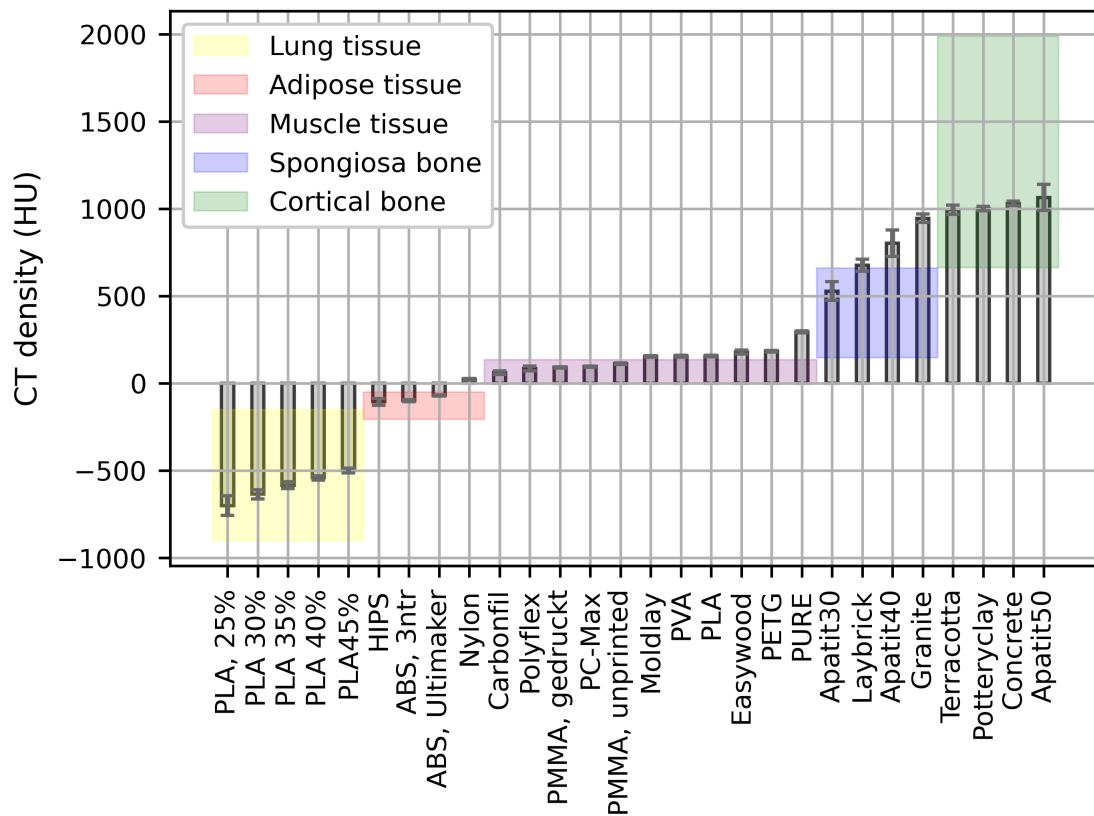


Figure 3.14: Mean CT densities for a specific ROI of the investigated materials scanned with 100 kV tube voltage and 200 mA tube current and the standard deviations. Additionally, the typical CT density ranges for adult tissues and bones are shown [101, 102].

### 3.3.4.1 Influence of printing settings on CT densities of printed samples

The results of the detailed investigations of the influence of general printing settings on the CT densities of printed samples are shown in Fig. 3.15.

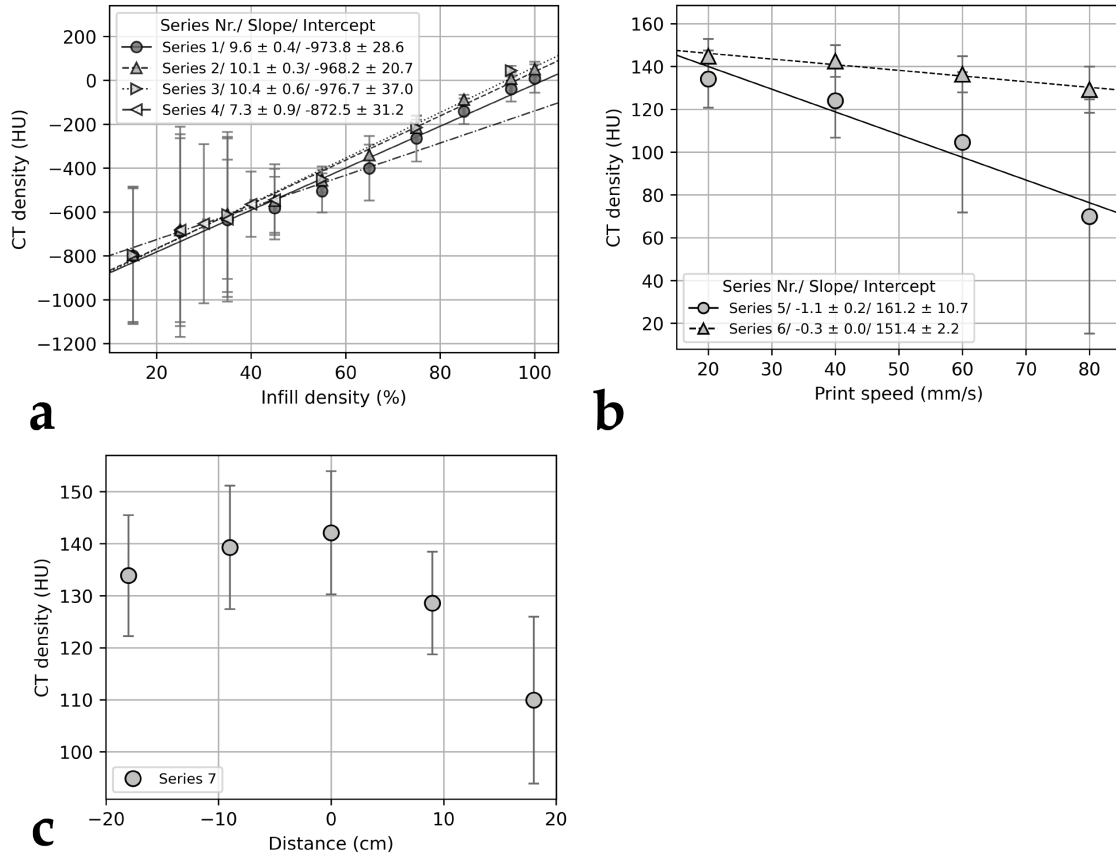


Figure 3.15: a) CT densities in dependence on the infill densities for sample series with different printing settings. b) CT densities of samples printed with 100 % infill density and two different layer heights in dependence of the print speed. c) CT densities of samples printed with 100 % infill density and 60 mm/s in dependence on the diagonal distance from the middle of the build plate. All CT densities were determined for CT scans with 100 kV tube voltage, representing mean values of an ROI. The error represents the standard deviation for the ROI. The legends give the results of the linear regression analyses.

The dependence of the CT densities from three main settings, namely the infill density, the printing speed and the position on the build plate, were investigated. In example of Series 3, the CT images are shown in Fig. 3.5. There is a systematic artefact in each cube, reasoned from the printing scheme, which starts printing the

half of the area of each layer with the innermost diagonal line. Owing to the longer hardening time there is less adhesion to the neighbour line printed as the last one in the corresponding other half of the area.

The linear relationship between CT density and the printed infill density, as found in other studies as well [75, 76], is proven again. However, the linear relationship is highly affected by the printing speed and the printing mode, as shown in Fig. 3.15 a. In the case of lower printing speeds (Series 2), the slope of a linear fit function increases while the intercept stays approximately constant. This effect is enhanced by the serial print mode (Series 3). The samples printed with the Ultimaker 2+ printer that were already investigated in the previous sections for the lung tissue equivalence (Series 4) show a linear relationship with clearly different slopes and intercepts compared to the samples printed on the 3ntr printer, which indicates the high influence of the printer itself.

Because the different printing settings affect the CT densities of samples with high infill densities the most, this effect was further quantified on samples with 100 % infill density for different printing speeds in Fig. 3.15 b. The CT densities decrease linearly with increasing print speeds. An additional influence on this effect has the printed layer height. A lower layer height is less influenced by the print speed (Series 6).

The influence of the different locations on the build plate was characterized by samples printed with 100 % infill density on a diagonal from the left top to the right bottom, as shown in Fig. 3.15 c. The sample printed on the centre position shows the highest CT density, while the values decrease on both sides of the plot for the samples printed at higher distances. This effect can be explained by the large print bed of the used printer with a calibration procedure, which is based on only one reference point in the middle of the build plate. Unfortunately, a more detailed calibration of the build plate is not provided as a standard procedure of the 3ntr printer.

### 3.4 Discussion

For a fundamental investigation of the topic of 3D-printed phantoms, the tissue equivalence of various commercially available FDM filaments was investigated in the first chapter of this thesis in order to find the most suited materials and print settings. Besides the AKACs, also absorbed doses were measured for various sam-

ple materials for a range of X-ray spectra typically used for diagnostic imaging to assess the tissue equivalence regarding attenuation and absorption behaviour. Additionally, MC simulations on relevant kinds of tissues were computed to achieve comparable reference values under the same conditions as for measurements.

The general methods were cross-validated for the example of PMMA and cortical bone with a high agreement to NIST based reference values in case of the attenuation behaviour and a high agreement to each other in case of the absorption investigations. This makes the comparison of measurements and simulations a suitable method for evaluating the tissue equivalence of printing materials.

In this process, appropriate materials were defined as tissue equivalent for lung, adipose, bulk soft tissue, skeletal muscle, cartilage and glandular tissue, and spongiosa. However, no suited material was found for cortical bone, neither for adult nor fetal cortical bone.

With the additionally investigated tissue equivalence in terms of the absorption behaviour, this study completes the knowledge about typical 3D-printable tissue equivalents, already defined in previous studies for the attenuation behaviour, e.g. PLA for muscle tissue [80, 103, 104] or ABS and Nylon for adipose tissue [82]. This way, it was proven that these materials are also suited to be used in phantoms for dosimetry measurements, besides for imaging purposes only. The same yields for the other tissue equivalents defined on this way. Examples are Moldlay and Easywood for muscle or bulk soft tissue, PETG for muscle tissue, and PVA for bulk soft tissue. For lung tissue PLA samples printed with infill densities from 40 to 45 % fulfill the conditions for tissue equivalence. Glandular tissue is very similar to the bulk soft tissue in its properties, however PMMA was found as an additional tissue equivalent material. In the case of cartilage, the composite material Pure imitates the attenuation behaviour the best, followed by PETG. Even if there was no perfect agreement for the absorption behaviour, the  $\delta$  of below 10 % might be an acceptable approximation for most cases. For spongiosa, the chalk composite material Laybrick is a tissue equivalent in both properties. Even if many different commercially available composite materials with high densities were investigated, no suited tissue equivalent was found for cortical bone because the stone-filled materials are significantly lower and metal-filled filaments significantly higher in their attenuation behaviours compared to the fetal and adult cortical bones. However, the analysis of the CT densities of the materials samples and the comparison to CT densities typically measured in human tissues showed that at least the values for bones with

lower densities are covered by the stone-filled materials.

The linear relationship [75, 76] between the infill density of printed samples and the attenuation behaviour was approved by several measurements, either by the analysis of the AKAC as well as by the analysis of CT densities. Nevertheless, some deviations from the expected behaviour in view of the mass densities were recognized during the AKAC measurement in a pencil beam setup. In addition, the orientation of the printed samples relative to the beam direction influenced the attenuation behaviour. Therefore, the infill structure has to be considered as relevant factor for the attenuation behaviour besides the mass density.

Further analysis of the influence of printing settings on the CT densities of printed samples showed that there is also a significant influence of the printing speed, the layer height and the calibration of the build plate on the attenuation behaviour of printed samples. This is especially valid for fully printed samples. The influence of the printer itself should also be mentioned. The samples produced by the two printers used in this study show distinctly different attenuation behaviours, which is also visible in the accuracy of the printed infill structure (cf. Fig. 3.1 and Fig. 3.5). It is recommended to investigate the individual influences, before starting the production of 3D-printed phantoms. In contrast, the material manufacturer and the filament's color showed no relevant influence on the attenuation behaviour of printed samples.

The large selection of tissue equivalents for bulk soft tissue and skeletal muscle is especially advantageous for producing phantoms using multi-material printing. The most relevant material is PLA, one of the most common FDM filaments, which often forms the basis of composite filaments, e.g., stone-filled filaments. For this reason, these materials have similar processing temperatures and ensure good adhesion between each other. However, when additionally printing other tissues, e.g., adipose tissue with the respective tissue equivalent materials, other soft tissue equivalent materials might be more suited because of better compatibility in the printing process. Additionally, with, e.g. Moldlay and Easywood, there are soft tissue equivalent materials with slightly different contrast properties (for samples printed with 100 % infill density). Combining them would allow minor contrast differences between different soft tissue organs in 3D-printed phantoms. This effect is also possible with partially different printing settings for a printer that allows only single materials to be processed.

Considering the uncertainties, the  $\delta$  in the relevant properties between non-composite

materials and soft tissues have no significant energy dependence. This confirms the flexible usage of those materials as tissue equivalents in printed phantoms for the total energy range investigated.

The lack of cortical bone equivalents found in previous studies was confirmed in this study [76]. Besides the significant absolute  $\delta$  between properties of materials and the cortical bone itself, a distinct energy dependence was also recognized with even larger absolute  $\delta$  of AKAC values for the lower tube voltages. This can be explained by the differences in density, but also larger differences in the elemental compositions of bones and materials. Newer approaches for the correct imitation of cortical bones, e.g. the interlace deposition of PLA and metal filaments [86], the decrease of metal filaments [77], the filling of bone cavities with plaster [105], or the self-development of special filaments [85] were not assessed in this thesis. Instead, mixtures of epoxy resin and hydroxyapatite powder were investigated. The AKAC of these mixtures are indeed in similar ranges to the stone-filled materials and, therefore, also not suited for imitating cortical bone. The amount of hydroxyapatite powder in the resin mixtures could not be further increased because no homogeneous mixture would have been reached. This shows the limitations of this method. Because processing these samples was much more complicated than printing composite materials, the latter is more recommended for phantom production. Most alternative methods for imitating cortical bones need special equipment, such as a multi-material printer or filament extruder. The development of commercially available cortical bone equivalent materials considering a realistic density and elemental composition is therefore highly recommended for easy production of more realistic bone phantoms.

In summary, this study characterized all typical thermoplastic materials suitable for FDM 3D-printing and a vast number of different composite materials in terms of attenuation and absorption properties for X-rays typically used for diagnostic imaging to find suitable tissue equivalents. This forms the basis for the production of 3D-printed phantoms.

---

## 4 Comparison of 3D-printed and conventionally produced phantom parts

The second part of this thesis is focused on a general quality assurance test of 3D-printed anthropomorphic phantom parts. For this purpose, conventional phantom parts were reproduced with an industrial FDM printer that can process three different materials in one step (3ntr A2 V4, 0.6 mm nozzles). The imaging and dosimetry properties of all phantom parts were compared in a clinical CT examination, as presented in the following. These investigations were already published elsewhere [71].

### 4.1 State of the art

There are many different approaches and concepts for producing 3D-printed phantoms for several application fields [106–108]. This shows, on the one hand, the flexibility of the method, but on the other hand, the experimental state that 3D-printed phantoms hold. Therefore, there are no guidelines regarding the used 3D-printing technologies or materials to imitate various tissues for the different fields of application. The following section gives a short overview of the most relevant concepts used in previous studies on printed phantoms for different fields of application in medical physics.

The simplest form of 3D-printed phantoms is made with the FDM-technology using only one material [109–112]. However, the anthropomorphic composition of different tissues cannot be considered this way. One solution is to print several tissue regions using the same materials and different infill densities, which is especially suited for printing lung phantoms [73, 76, 77]. Phantoms printed by multi-material FDM printing can also contain more realistic bones by using suited composite fila-

ments [113, 114]. Most of these phantoms were aimed for applications in diagnostic imaging, while some were also used for quality assurance tasks in radiotherapy [110, 112].

For phantoms with delicate structures, e.g. in the glandular tissue of the breast or for lung vessels, the SLA or Polyjet technology were more often chosen than the FDM technology because of the higher spatial resolution [115, 116].

Also, for the field of nuclear imaging, e.g. single photon emission computed tomography (SPECT) and positron emission tomography (PET), 3D-printing technologies were already used for the production of phantoms. Because the filling with radionuclide solutions is necessary for these phantoms, the favoured 3D-printing technology for this application field is the Polyjet technology that ensures the production of cavities with smooth surfaces and without any holes. For example, besides an abdomen phantom for selective internal radiotherapy [117], also individualized thyroid phantoms for  $^{131}\text{I}$  measurements [118, 119], and phantoms for quality assurance for PET imaging [120, 121] were printed this way.

For the field of motion-guided radiotherapy or four-dimensional imaging, deformable phantoms are necessary, which can be printed using flexible materials [122]. Another possibility is the separate print of the required parts and the mounting to a finished phantom afterwards [123–125].

While most of the mentioned publications were based on patient datasets, some phantoms were also designed with the view of a general quality assurance test based on conventionally produced phantoms [105, 109, 113, 114]. Those phantoms yielded high agreement with the conventionally produced ones in their imaging contrasts and geometry but were only rarely compared in their dosimetry results. Only for radiotherapy, some dosimetric studies with high accordance to therapy plans were performed on 3D-printed phantoms [110, 111, 114].

Because this thesis focuses on phantoms for diagnostic imaging, the method of choice for the phantoms produced in this thesis was the FDM-technology. Owing to the newest multi-material FDM-printer, this allows the consideration of multiple materials to represent relevant tissues with either different materials or printing settings. Now that there is no general recipe for producing those phantoms, quality assurance focusing on imaging and dosimetry properties of the phantoms produced with different material combinations or printing settings is still required to ensure the equivalence to the human body. Especially the dosimetry properties of 3D-printed phantoms were insufficiently considered in previous studies for X-rays with energies

typically used for imaging. For the reason that the comparison to conventionally produced phantoms is the most suited method for such quality assurance, the following chapter of this thesis aims to reproduce conventional anthropomorphic phantom parts and to compare them with each other regarding image contrasts and absorbed doses.

## 4.2 Materials and methods

### 4.2.1 Reproduction of a conventional anthropomorphic female thorax phantom slice and breast add-ons

The conventional CIRS atom female phantom was chosen as a reference phantom to validate methods for the production of 3D-printed phantom parts. The validation process was carried out in example of one phantom slice of the thorax and the breast add-ons to address all relevant kinds of tissues.

#### Phantom slice

As marked in the figure below, the chosen slice was located in the middle of the chest (Fig. 4.1 a). It contains four relevant tissues of the CIRS phantoms: soft tissue, lung tissue, bones and costal cartilage.

Several steps were necessary to print the phantom slice, outlined in the following and sketched in Fig. 4.1. The first step was the generation of tomographic data of the reference phantom (Fig. 4.1 b), for which, in principle, any tomographic imaging technology can be used. Consequently, the whole CIRS female phantom was scanned in a clinical CT device (GE BrightSpeed) with 120 kV tube voltage and 50 mA tube current in a helical scan mode (pitch 1.38). The images were iteratively reconstructed with a standard convolution kernel with a slice thickness of 0.625 mm. On these tomographic data, the relevant organ volumes were segmented based on the different CT densities in a segmentation software (3D Slicer [126]). For this step, the following CT density ranges were used: soft tissue (-200 to 80 HU), lungs (-800 to -200 HU), bones (450 to 1000 HU), and cartilage (80 to 200 HU). The segmented volumes were limited to the height of the relevant slice using the snipping tools included in the segmentation software. However, some overlap to the neighbour slices was left, as shown in Fig. 4.1 c. In the postprocessing step (Fig. 4.1 d), surfaces were smoothed, and the heights of all volumes were adapted to each other

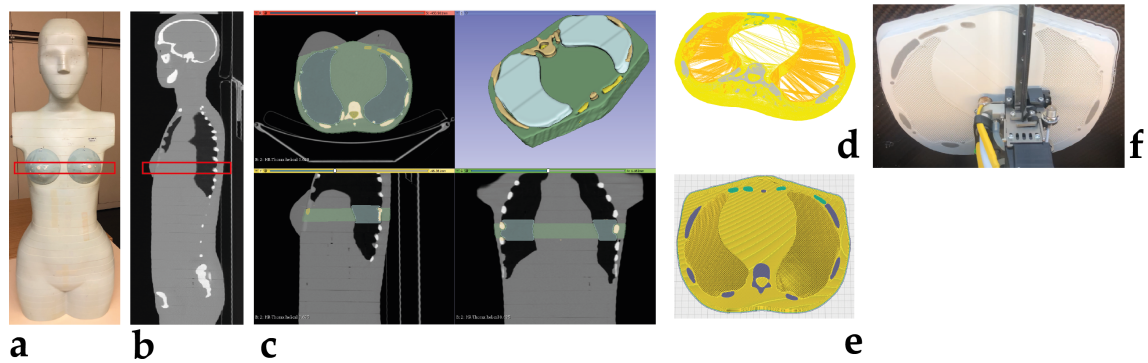


Figure 4.1: General proceeding scheme for reproducing an anthropomorphic phantom slice of a conventional female phantom (a). On a set of tomographic reference data (b) of the conventional phantom, all relevant tissues were segmented to get 3D datasets (c). Those were aligned with each other in a postprocessing step (d) and assigned to different printing materials and settings in the slicing process (e). The last step was the printing process using a multi-material FDM printer (f).

and a total thickness of 2.5 cm according to the thickness of the original phantom slice using a CAD software (Rhinoceros 7, Robert McNeel and Associates, Seattle, Washington, USA). In the next step (Fig. 4.1 e), all tissue volumes were merged and assigned to their printing materials and settings in the slicing software (Cura 4.3.0). Those settings are collected in Tab. 4.1 respectively 4.2. The individual tissues were printed with the following materials and infill densities: bones with Granite PLA (100 %), muscle with PLA (95 %), lung with PLA (30 %), and cartilage with PETG (100 %), as identified as suited tissue equivalents in the first chapter of this thesis. The reduced infill densities were printed with the same line infill style as used in the previous analyses. The whole printing step (Fig. 4.1 f) was performed in 43 hours. The material costs were 26 € in total.

Table 4.1: General printing settings for the production of the 3D-printed phantom slice and the breast add-ons.

Layer Height	Wall Line Count	Line Width	Cooling	Travelspeed
mm		mm	%	mm/s
0.2	1	0,6	100	120

Table 4.2: Individual printing settings of the FDM materials used for the production of the 3D-printed phantom slice (PLA, PETG, Granite) and the left (l) and right (r) breast add-ons (ABS, PMMA)

	<b>PLA</b> muscle	<b>PLA</b> lung	<b>PETG</b> cartilage	<b>Granite</b> bones	<b>ABS</b> adipose	<b>PMMA</b> glandular
<b>Printing speed</b> mm/s	60	60	25	60	80	80
<b>Infill density</b> %	95	30	100	100	100	100
<b>Printing temperature</b> °C	200	200	230	220	240	240
<b>Heat bed temperature</b> °C	60	60	60	60	110	110
<b>Mass of used material</b> g	864		11	80	208/167 (l/r)	47 (r)

Pins with 7 mm diameter and 2.5 cm height were printed with the same settings and materials for each tissue to realize a similar possibility for the insertion of TLDs as in the conventional CIRS phantom. Holes with a diameter of 2 mm and a depth of 7 mm were drilled in the pins to accommodate rod-shaped TLDs. This way, air gaps around the TLDs are minimized, but easy insertion and removal is still possible. Additionally, appropriate holes were drilled in the printed phantom slice to include the TLD pins at the same positions as in the conventional slice. This way, four TLDs can be located in the muscle, 10 TLDs in the lung tissue and seven inside the bones. The exact locations are marked in Fig. 4.4.

### Breast phantom add-ons

The breast add-ons were segmented in an individual step with a threshold of -100 to -10 HU on the same CT dataset as the phantom slice, as shown in Fig. 4.2 a. The conventional CIRS breast add-ons are homogeneous phantoms, imitating a mixture of 50 % adipose and 50 % glandular tissue [50]. Besides a printed homogeneous breast add-on made of adipose equivalent ABS material, the possibility of printing more realistic breast phantoms was tested in this context. For this reason, a simplified glandular structure was constructed for the right breast add-on using the CAD software Rhinoceros, as shown in Fig. 4.2 b as well. This way, the influence of a separate glandular structure on the absorbed dose can be investigated. The

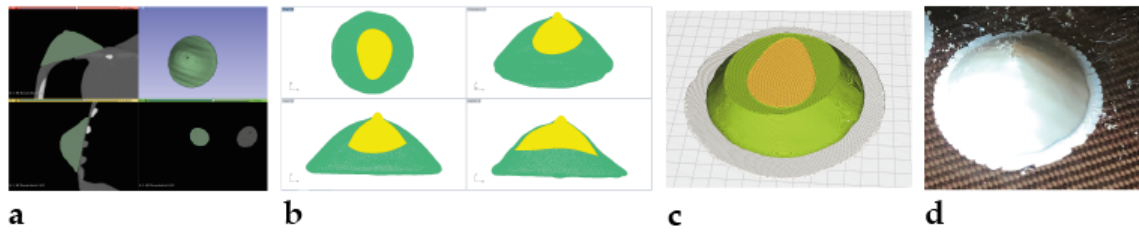


Figure 4.2: Proceeding scheme for the production of a 3D-printed breast add-on based on the conventional CIRS phantom. (a) The segmentation was performed on a CT dataset from the conventional phantom. (b) For the right breast add-on, a simplified glandular structure was constructed as a parabolic shape in the postprocessing step. (c) The respective tissue equivalent materials were assigned to both volumes in the slicing step. (d) Finally, the breast phantom was printed with a multi-material FDM printer.

glandular structure was printed with PMMA, as specified as tissue equivalent in the previous chapter. The exact printing settings of both materials are summarized in Tab. 4.2, while the general settings are shown in Tab. 4.1. For an optimal build plate adhesion, ABS needs to be printed on a raft support structure (printed with HIPS), which is visible as a white underground in Fig. 4.2c and d. This structure was removed from the finished breast phantoms. The homogeneous breast was printed in 13 hours, with total material costs of 6 €. The right breast containing the glandular structure was printed in 15 hours with material costs of 7 €. For each breast phantom, TLD pins and the corresponding holes were produced according to the description in section 4.2.1. This way, four rod-shaped TLDs can be located in each breast add-on.

#### 4.2.2 Comparison of image contrasts and absorbed doses in CT

The printed phantom parts were tested and compared with the conventional ones in terms of their imaging and dosimetry properties for a typical chest CT scan. To ensure realistic conditions for the influence of scattered photons, not only the relevant phantom slices were scanned, but a portion of the conventional CIRS phantom, including five slices of the upper chest region with the relevant phantom parts in their middle, as shown in Fig. 4.3. An adhesive tape fixated the portion of the phantom, and the printed breast add-ons were taped on the same location as the

conventional add-ons.

A typical chest CT scan on the GE Brightspeed CT scanner was performed in axial scan mode with 120 kV tube voltage, 100 mA current, and a slice thickness of 0.63 mm. For reconstruction, an iterative algorithm with a standard convolution kernel was chosen, with a remaining voxel size of  $0.7 \times 0.7 \times 0.63 \text{ mm}^3$ .

For both scans, all phantom slices (the one to be compared as well as the surrounding ones) and the breasts were filled individually with rod TLDs (TLD-100; Bicron-Harshaw). This way, the possible influence of the printed phantom slice on the dose to the other phantom slices owing to, for example, different scattering behaviours could be evaluated as well. TLD chips were attached wrapped into a foil ventral and dorsal on the phantom to measure the skin dose. The TLDs were prepared, evaluated and calibrated as described in section 3.2.4. The scans were repeated four times to collect a sufficient signal on the TLDs.

The CT densities for ROI of the relevant tissue regions in both versions of the phantom and different profiles were determined using the software ImageJ [100].

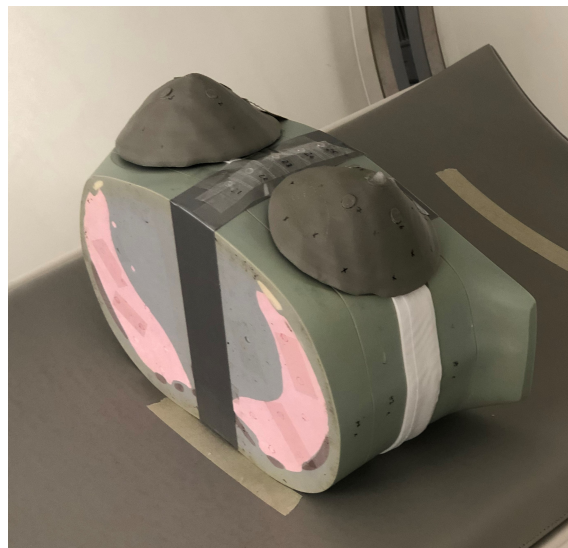


Figure 4.3: Upper chest of the CIRS phantom consisting of five phantom slices and the printed breast add-ons with the 3D-printed phantom slice in the middle. This scan was also performed with the conventionally produced phantom parts instead.

## 4.3 Results

### 4.3.1 Comparison of the geometry

Fig. 4.4 shows the printed phantom parts next to the conventionally produced ones.

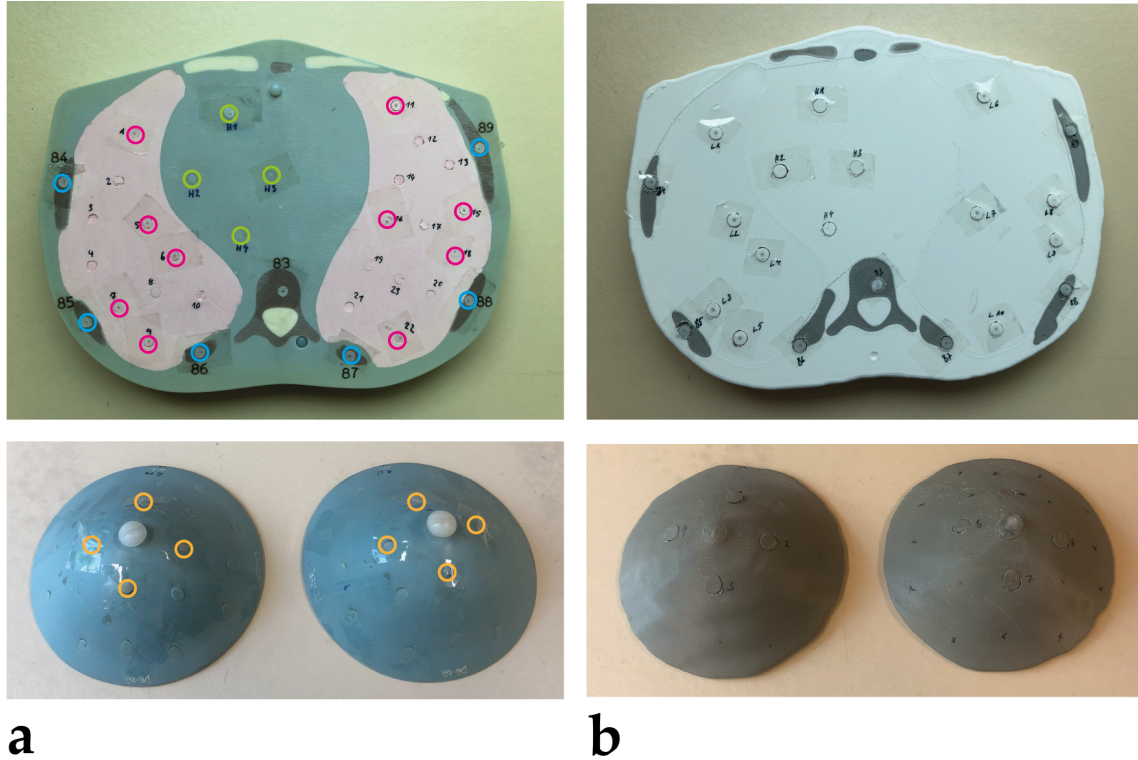


Figure 4.4: The conventional phantom slice and breast add-ons of the CIRS female phantom (a), and the 3D-printed versions (b), the left breast was printed homogeneously, and the right breast was printed with a simplified glandular structure. The positions marked in (a) are for insertion of TLDs and are available at the same location in the printed parts as well (blue=bones, red=lungs, green=muscle, yellow=breast). The printed lung structure is not visible because the phantom slice is sealed with a layer with 100% infill density.

The 3D-printed phantom slice is 5 mm larger in its circumference than the conventional one, which might be attributable to a more uneven surface of the printed phantom slice. In contrast, the printed breast add-ons are 10 mm lower in their circumference than the CIRS phantom breasts. This can be explained by the shrinking behaviour of the used ABS material [127]. The height of the printed breast add-ons is 3 mm lower, while the height of the phantom slice is exactly 2.5 cm, just as the

conventional slice.

Minor deviations are visible on the phantom slice's top and bottom plane regarding the locations and general shapes of bones and cartilage structures. These belong to difficulties in the segmentation process, which was performed on a whole-body CT scan of the conventional phantom. In this process, a manual selection of the relevant slice was necessary, which is susceptible to minor displacement errors. However, the inner structures of the phantom slice is not affected by this, as shown in the following.

As visible in Fig. 4.4b, there is an undulating structure on the printed breasts' surface and the phantom slice's outer surface. These are also part of the digital data files and are therefore attributable to the interpolation of slices on a tomographic dataset with a too high pitch factor. This effect did not affect the top and bottom surfaces of the phantom slice.

### **4.3.2 Comparison of image contrasts**

The CT images of both phantoms are shown in Fig. 4.5 next to each other with the same window settings. At the first sight, there is a good agreement between both phantoms in their contrast and geometry. The good agreement between the inner geometries is demonstrated in more detail on the subtracted difference of both images in Fig. 4.5c. Although the excellent agreement of the location of the inner structures of the phantom slices is proven, minor differences in the volumes of the lungs can be recognized as a light border. An explanation for this effect is given by the wall lines printed around the lung structures with lower infill density that are printed in the standard procedure to obtain sufficient stability. Additionally, minor differences in the breast volumes are visible that are attributable to the general lower volume reasoned in the shrinking behaviour of ABS.

Another analysis of the internal structures and their CT densities is possible by comparing the two different profiles on both CT images, which are also plotted in Fig. 4.5. Generally, both profiles validate the good geometrical agreement of the phantom parts. In the case of horizontal profile 1, which goes through soft tissue, lung tissue, and two different bone structures, as well as for the perpendicular profile 2, going through the breast, costal cartilage, lung, and soft tissue, some characteristic jags are visible inside the lung structure realized by the low infill densities. This is reasoned in the general concept of decreased infill density, for which a grid structure with undulating material deposition was printed. The soft and lung tissue wall lines

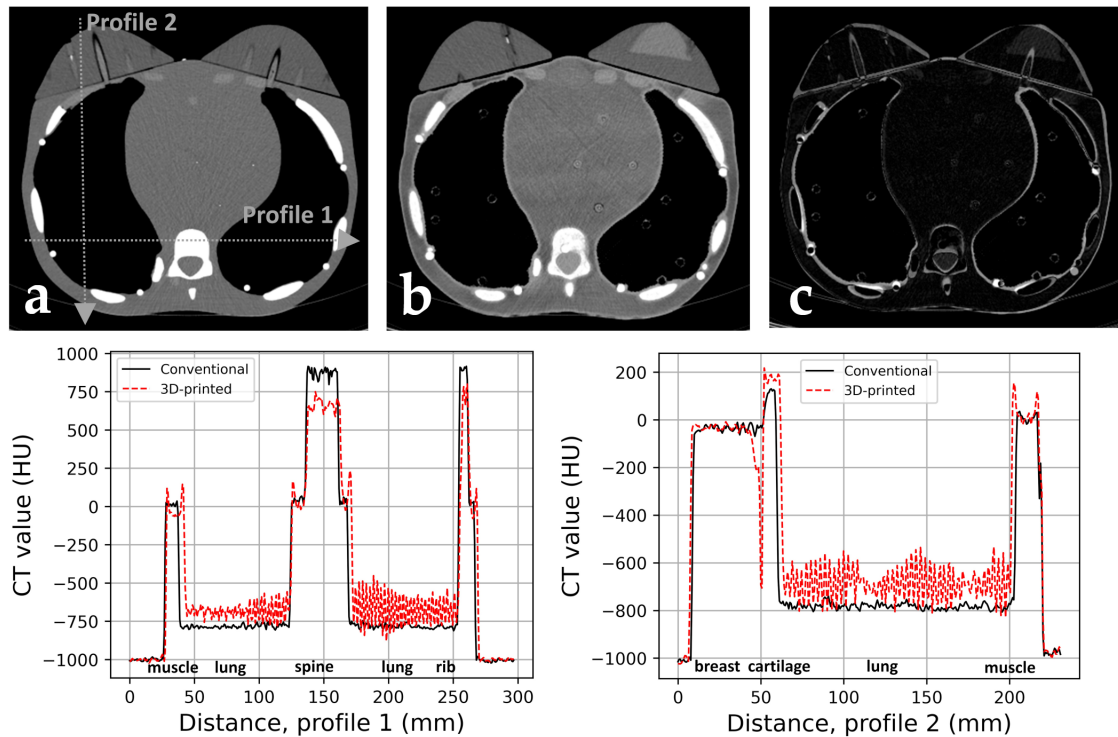


Figure 4.5: CT image of the conventionally produced phantom parts (a) and the corresponding CT image on the printed phantom parts (b) (level 100, window 1100), (c) presents the subtraction of both CT images and offers the possibility for a comparison of the inner geometry. The CT value profiles, as illustrated in (a), are summarized for both phantoms in the graphs below.

are also visible in the profiles as a sharp jag with higher CT density. There is an air gap between the 3D-printed breast add-on and the phantom slice, as visible as a sharp peak downwards in profile 2. Owing to the less smooth surface of the printed phantom parts, they cannot be located as evenly as on the conventional phantom. The mean CT densities are further compared for selected ROIs in Tab. 4.3. The mean CT densities for the printed lungs are 110 HU higher than in the conventional phantom. In contrast, the CT densities for bones are 160 HU lower. The muscle and homogeneous breast tissue show good agreement for the CT densities for both phantoms. For cartilage, the CT densities in the printed phantom are slightly higher (60 HU) than in the conventional phantom. The printed glandular tissue is, in comparison to CT densities in human glands, also slightly higher (50 HU). However, these differences are not noticeable in the CT images with the chosen window settings, as shown in Fig. 4.5. Compared to CT densities typically measured in human

tissues as provided in the literature, the other printed tissues are in a realistic range [128–131].

Table 4.3: Mean CT densities (HU) and the standard deviation of ROI for the particular kind of tissues in the conventionally produced and 3D-printed phantom parts.

Tissue	Conventional phantom parts	3D-printed phantom parts	Humans
Muscle	$20 \pm 20$	$30 \pm 25$	20 to 40 [130]
Lung	$-780 \pm 10$	$-690 \pm 80$	-500 to -900 [128]
Bones	$860 \pm 40$	$700 \pm 50$	300 to 1200 [128]
Cartilage	$-110 \pm 15$	$-170 \pm 20$	120 to 260 [129]
Adipose	$-40 \pm 10$	$-30 \pm 10$	-95 to -50 [128]
Glandular	–	$95 \pm 15$	-37 to 45 [131]

### 4.3.3 Comparison of absorbed doses

The mean doses measured with different TLDs located in the concerning tissues of in the phantom parts are shown with their standard deviation in Fig. 4.6. In Fig. 4.6 a, the mean dose to the tissues measured in the surrounding phantom slices is presented. In contrast, Fig. 4.6 b shows the mean dose for the conventionally produced and 3D-printed phantom parts themselves. This way, the influence of the printed phantom parts on the dose to the surrounding slices can also be evaluated. Actually, the mean dose to the tissues in the outer phantom slices is the same for both measurements (cf. Fig. 4.6 a), which shows that there is no relevant influence of the printed phantom parts on the scattered radiation inside the phantom.

The doses in the printed and conventionally produced phantom parts are also similar for both measurements. This applies to every kind of tissue considered. The dose to the breast add-on printed with a simplified glandular structure is not considerably different from the dose to the homogeneous breast add-on.

## 4.4 Discussion

The second part of this thesis focused on a direct comparison of 3D-printed phantom parts with conventionally produced anthropomorphic phantoms in terms of

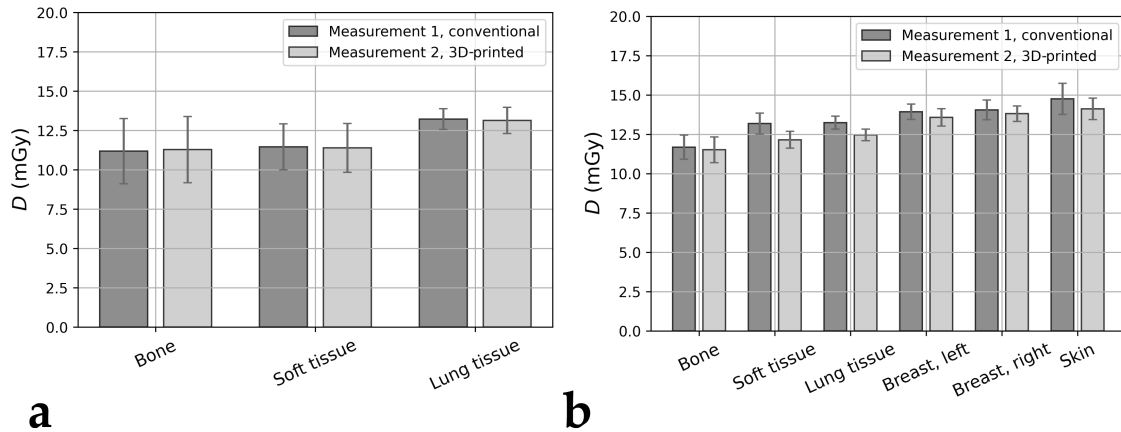


Figure 4.6: Mean doses to individual phantom regions and their standard deviations for a single CT scan. Measurement 1 represents the measurement on the phantom portion with the conventional phantom parts, measurement 2 is the one with the 3D-printed parts. a) shows the mean doses to tissues in the outer phantom slices. b) shows the mean doses to tissues in the relevant phantom parts reproduced for this study and their conventionally produced counterparts. In the right breast, a simplified glandular structure was considered, while the left one was homogeneous.

both imaging and dosimetry properties. For this reason, a phantom slice and the breast add-ons of an conventionally produced CIRS atom female phantom were reproduced under consideration of four different kinds of tissues (muscle, lung tissue, cartilage and bones). This is the next logical step for the development and evaluation of 3D-printed phantoms after the material characterization of the first chapter. While for the left breast add-on, only adipose equivalent material was considered, the right breast was produced with an additional simplified glandular structure to investigate the possibility of producing more realistic breast phantoms, as well as the influence of this structure on the absorbed dose.

All phantom parts, conventionally produced and 3D-printed ones, were subjected to a typical chest CT examination. In this process, the general good geometrical agreement of all printed parts with the original phantom parts was proven. However, the volume of printed breasts was lower than the volume of the conventionally produced breast. This can be explained by the printing material ABS, known for its warping effects after cooling [127]. One solution would be to increase the volume of the printed samples in the slicing process by the respective shrinking factor. This factor needs to be determined by the deviation of the volume of a printed test object from its 3D dataset. Alternatively, other materials, e.g. Nylon that was also found

as adipose equivalent in the previous chapter, can be tested. The warping did not affect the adhesion to PMMA for the breast add-on with the simplified glandular structure. However, it is presumable that internal adipose structures printed with ABS in anthropomorphic phantom would lead to problems. Because no adipose tissue was considered in the CIRS female phantom, this was not tested for the 3D-printed phantom slice in this study.

The CT densities of most materials considered showed a good agreement with the materials used in the conventional phantom parts, e.g. for muscle, cartilage and adipose tissue. Some larger deviations from the conventional phantom occurred only for the lung tissue and the bones. Lung tissue has a higher and bones a lower CT density in the printed version of the phantom. Both tissues have no strict range of CT densities in natural human tissues. While the CT densities of the lung depend on the breathing state and can be affected by lung diseases, for bones, the individual composition is crucial for the CT density that depends on individual bone types as well as the patient's age or gender [132]. Considering these facts, the CT densities of the CIRS phantom cannot be taken as absolute reference values and bones of both the conventional and 3D-printed phantoms have to be interpreted as simplified reconstructions with a mean composition of cortical, spongiosa, marrow, and blood. Considering the ranges of CT densities that typically occur in human bodies, the printed tissues have reasonable contrasts (cf. Fig. 3.14). Principally, there are possibilities for adjusting the printed lung density by changing the printing settings. Increasing the CT densities of printed bones is not possible in this way because it was already printed with 100 % density. For this reason, suitable composite materials are badly required, as already mentioned. Recent publications, which were not available when starting the production of the phantom parts presented in this chapter, offer promising possibilities for the production of bones by mixing different filament types [86], or by selective adjustment of infill densities for lungs [133, 134], which might be suitable for more realistic phantoms. The printed breast phantom with a simplified glandular structure showed a good contrast between adipose and glandular tissue with good adhesion between the different materials. However, more realistic glandular structures should be printed in the following.

In contrast to other studies on comparing 3D-printed phantoms to conventionally produced phantoms, this study also investigated the dose inside the phantoms by TLD measurements. The doses in both kinds of phantoms were equivalent to each other. This is valid for the relevant phantom parts themselves, as well as for the sur-

rounding phantom slices that were conventionally produced and also considered in the measurements. This shows that there is no relevant influence of the 3D-printed phantom parts on the scattering of photons. Therefore, 3D-printed phantom parts are equivalent to the conventional produced phantom parts also for the dosimetry properties, which allows a combination of printed and non-printed phantom parts. The dose in both versions of the printed breast add-ons was equivalent to each other, and consideration of glandular tissue seems to be unnecessary for this kind of examination when focusing on dosimetry purposes only.

This study investigated the method to print anthropomorphic phantom parts using a multi-material FDM printer. Most other studies used printers with at the most two different materials [85, 113, 114]. In contrast, the printer used for this study provides three print heads, which was used in this example to print soft tissues, the bones and cartilage tissue with individual materials. However, for consideration of even more kinds of tissues in a phantom, this might be a limiting factor. In other phantoms, the additional consideration of internal adipose tissue or realistic bones with cortical and spongiosa structures might be of interest. This may be solved by FDM printer able to process more than three materials at the same time. Those printers are already available, however, for higher costs. An alternative is the production of phantoms in several steps under consideration of relevant tissue regions or by a more precise adjustment of infill densities.

Another limitation of this study is that dosimetry and imaging properties of 3D-printed phantoms were only validated for a simplified representation of a human body using a conventional anthropomorphic phantom as a template. The next logical step for validation would be to produce a patient-specific phantom. However, for this case, the validation of doses is only possible with MC simulations on virtual phantoms adapted to the same patient anatomy.

---

# 5 Individualized 3D-printed phantoms

The main advantage of 3D-printing methods for the area of medical physics is the possibility to individualize phantoms to patient-specific anatomies. The following chapter of the thesis focuses on two examples of individualized phantoms. As a first example, the possibility to produce more realistic breast phantoms was further developed and tested. The second example is a phantom of the abdomen of a pregnant female based on a computational phantom, which allows the measurement of doses directly in fetal structures. These measurements were further validated by the comparison with results of Monte-Carlo simulations using the virtual pregnancy phantom. Additionally, an interindividual comparison between different pregnancy phantoms was performed.

## 5.1 State of the art

As explained in the previous chapter, various concepts for individualized 3D-printed phantoms are available, focusing on different application areas in medical physics. In the following a literature overview of studies dealing with similar topics like the ones presented in this chapter is given.

Typically, breast phantoms are produced using moulding technologies where two different materials are swirled with each other [135, 136]. However, some approaches for 3D-printed breast phantoms were also tested in the last few years. Using the Polyjet technology, the breast shell and the glands were printed, while the adipose tissue was realized with a suited filling material [115, 137]. Similar moulding techniques were used in other publications [138–140]. Combining different infill densities for the representation of the glandular and adipose tissue with one material was also successfully applied for breast phantoms using the FDM technology [141]. The printing of both kinds of breast tissues using different materials in a single step with the

multi-material FDM technology has not been considered in the literature until 2022. However, recent studies also implemented this production method successfully [134, 142]. The breast phantom produced in this thesis is still a valuable extension regarding production schemes of breast phantoms because different materials and printing settings were used.

The second example of this chapter deals with a 3D-printed phantom of a pregnant female and its validation by comparison to computational simulations with similar virtual phantoms. The cross-validation of measurements and simulations on human models was already investigated in several previous studies. While first validations were done on CTDI phantoms [143, 144], later on, comparisons of measurements in anthropomorphic phantoms, e.g. paediatric and adult CIRS phantoms or Alderson Rando phantoms, and simulations with computational phantoms considering several tissues and realistic anatomies were performed [145–148]. While in these studies the voxel phantoms are created by digitizing the respective physical phantoms, another study focused on rebuilding a physical copy of a computational phantom with milling methods [149]. Another study aimed to calculate the dose in the computational phantom at the positions where the TLDs were located in the measurements with the anthropomorphic phantom and compared the results [150]. The deviations between measured and simulated organ doses were in all these studies up to 20 %, ascribable to large uncertainties in measurement and simulation methods. With the consideration of the properties of TLDs regarding their energy or angular dependence, the differences to simulation results were lower than 10 % [149, 151].

To the best knowledge, this kind of validation was not done for 3D-printed phantoms until now. Especially for 3D-printed phantoms with individualized anatomy, such a comparison is a well-suited validation method because the same phantom can be constructed in a physical and a numerical form.

This thesis presents an anthropomorphic phantom of a pregnant woman as an example of an individualized 3D-printed phantom. Pregnant females are a crucial patient group for radiation protection because of the high sensitivity of the fetus to ionizing radiation. Because there are no commercially available anthropomorphic phantoms of pregnant females, the dose estimation for those patients is typically done by MC simulations [152–155] or by physical measurements on improvised pregnancy set-ups based on conventional anthropomorphic phantoms without any consideration of fetal structures [156–158]. Therefore, the uterus dose was used for an approximation of the fetal dose in these phantoms. Especially for the later stages of pregnancy, the

approximation of a homogeneous dose distribution inside the fetus is less accurate and the consideration of individual fetal structures would be desirable. To the best knowledge, there was no other study on a 3D-printed phantom of a pregnant female until now.

## 5.2 Production of a patient-specific breast phantom

### 5.2.1 Materials and methods

The patient-specific 3D-printed breast phantom was constructed from a clinical image set obtained with an advanced breast CT machine (AB-CT; Erlangen, Germany). This system allows tomographic imaging of the breast without compression in high resolutions (voxel size  $0.06 \times 0.06 \times 0.15 \text{ mm}^3$ , 60 kVp), and is therefore ideally suited for a realistic rendering of the breast shape and the production of 3D-printed models. The anonymized dataset of the patient was kindly provided by the radiology department of the university hospital Aachen and is shown in Fig. 5.1 a. Besides

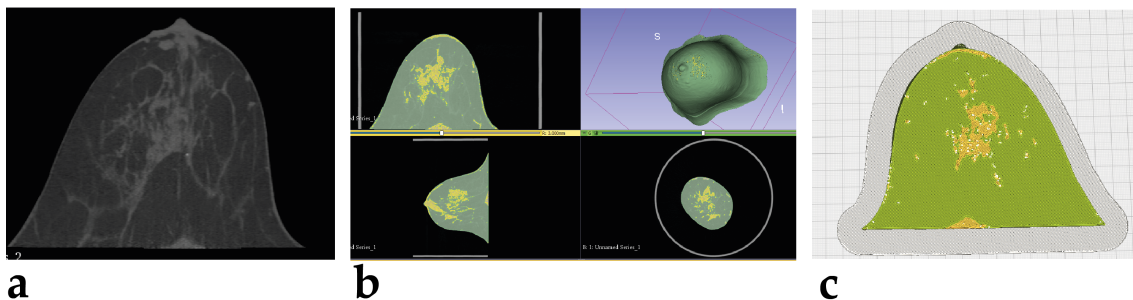


Figure 5.1: Workflow for producing a 3D-printed patient-specific breast phantom based on an advanced breast CT dataset (a). The natural adipose (green) and glandular structure (yellow) were considered in the segmentation step (b), slicing (c) and printing processes.

a non-dense glandular structure, it shows some microcalcifications and a small tumour. These were not considered in the printed phantom, because the focus of this project was on the reproduction of the glandular structure only.

The segmentation of the adipose ( $-350$  to  $-84$  HU) and glandular structure ( $-84$  to  $0$  HU) was done in the 3D Slicer software using the threshold function (Fig. 5.1 b). To keep the detailed glandular structure, no further smoothing of the object surface or image post-processing was applied. The 3D volumetric structures of both tis-

sues were merged in the Cura slicing software (Fig. 5.1 c). This step required some additional working memory capacities on the computer (32 GB) owing to the large file sizes of the detailed structures. The breast was cut longitudinally in the middle during the slicing process and printed in two steps, as shown in Fig. 5.1 c and Fig. 5.2 a. This way, it is principally possible to insert TLDs in the inner of the breast. As for the previous breast add-ons (cf. chapter 4.2.1), the adipose tissue was printed with ABS and the glandular structure with PMMA and the printing was performed with the 3ntr printer. Except for reducing the PMMA print speed to 30 mm/s, the printing settings given in Tab. 4.2 were used. The entire breast, consisting of both halves, required 820 g ABS, 77 g PMMA and as a support structure 28 g HIPS. The total material costs were 25 € and the print took 6.5 days.

In order to investigate the influence of the printing speed on the printing quality of the detailed glandular structure, a smaller sub-volume ( $2 \times 2 \times 2 \text{ cm}^3$ ) of the breast was printed with a much lower print speed (20 mm/s) for both materials, ABS and PMMA.

### 5.2.1.1 Imaging of the patient-specific breast phantom

The inner structure of the patient-specific breast phantom was imaged using a conventional CT scanner (GE BrightSpeed). Therefore, both halves of the breast phantom were combined using adhesive tape. The phantom was located with the flat bottom side on the patient couch of the scanner. An axial scan with 80 kV tube voltage (instead of 60 kV of the advanced breast CT scanner) and 300 mA was performed. This tube voltage is the lowest possible of the available scanner. The CT images were iteratively reconstructed on a standard kernel with a voxel size of  $0.41 \times 0.41 \times 1.25 \text{ mm}^3$ , which is magnitudes larger than the resolution of the patient's reference image. During this examination no dose measurement was performed.

## 5.2.2 Results

Both halves of the patient-specific breast phantom were printed without larger issues at the first try. As already visible during the printing process, some adhesion problems of PMMA on the adipose tissue printed with ABS occurred for glandular structures. This behaviour is also visible in the CT images of the printed phantom in Fig. 5.2 as small air gaps. Those occurred mainly between the finer glandular structures and the surrounding adipose tissue. The central area of the glandular

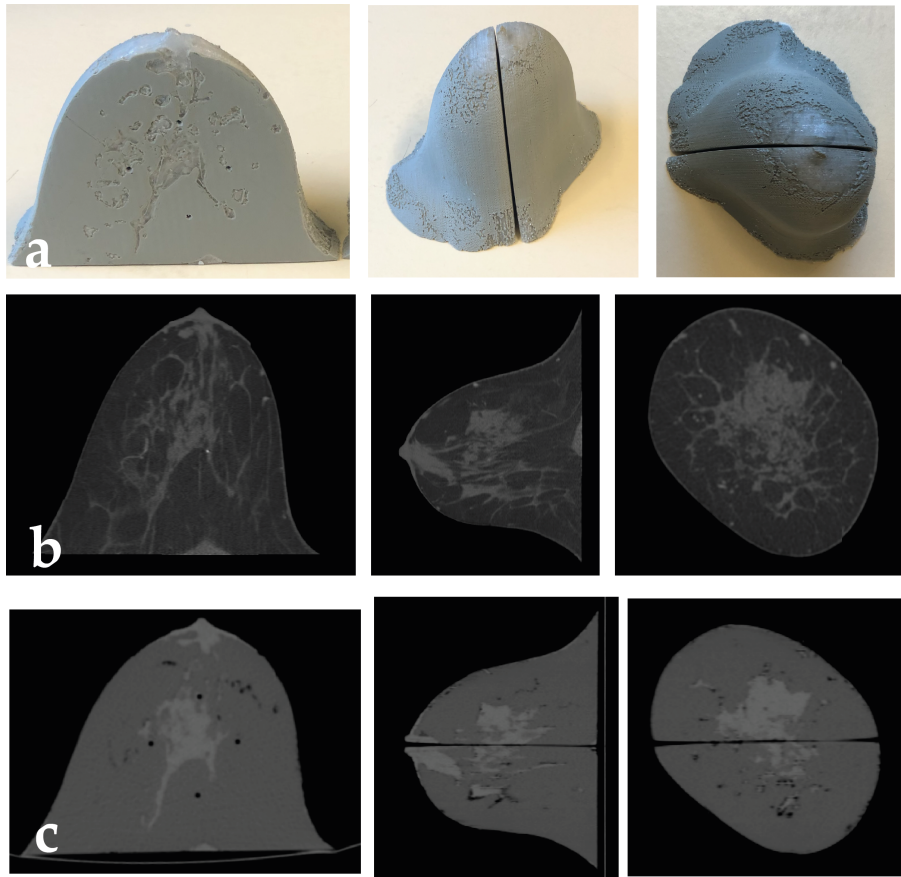


Figure 5.2: The 3D-printed patient-specific breast phantom (a), and the original patient breast CT dataset captured with 60 kV (b). c) shows the CT scan of the breast phantom captured with a classical CT device at 80 kV (The window settings for both CT image datasets are:  $W=1500$ ,  $L=250$ ). The holes in the printed breast halves represent possible locations for the insertion of rod-TLDs.

structure was printed homogeneously without any air gaps, just as the simplified glandular structure, which was printed in one of the breast add-ons for the CIRS phantom in section 4.3.2. The warping effect of ABS led to slightly curved edges at the connecting area of both patient-specific phantom halves and may have supported the bad adhesion between the two different materials. Also attributable to the warping effect is the lower height (4 mm) of the 3D-printed breast in comparison to the segmented volumes of the patient dataset.

The test print of a small volume of the internal breast tissues with a print speed of only 20 mm/s showed no significant improvement in the quality of delicate printing structures in which between also air gaps appeared.

The comparison to the original patient images is only possible on a quantitative manner because it was scanned with a different CT device (AB-CT), which allows a much higher spatial resolution and a lower tube voltage. However, the direct comparison in Fig. 5.2 shows a rough match between the reference dataset and the internal structures of the printed breast phantom. The finest glandular structures of the patient dataset were not segmented and not considered in the printing step, as shown in Fig. 5.1 b. Owing to the different X-ray spectra used for imaging, a more detailed comparison of the phantom and the patient dataset regarding the exact CT densities of adipose and glandular tissue is not possible. The CT densities of ABS and PMMA for a CT scan with 120 kV tube voltage are presented for the breast add-ons in section 4.3.2 in Tab. 4.3.

## **5.3 Production of an abdomen phantom of a female in 25. week of pregnancy**

### **5.3.1 Materials and methods**

#### **5.3.1.1 Production of the phantom add-on**

The general proceeding workflow for the production of the abdomen phantom of a pregnant female is sketched in Fig. 5.3 and outlined in the following. The template for the abdomen was given by a computational hybrid phantom of the University of Florida (Fig. 5.3 a), which is available for different weeks of gestation in a mesh and voxel version [159].

The phantom of the woman in the 25. week of gestation (named UFPF25WK in the following) was chosen to be printed because of the advanced pregnancy with a fully developed fetus and the still moderate circumference of the abdomen. Owing to the long processing time that would be necessary, not the entire mesh phantom was 3D-printed, but only the relevant abdomen region that contains the fetus. To realize the full-body phantom of a pregnant female (Fig. 5.3 c), the geometry of the pregnant torso of the computational mesh phantom was adjusted in a CAD software (Rhinoceros) to be compatible with the 3D volume of the torso of the female CIRS phantom (Fig. 5.3 b), which had been segmented in a previous step (cf. chapter 4.2.1).

The maternal bones were printed based on the segmentation of a CT scan of the

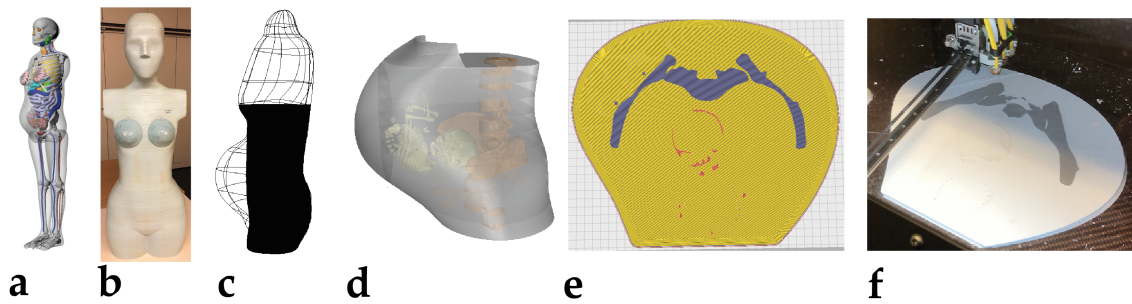


Figure 5.3: Workflow for the production of a 3D-printed abdomen add-on of a pregnant female in the 25. week of pregnancy. The abdomen of the computational mesh phantom (UFPF25WK) (a) was adjusted to the body of a conventional anthropomorphic phantom (CIRS, b) to realize a compatible phantom add-on (c, d). After the slicing step (e) the slices of the abdominal phantom were printed under consideration of soft tissue as well as maternal and fetal skeletal structures (f). For technical reasons, the top of the belly needed to be printed separately.

CIRS phantom, and the fetal skeleton based on the data of the computational mesh phantom. Both were considered as homogeneous structures. The fetus was located in the abdomen according to its position in the mesh phantom. The constructed 3D dataset (Fig. 5.3 d) was cut into slices in the CAD software, to allow the insertion of TLDs in the internal structures. The thickness of the individually printed slices was 1.25 cm instead of 2.5 cm like in the conventionally produced CIRS phantom, to allow a denser placement of TLDs inside the small structures of the fetus.

The phantom slices were printed (Fig. 5.3 e) with 0.6 mm nozzles on the 3ntr printer. The diameter of the abdomen exceeds the area of the printer's build plate, so the top of the abdomen needed to be printed in a separate step. Similarly, the upper part of the belly was not printed as an entire slice but as an add-on for the last CIRS thorax slice (this is shown in Fig. 5.3 d). The soft tissue was printed with PLA (Filamentworld, PLA snow white) with an infill density of 95 %, and the mothers bone with Granite PLA and 100 % infill density (Formfutura, granite), which were proven to be equal to the CIRS tissues in section 4.2.1. For the fetal skeleton, Laybrick (CC-Products) was used, which is less attenuating than the granite filament as shown in Fig. 3.7. The printed layer height was 0.2 mm and the print speed for PLA and granite 60 mm/s, while Laybrick was printed with 30 mm/s and a print temperature of 190 °C. The print temperatures of the other materials are summarized

in Tab. 4.2. For all slices of the printed phantom add-on 18.9 kg PLA, 1.5 kg granite and 55 g Laybrick were used. The total material costs were 582 €. The total net print time was 30 days, without considering cooling time and post-processing steps. In order to save several working steps, holes of 2 mm diameter and 8 mm depth for the accommodation of TLD rods were directly drilled into the phantom slices, instead of printing TLD pins as described in the previous chapter (cf. section 4.2.1). The proper locations of TLDs for maternal organs were estimated by a comparison with the organ location in the computational phantom of the University Florida. For the fetus, only organs clearly recognizable through the skeletal structure, e.g. the eyes or the brain, were equipped with allocations for TLDs. Other fetal organs and tissues are difficult to differentiate in the phantom due to their size and position in the womb and could allocate no more than one TLD, if any. For this reason, the dose measured with the TLDs positioned in different locations in the fetal body was averaged under a generic value termed "residual fetal tissues". In total, 105 different TLDs can be located inside the printed abdomen add-on in maternal and fetal organs.

### 5.3.1.2 Whole-body CT examination on the physical phantom of a pregnant female

In order to investigate the dose of a pregnant patient for the scenario of a trauma CT examination, a whole-body CT scan of the CIRS female phantom with the 3D-printed abdomen add-on of a pregnant female was performed. To measure the internal dose distribution, the whole phantom was filled with 248 rod-shaped LiF TLDs (TLD-100, Bicron-Harshaw). Additionally, 73 TLD chips (TLD-100, Bicron-Harshaw, rus) were wrapped into a foil and attached ventrally and dorsally on the phantoms surface to determine the skin dose. The TLDs were treated as described in chapter 3.2.4.

The examination of the phantom was performed according to clinical guidelines [160] using a clinical CT device (GE Brightspeed). The phantom, without arms, was placed with the head first on the patient table, as shown in Fig. 5.4. The total phantom was secured with adhesive tape and additional clamping devices to ensure an ideal setting of the individual phantom slices. Additionally, a soft foam material was located on the phantom's back to maintain the printed abdomen slices in the correct location. The scan was performed in helical scan mode (pitch factor of 0.56) with 120 kVp tube voltage, a slice thickness of 2.5 mm and without tube current

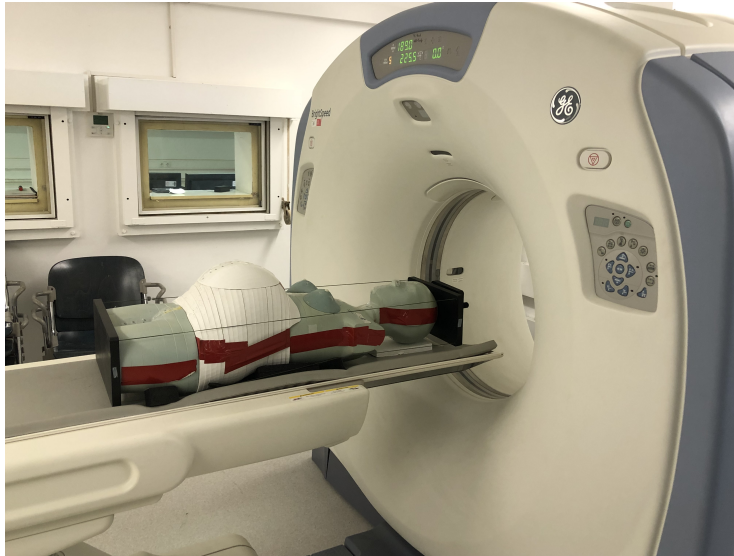


Figure 5.4: Whole-body CT examination of the physical phantom of a pregnant female, consisting of a conventional female CIRS atom phantom and a 3D-printed abdomen add-on.

modulation. Instead, the tube current was manually selected for three different body regions.

From the top of the skull to the skull base, 210 mA, from the skull base to the clavicles, 120 mA, and for the rest of the body 150 mA were used. For the first two scans, a small field of view (FOV) ( $250 \times 250 \text{ mm}^2$ ) and a head filter, and for the third scan, a large FOV ( $500 \times 500 \text{ mm}^2$ ) with a body filter was chosen. The corresponding dose parameters (e.g. the indicated CTDI-values,  $\text{CTDI}_{\text{vol}}^{\text{disp}}$ ) of each scan are summarized in Tab. 5.1.

Table 5.1: Dose parameter of the different scans of the whole-body CT examination on the physical phantom. The last column specifies the relevant CTDI phantom used to calibrate the corresponding CT protocols.

Scan	Tube Current mA	$\text{CTDI}_{\text{vol}}^{\text{disp}}$ mGy	DLP mGy · cm	Phantom
head	210	70.0	936	Head 16
neck	120	34.3	539	Head 16
body	150	21.5	1300	Body 32

Each scan was repeated eight times to get a sufficient TLD signal. Images were iteratively reconstructed with a standard convolution kernel, the remaining voxel size was  $0.5 \times 0.5 \times 1.3 \text{ mm}^3$ .

The TLD results were averaged over the respective organ regions to determine the organ doses. The effective dose was calculated following the approach described in Eq. 2.32. The organ dose for the red bone marrow was estimated by weighting the dose to the bones by the mass fraction of active bone marrow in the individual bones, as defined elsewhere [161]. The skin dose was determined by weighting the dose measured on the surface of the individual phantom slices by the approximate fraction of the slice surface to the total skin surface of the entire female phantom.

### 5.3.1.3 Simulation of the whole-body CT examination using computational phantoms

The whole-body CT examination was simulated with several computational phantoms. Using several phantoms with similar patient anatomies enables evaluating the influence of interindividual variabilities and grossly assessing the uncertainties associated with using a reference phantom. Still the simulation on the UFPF25WK phantom was mainly used for validating the 3D-printed phantom because both have the same anatomy in the abdomen region.

The simulations were performed with a MC particle transport code, originally developed at the Helmholtz Zentrum München for dose estimations in voxel phantoms for various irradiation geometries, including spiral and helical scanning in a CT setup [162, 163]. The code is based on the EGSnrc V4-2-3-0 package [164]. The correct energy spectrum of the CT device used for the measurements (GE Brightspeed) and the respective bowtie filtration, which was determined in a previous work [165], were implemented in the simulation. The energy distribution of the initial photons was obtained from the software SpekCalc using the corresponding X-ray tube settings [166].

During the simulation, the deposited energy in every voxel of the phantom was scored. Division by the mass of the respective voxel gives the deposited dose  $D$ , however, this value depends on the simulated particle fluence. Therefore, dose conversion coefficients, which are independent from the simulation parameters, were calculated by dividing the dose values by the total air kerma,  $K_{a,tot}$ , scored simultaneously on a co-rotating reference plane perpendicular to the beam direction, thus yielding the dose per air-kerma for all rotations  $\frac{D}{K_{a,tot}}$ .

To obtain a quantity  $D'$  from the simulated dose values, which can be numerically compared to the measured dose values it must be referred to a measurable quantity. Because  $K_{a,tot}$  cannot be measured during CT imaging, the chosen quantity was the  $CTDI_{vol}^{disp}$  displayed by the CT-device. For this reason, a separate simulation step was required to refer the simulated dose conversion coefficients,  $\frac{D}{K_{a,tot}}$ , to the simulated quantity  $CTDI_{vol}$ . Therefore,  $\frac{CTDI_w}{K_a}$ -values were obtained by employing a computational CTDI phantom in the simulation, i.e. a body or a head CTDI phantom, respectively. The  $CTDI_w$  is defined to be per rotation, which also applies to the  $K_a$  component of this simulation. As the simulations on voxel phantoms provide dose coefficients per air kerma integrated over all rotations,  $\frac{D}{K_{a,tot}}$  need to be multiplied by the number of rotations,  $N_R$ , to obtain doses per air kerma per rotation  $K_a$ . With that the simulated  $\frac{D_{sim}}{CTDI_w}$  are:

$$\frac{D_{sim}}{CTDI_w} = \frac{D_{sim}}{K_{a,tot}} \cdot N_R \cdot \frac{K_a}{CTDI_w}. \quad (5.1)$$

According to equation 2.22,  $CTDI_w$  is  $CTDI_{vol}$  divided by the pitch  $p$ . Therefore, the following relationship for  $\frac{D_{sim}}{CTDI_{vol}}$  is given:

$$\frac{D_{sim}}{CTDI_{vol}} = \frac{D_{sim}}{K_{a,tot}} \cdot \frac{K_a}{CTDI_w} \cdot N_R \cdot p. \quad (5.2)$$

For the quantity  $D'$ , directly comparable to the measured values, this results in:

$$D' = \frac{D_{sim}}{K_{a,tot}} \cdot \left( \frac{CTDI_w}{K_a} \right)^{-1} \cdot N_R \cdot p \cdot CTDI_{vol}^{disp}. \quad (5.3)$$

The individual dose enhancement factors, describing the additional dose in the bone marrow owing to photoelectric absorption in the surrounding trabecular bones containing high Z-materials (Ca), were considered for each bone in the simulation code [167].

Three individual scans of the different areas imaged in the CT examination on the physical phantom were simulated with the computational phantoms (each at a tube voltage of 120 kV). The simulations were performed on a Linux virtual machine (AMD EPYC 7742) with 64 cores and 128 threads with  $10^8$  initial photons. The coefficients of variance for the relevant organs were less than 0.5%. The computing time for one simulation was 40 minutes.

The organ doses were calculated as specified in Eq. 5.3 for each scan under con-

sideration of the relevant coefficients. The total organ doses for the whole-body examination were calculated by summation of the individual organ doses  $D'$  for all three scans. The effective dose was calculated for each phantom according to Eq. 2.32 under consideration of all relevant organ doses.

### Computational voxel phantoms

The three different voxel phantoms used for the simulations were: The UFPF25WK voxel phantom [159], representing a pregnant female in the 25. week of pregnancy, which was the basis of the 3D-printed abdomen add-on and is, therefore, best suited for directly validating the physical phantom; the Katja phantom [168], representing a female in the 24. pregnancy week, and the RCP-AF phantom [59], which is the official reference phantom of the ICRP that represents a non-pregnant female and forms the basis of the Katja phantom. The latter one was chosen to compare the fetal dose measured in the physical phantom to the simulated uterus dose, which is a common method for dose estimations in the early stages of pregnancy [169]. This way, general differences between fetal dose estimations using different pregnant (and non-pregnant) phantoms can be assessed, besides the general cross-validation of measurement and simulation results in the 3D-printed abdomen region of the UFPF25WK phantom. The general characteristics of all phantoms are summarized in Tab. 5.2, and all phantoms are illustrated in Fig. 5.5.

Table 5.2: Main characteristics of computational phantoms used for simulations of the whole-body CT examination.

Phantom	Height	Weight	Number of Organs	Number of Voxels	Voxel Resolution
	cm	kg			cm <sup>3</sup>
UFPF25WK <sup>a</sup>	164	65.8	260	388 × 275 × 608	1.26 × 1.26 × 2.7
Katja <sup>b</sup>	163	54	171	299 × 151 × 348	1.78 × 1.78 × 4.84
RCP-AF <sup>c</sup>	163	60	141	299 × 137 × 348	1.78 × 1.78 × 4.84

<sup>a</sup>[159]

<sup>b</sup>[168]

<sup>c</sup>[59]

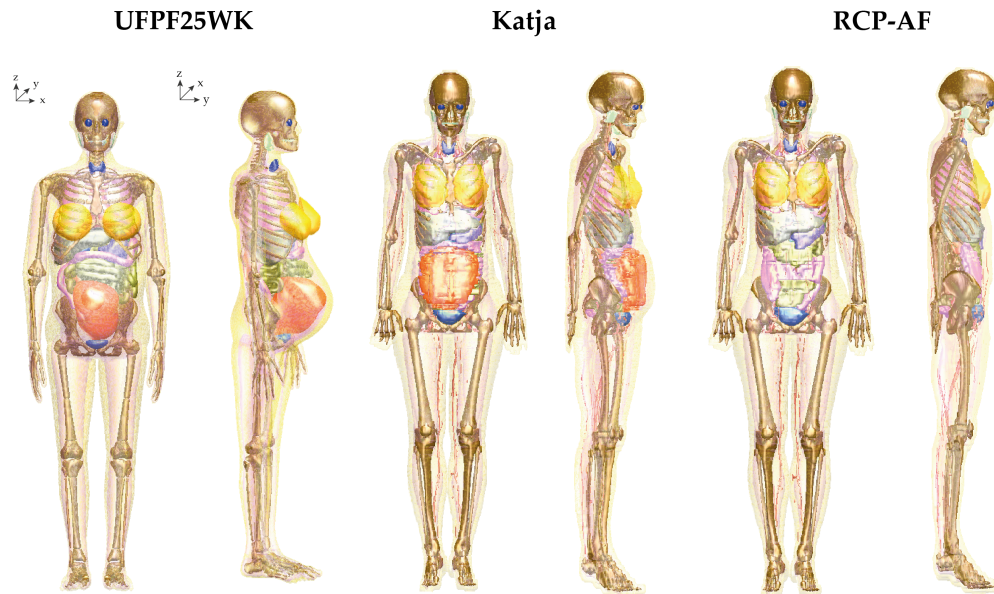


Figure 5.5: Voxel phantoms used for the whole-body CT simulation in frontal and lateral view.

Katja and the RCP-AF phantom were already implemented in the EGSnrc simulation code. In contrast, the UFPF25WK phantom was newly implemented within the scope of this thesis.

This computational phantom actually consists of two different parts: a maternal phantom where the uterus is fully filled with amniotic fluid (with a coarse voxel resolution as given in Tab. 5.2) and a separate fetus phantom with a much finer voxel resolution ( $0.04 \times 0.04 \times 0.04 \text{ cm}^3$ ). The original fetal phantom is shown in Fig. 5.6 a and the maternal phantom in Fig. 5.6 d. The resolution of the fetal phantom was reduced to the voxel resolution of the maternal phantom, as shown in Fig. 5.6 b, to be able to combine both phantoms. This step resulted in some poorly resolved organs of the fetus for which the dose estimation could be less accurate. However, for this study, no detailed dose estimation of internal fetal organs will be done but only for the entire fetal body and the fetal eyes, brain and residual tissues, like in the physical phantom. In the last step, the maternal and the fetal phantom with reduced resolution were combined to represent a complete pregnant voxel phantom, as shown in Fig. 5.6 c and e. All tissue data, i.e. elemental composition and density of the maternal and fetal phantom, were implemented with data of a 30-year-old female and a newborn [93].

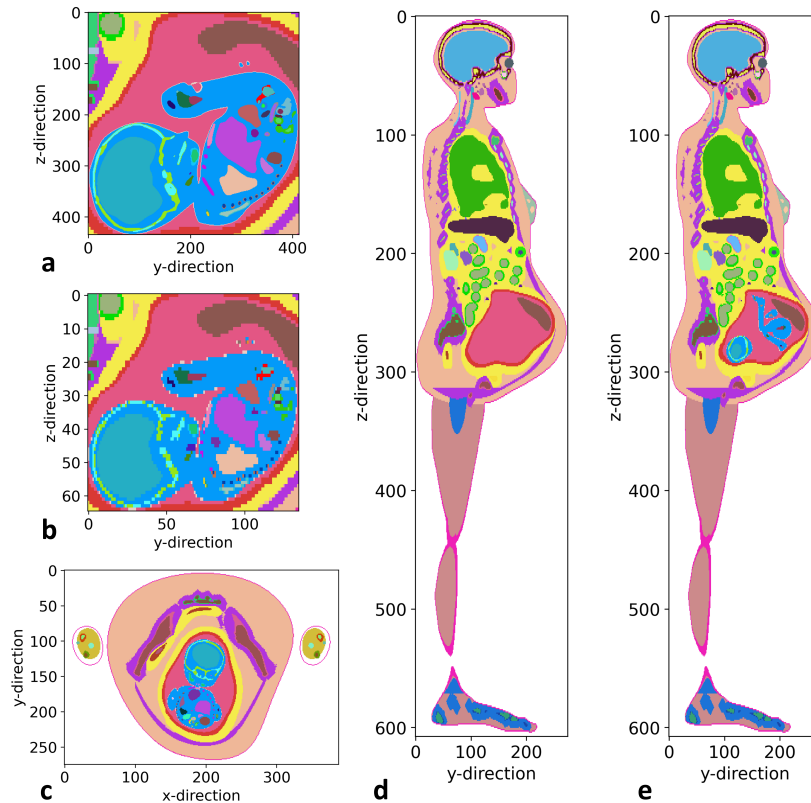


Figure 5.6: Implementation of the UFPF25WK phantom. a) Fetal phantom with fine voxel resolution. b) Fetal phantom reduced to the coarse maternal voxel resolution. c) Combined phantoms in axial view. d) Maternal phantom without fetal phantom as provided by the developers. e) Combined phantoms in lateral view. The individual colors represent different kind of tissues in the voxels.

### 5.3.2 Results

During the printing process of the various phantom slices of the abdomen add-on, some printing failures occurred, caused mainly by clogging of the printers nozzles. In these cases, the printer continued printing even if no material was flowing out of the nozzles, and decisive structures were missing in the printed slices. Principally, these mistakes can occur in any 3D-print. However, the probability is much higher when printing a large phantom consisting of multiple slices.

Apart from these technical problems, the general printing settings and chosen materials adhered well to each other and all phantom slices were printed evenly and accurately without any warping effects. The general shape of the printed abdomen add-on and a view into one slice with positions for the insertion of TLDs to measure

dose in the fetal residual tissues and brain is shown in Fig. 5.7 a.

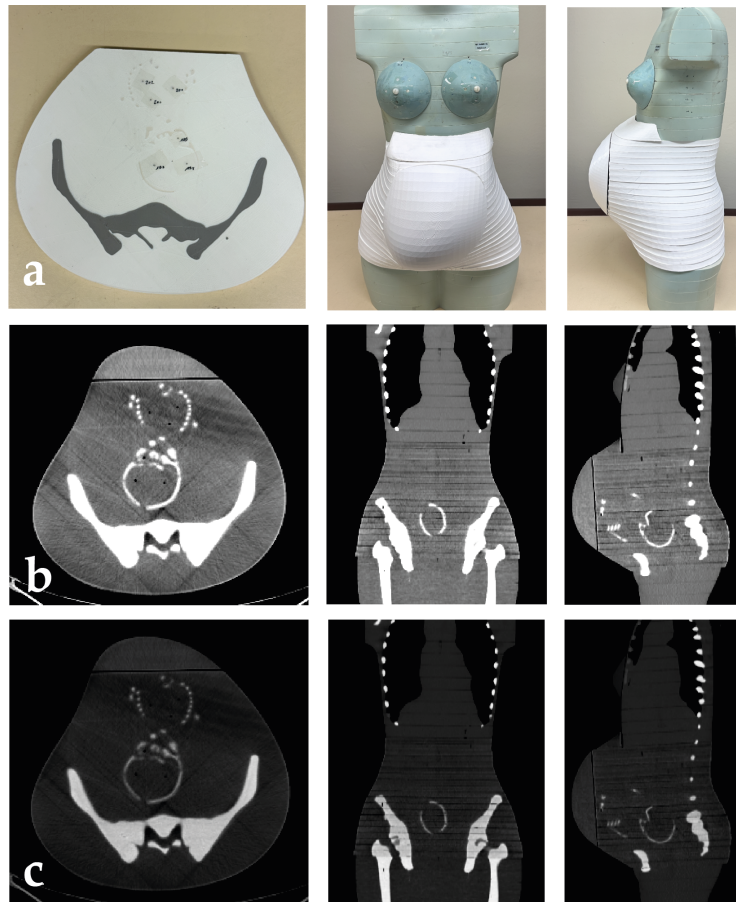


Figure 5.7: a) The 3D-printed abdomen add-on in combination with the CIRS female phantom from different views, the first shows the axial view of a phantom slice including the fetal structures and some location of TLDs in the fetal body. b) shows the phantom in multiple planes of the CT scan in the soft tissue window ( $w=350$ ,  $l=40$ ), c) shows the phantom in the bone window ( $w=1000$   $l=400$ ).

A problem with handling the finished phantom add-on is the perfect alignment of the printed top of the belly without larger gaps to the rest of the phantom, for which all slices have to be in their exact position. For technical reasons, no dowels for fixing the slices between each other were included. Instead, a support foam material adapted to the exact shape of the phantom's hollow back prevented the slipping of the slices during the CT measurement.

### 5.3.2.1 Imaging properties of the physical phantom

The CT images of the phantom of a pregnant female are shown for two different window settings (soft tissue and bone window) in Fig. 5.7 b-c. There is a good transition between the conventional CIRS phantom and the 3D-printed abdomen add-on in the geometry and in the imaging contrast of soft tissue and the bones. Slight differences between the conventional CIRS and 3D-printed bones, as they were also detected in section 4.3.2, are only visible in the bone window. The fetal skeleton has a lower contrast than the maternal bones as expected ( $530 \pm 75$  HU), representing the realistic behaviours of a lower amount of Ca in fetal bones (cf. Tab. 3.2). Even delicate fetal bone structures (Laybrick) were printed without any air gaps to the surrounding soft tissue (PLA), showing the good adhesion between both materials.

For the soft tissue, some printing artefacts are visible in the axial view on the soft tissue window. Those are caused by the movement of the print head and might be increased by smaller differences in the build plate calibration level that leads to different CT contrasts depending on the position in the phantom slice, as described in section 3.3.4.1.

### 5.3.2.2 Dose estimation for a whole-body CT examination on physical and computational phantoms

The effective doses for the mother during the whole-body CT examination determined for all considered phantoms are summarized in Tab. 5.3. Under consideration

Table 5.3: Maternal and fetal doses for the whole-body CT examination on the different kinds of phantoms. In case of the fetal dose for the RCP-AF phantom the uterus dose is given.

	Physical phantom	UFPF25WK	Katja	RCP-AF
Maternal effective dose (mSv)	$30.2 \pm 2.4$	30.4	32.1	33.9
Mean fetal dose (mGy)	$21.1 \pm 1.7$	24.3	28.7	23.4

of uncertainties for TLD measurements in anthropomorphic phantoms estimated with 8% [170], the effective doses of the physical phantom and the UFPF25WK,

as well as the Katja phantom, are equivalent to each other. In contrast, the effective dose is higher to the non-pregnant RCP-AF phantom. Uncertainties for the measurements take statistical uncertainties of the TLD readings, the energy and radiation quality dependency of the TLDs and the uncertainty of measuring organ doses only in a few reference locations of the phantom into account.

The fetal doses also provided in Tab. 5.3 give mean organ doses for the entire fetal body (calculated for the respective organ doses measured, respectively simulated), because no tissue weighting factors are defined for the fetus to calculate an effective fetal dose. The mean fetal dose estimated for the UFPF25WK phantom is slightly larger than in the physical phantom and significantly larger in the Katja phantom. This might be explained by the fact that with the computational phantoms doses were simulated and weighted in the mean fetal dose for all organs and tissues of the fetus, while in the physical phantom only the brain, the eyes and the residual tissues were considered. Estimating the fetal dose by the uterus dose of the non-pregnant RCP-AF phantom shows, in principle, a good agreement with the fetus dose of the physical phantom. However, the uterus dose of the physical pregnancy phantom itself is higher than in the RCP-AF phantom (cf. Fig. 5.8).

The individual organ doses of the physical phantom of a pregnant female are shown and compared to the simulated organ doses of the different voxel phantoms in Fig. 5.8. All organs relevant for determining the effective dose as specified in [30], were considered in the detailed comparison of the results. Therefore, relative differences,  $\delta$ , between the measured organ doses in the physical phantom and the results of simulations on the different voxel phantoms are also given in Fig. 5.8. The numerical values for organ doses are given in the Appendix in Tab. 7.2.

As recognizable in this figure the dose distribution inside the fetal body is similar in all pregnancy phantoms. Owing to the shielding of the radiation by the maternal hips, the dose to the fetal brain is lower than in the residual fetal tissues. For a validation of the dose measurements of the individualized 3D-printed phantom add-on, the measured dose values to the abdomen region (as marked by an orange box in Fig. 5.8) are compared to the simulated values on the UFPF25WK phantom. This includes the doses to the fetal body, the uterus and the urinary bladder of the mother. For these organs there is a perfect agreement between measured and simulated doses under consideration of the measurement uncertainties. This shows the high reliability of the dose estimations on individualized 3D-printed phantoms compared to a virtual phantom with the same anatomy and location of organs.

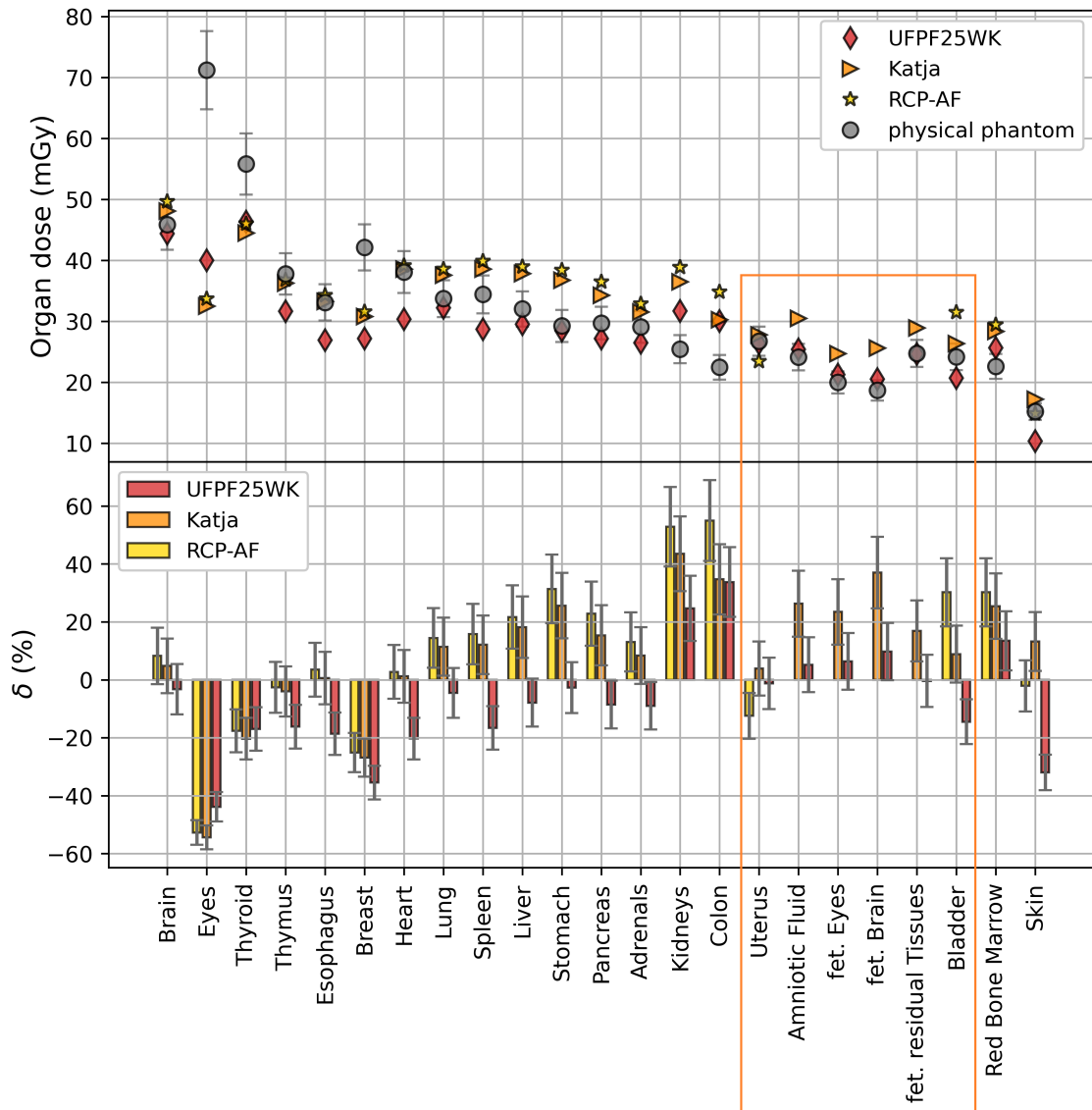


Figure 5.8: Organ doses estimated for a single whole-body CT examination during measurement on the physical phantom of a pregnant female, containing a 3D-printed abdomen add-on, and simulated for various pregnant (UFPF25WK, Katja) and non-pregnant female (RCP-AF) voxel phantoms. The relative differences,  $\delta$ , show the percentage difference of organ doses between the voxel phantoms and the physical phantom. The organs marked by the orange box show the region of the 3D-printed abdomen.

For the other organs of the mother, only the major differences will be discussed in the following. The dose to the eyes is in the physical phantom up to 60 % higher than in all voxel phantoms. This can be explained by the small volume of the eyes and the consideration of only two TLDs for the dose measurements. Because the eyes have only a small impact on the effective dose, this difference can be neglected. Similarly, the dose to the thyroid is higher in the physical phantom, which can also be explained by the small size of the organ, but also by a non-perfect central alignment of the physical phantom in the CT scanner. The thyroid and eyes are close to the body surface, and a closer distance to the X-ray tube leads to higher doses. In general, those organs have no well defined location in the body, and can deviate between the different phantoms. For the breast, the measured dose is higher than the dose in all voxel phantoms, which must therefore be owing to problems in the measurement itself, for example, the alignment of the physical phantom. With regard to the skin dose, only for the UFPF25WK phantom the simulated dose is evidently lower than the measured dose in the physical phantom. The larger deviations for the kidneys and the colon between the measurement and simulation apply to all three voxel phantoms and is attributable to the physical phantom. In the case of the kidneys, there are relevant differences in the volume covered by TLDs in the physical phantom and the actual volume of the kidneys in the voxel phantoms. Similarly, for the colon, not the whole spatial distribution of the organ as in the voxel phantoms was covered with TLDs.

A general uncertainty affecting the comparison between the simulated doses and measured doses is the  $CTDI_{vol}^{disp}$  used to convert the simulated doses to the same magnitude as measured values. This value was derived from the specification of the CT device, for which uncertainties of 20 % are tolerated. However, this would affect all simulated values equally. In this context, it should also be referred to a general problem with the UFPF25WK phantom, which was communicated unofficially by the developers. According to this statement, unlike the other organs in the abdomen, the mass of the amniotic fluid in the UFPF phantoms was not based on the reference data published in ICRP 89 [92] but on a patient dataset. This can also lead to some systematic deviations. In this study, no influence of this issue on the simulation results was noticed.

## 5.4 Discussion

The most important advantage of the method of 3D-printed anthropomorphic phantoms is the possibility of producing individualized phantoms according to the needs of specific scientific issues. In this part of the thesis, this was investigated for two kinds of phantoms.

To investigate the possibility to produce realistic breast phantoms by 3D-printing under consideration of a fine glandular structure using the previously developed method, a patient-specific breast phantom was printed based on an advanced breast CT dataset. Owing to decisive adhesive problems of the chosen materials for glandular (PMMA) and adipose tissue (ABS) some air gaps were visible in the boundary regions of both materials for the finest structures in the first version of the phantom. Even by significantly reducing the print speed, this issue could not be fixed. Therefore, the breast phantom was less realistic.

In principle, it is possible to consider another material in the breast phantoms with the available multi-material printer, e.g. for the representation of a tumour or microcalcification with a different material (e.g. a chalk-filled material for the calcifications). Especially for the latter, the adhesion problem of small structures is the main limiting factor. Another limitation factor is the spatial resolution of the 3D-printer itself, which determines how fine printed structures can be. Technically, resolutions of 50  $\mu\text{m}$  for one material are possible. However, the adhesion problems have shown that those resolutions are hardly reachable with multiple materials. Therefore, it is debatable that the multi-material FDM method is suited for producing realistic breast phantoms with acceptable quality, as it would be necessary for, e.g. quality assurance in mammography. Nevertheless, other concepts for producing realistic breast phantoms should be considered in future work, e.g., printing the relevant tissue regions in separate steps [171] or using alternative materials [142, 172]. Because dose measurements in breast phantoms with and without an additional simplified glandular structure showed no significant difference for a typical CT scan (cf. section 4.3.3), the glandular structure is, in general, not relevant for breast phantoms used for dosimetry purposes only for the investigated radiation quality (tube voltage of 120 kV).

A second example of an individualized phantom developed in this chapter of the thesis was a phantom of a pregnant female. Therefore, the phantom of the lower abdomen of a woman in the 25. week of pregnancy was developed based on volumet-

ric data of a computational hybrid phantom and produced by 3D-printing methods. By combination with the conventional CIRS female phantom, a full-body phantom of a pregnant woman was realized. For the fine structures of the fetal skeleton, no adhesion problems occurred for the chosen materials and printing settings. During the analysis of the imaging properties, a good transition between the CIRS female phantom and the printed abdomen was recognized, with only smaller differences in the bone contrast, as discussed previously. With the Laybrick material for the fetal bone structures, a good contrast to the maternal bones was realized; however, it has to be interpreted as a mixture of spongiosa and cortical bones, like the maternal bones. This also reflects the fact that there is also no cortical bone equivalent material for the fetus available (cf. section 3.3.3). The exact CT densities of fetal bones cannot be compared to literature values because image data of real pregnant patients are rarely available. In contrast to the simplified physical pregnancy phantoms used in literature [156–158], this phantom enables the fetal dose estimation for different fetal body regions. This allows, for example, a determination of the dose to the fetal brain, which is a susceptible region for effects of ionizing radiation between the 8. and 25. week of pregnancy [173].

The dose measurements in the individualized physical phantom were compared to simulations on the UFPF25WK voxel phantom, which served as a template for the 3D-printed abdomen add-on. To investigate the influence of various anatomies on the organ doses, two additional voxel phantoms, the pregnant Katja and the non-pregnant RCP-AF phantom, which both represent the ICRP reference woman, were also compared to the results on the physical CIRS phantom. A whole-body CT scan was realized in measurements and simulations, as it would have been done for a trauma patient.

The best agreement between most organ doses, as well as the effective doses of the mother, could be achieved between the physical phantom and the UFPF25WK phantom. Especially for the printed abdomen region and the dose to the fetal organs, the relative difference was below 10% and equivalent within the measurement uncertainties. This is a good validation of the 3D-printed phantom, because previous studies on the comparison of doses measured in a physical phantom by TLDs to the dose simulated in equivalent voxel phantoms yielded a similar order of magnitudes of differences [149]. In contrast, the dose to the fetus was overestimated by over 20% in the Katja phantom. The uterus dose of the RCP-AF phantom, often used for approximating the fetal dose, was underestimated in contrast to the uterus dose

of the pregnancy phantoms, but in comparison to the mean fetal dose of the physical phantom an acceptable approximation. However, the distinct dose distribution for different fetal body regions as shown in all investigated phantoms of pregnant females cannot be determined with this simplified approach. For some organs, e.g. the mother's eyes, breasts and kidneys, the doses measured in the physical phantom deviate particularly from the simulation results on all three voxel phantoms. This is attributable to the systematic deviations, reasoned in different organ segmentation on the physical phantom, or general measurement uncertainties [151].

With this study, the high quality for dose determination in individualized 3D-printed phantoms could be validated with MC simulations on voxel phantoms for applications in medical imaging. However, the CIRS component of the physical phantom was no ideal representation of any of the used voxel phantoms, leading to larger deviations in individual maternal organ doses. Considering the dose to maternal organs only and the uncertainties of measurements, the Katja phantom is a similar good approximation of the physical CIRS phantom like the UFPF25WK phantom. However, the different anatomies lead to deviations in the absolute dose values of individual organs. In general, organ dose depends on many factors, e.g. the size and the location inside the body. Because none of the phantoms represents a specific patient anatomy, organ doses measured or simulated in these phantoms can only be interpreted as a rough approximation of the real patient dose.

Until now, there are no commercially available anthropomorphic phantoms of pregnant females. Compared to the simplified realization of those phantoms in previous studies, the 3D-printed phantom add-on is a great advance [158]. Furthermore, realistic examinations with a view to imaging and dosimetry properties are possible with the realistic anatomy of the mother and the consideration of a fetal skeleton. This way, the dose to the fetus does not have to be approximated as a homogeneous dose distribution, but differences in distinct fetal organs can be estimated. Additionally, the physical pregnancy phantom can be used in the future to validate different simulations on the virtual phantoms with measurements, e.g., for technologies or devices that are not sufficiently characterized for an exact simulation.

---

## 6 Conclusion

The promising approach to improve quality assurance and radiation protection research for the application of ionizing radiation on vulnerable patient groups not adequately represented by commercially available phantoms with 3D-printed anthropomorphic phantoms tailored to individual patient anatomies was investigated in detail in this thesis. In this process, multiple relevant topics were considered for developing 3D-printed phantoms. A main focus was set on validating those phantoms by comparison to established phantoms and simulation methods for dose estimations for application in diagnostic X-ray imaging.

In the first step, conventionally available FDM filaments were studied for their tissue equivalence to give a broad overview of material characteristics and to provide a selection of well-suited materials for phantom production. In this process, suitable materials with equivalent behaviours in their attenuation and absorption of X-rays for diagnostic imaging could be found for all relevant soft tissues. The extensive influence of several printing settings on the CT density of printed objects allows an additional fine adjustment of soft tissue contrasts. However, it also shows the need for advanced investigation of the individual printing settings before the phantom production. The investigation of possible bone equivalents was done separately for two bone compositions, spongiosa and cortical bone. However, a 3D-printable equivalent was found only for the first one. For the latter, the development of composite filaments with similar compositions and densities is highly recommended to allow the consideration of cortical bone structures in realistic anthropomorphic phantoms. In summary, these investigations supplement the previous studies about the behaviours of typical FDM filaments not only regarding the attenuation but also the absorption of X-rays.

The second chapter of this thesis focused on a general validation of 3D-printed phantom parts compared to conventionally produced ones. Therefore, selected parts of a conventional phantom were reproduced using the materials defined as tissue equivalent in the first chapter of this thesis. The phantoms were directly compared in a

typical CT examination regarding image contrasts and dose measurements. In this process, the good agreement between 3D-printed and conventional phantoms was ascertained in all relevant properties. This shows that 3D-printed phantoms can be used as equivalent to conventionally produced ones.

The last topic of this thesis was the production of individualized phantoms. Besides a patient-specific breast phantom, for which some issues in the printing process were ascertained, a larger project was the production of a phantom of a pregnant female, realized by combining a 3D-printed abdomen add-on and a conventional female phantom. Besides the maternal bone structures, this phantom also considers the fetal skeleton and allows a detailed investigation of the dose inside different fetal body regions. Therefore, it is a vast improvement for experimental dose estimation for the fetus because there are, until now, no commercially available phantoms for pregnant females. Because the phantom was based on the geometry of a computational phantom of a pregnant female, a direct comparison of the dose measurements on the individualized 3D-printed phantom and the results of computational simulations on the respective computational voxel phantom could be performed for a validation step. This was done in example of a whole-body CT examination. The high quality and good agreement of measured dose distributions with simulated ones was shown in this process.

This thesis is a valuable contribution to the previous studies on the topic of 3D-printed phantoms, which were mostly focused on specific fields of application in terms of a more general point of view. Therefore, the focus was on a application of the phantoms for image quality and dose estimation purposes for a broad range of X-ray qualities typically used for diagnostic imaging. In addition, with the extended validation process, in which 3D-printed phantoms were compared with established methods for dose estimation, as measurements on conventional phantoms and MC simulations on virtual phantoms, the high quality and the promising possibilities of 3D-printed phantoms were demonstrated.

Future research should focus on a more realistic imitation of bone and lung structures, i.e. by investigating more suited infill structures that show no preferred direction for attenuation measurements, the reconstruction of more realistic vessel structures, or methods for creating realistic cortical bone contrasts. The consideration of more detailed soft tissue contrasts is also a relevant topic for the production of more realistic patient-specific phantoms or standardized phantoms, e.g., for assessment of image quality in low contrast regions. Also, for realistic breast phantoms,

more extensive tests should be done to investigate whether there are more suitable materials or printing settings. Newest publications have presented promising concepts for these issues [86, 133, 134]. Because this thesis focused on applications for X-ray imaging, similar quality assurance tests on printed phantoms need to be done for radiation qualities typically used for therapy.

In summary, this thesis proves the high quality of 3D-printed phantoms for image quality and dose measurement purposes for applications in medical imaging. This shows that 3D-printing technologies are qualified for individualized phantom production, for example, with anatomies reflecting patient groups not covered by conventional phantoms. This improves radiation protection for vulnerable groups, e.g. the fetus, because measurements can accomplish computational simulations on clinical devices and settings. Additionally, the low material costs and acceptable prices for FDM 3D-printer enable the use of anthropomorphic phantom in institutes with a small budget by investing some working hours.



---

# Bibliography

1. Booth, M. J. & Bayley, H. 3D-printed synthetic tissues. *The Biochemist* **38**, 16–19 (2016).
2. Yi, H.-G., Lee, H. & Cho, D.-W. 3D printing of organs-on-chips. *Bioengineering* **4**, 10 (2017).
3. Aimar, A., Palermo, A. & Innocenti, B. The role of 3D printing in medical applications: a state of the art. *Journal of healthcare engineering* **2019** (2019).
4. Blachowicz, T., Pająk, K., Recha, P. & Ehrmann, A. 3D printing for microsatellites-material requirements and recent developments. *AIMS Materials Science* **7** (2020).
5. Tay, Y. W. D. *et al.* 3D printing trends in building and construction industry: a review. *Virtual and Physical Prototyping* **12**, 261–276 (2017).
6. Liu, Z., Zhang, M., Bhandari, B. & Wang, Y. 3D printing: Printing precision and application in food sector. *Trends in Food Science & Technology* **69**, 83–94 (2017).
7. Su, S., Moran, K. & Robar, J. L. Design and production of 3D printed bolus for electron radiation therapy. *Journal of applied clinical medical physics* **15**, 194–211 (2014).
8. Lindsay, C *et al.* 3D printed plastics for beam modulation in proton therapy. *Physics in Medicine & Biology* **60**, N231 (2015).
9. Röntgen, W. Über eine neue Art von Strahlen: vorläufige Mitteilung. *Sitzungsbericht Phys. Med. Gesell.* (1895).
10. Friedrich, W., Knipping, P. & Laue, M. Interferenzerscheinungen bei roentgenstrahlen. *Annalen der Physik* **346**, 971–988 (1913).
11. Einstein, A. Über einem die Erzeugung und Verwandlung des Lichtes betreffenden heuristischen Gesichtspunkt. *Annalen der physik* **4** (1905).

12. Thomas, D. J. *ICRU report 85: fundamental quantities and units for ionizing radiation* 2012.
13. Seltzer, S. M. & Berger, M. J. Improved procedure for calculating the collision stopping power of elements and compounds for electrons and positrons. *The International Journal of Applied Radiation and Isotopes* **35**, 665–676 (1984).
14. Berger, M., Coursey, J., Zucker, M. & Chang, J. *ESTAR, PSTAR, and ASTAR: Computer Programs for Calculating Stopping-Power and Range Tables for Electrons, Protons, and Helium Ions* <http://physics.nist.gov/Star>. Accessed: 2022-01-18. 2005.
15. Zink, F. E. X-ray tubes. *Radiographics* **17**, 1259–1268 (1997).
16. Krieger, H. *Grundlagen der Strahlungsphysik und des Strahlenschutzes* (Springer, 2007).
17. Berger, M. J. XCOM: Photon cross section database (version 1.3) (2005).
18. Heitler, W. *The quantum theory of radiation* (Courier Corporation, 1984).
19. Klein, O. & Nishina, Y. Über die Streuung von Strahlung durch freie Elektronen nach der neuen relativistischen Quantendynamik von Dirac. *Zeitschrift für Physik* **52**, 853–868 (1929).
20. Schätzler, H. Basic aspects on the use of elastic and inelastic scattered gamma radiation for the determination of binary systems with effective atomic numbers of less than 10. *The International Journal of Applied Radiation and Isotopes* **30**, 115–121 (1979).
21. Borek, C. Antioxidants and Radiation Therapy. *The Journal of Nutrition* **134**, 3207S–3209S. ISSN: 0022-3166. <https://doi.org/10.1093/jn/134.11.3207S> (Nov. 2004).
22. Stewart, F. *et al.* ICRP publication 118: ICRP statement on tissue reactions and early and late effects of radiation in normal tissues and organs—threshold doses for tissue reactions in a radiation protection context. *Annals of the ICRP* **41**, 1–322 (2012).
23. Doessel, O. *Bildgebende Verfahren in der Medizin* (Springer Vieweg, Berlin Heidelberg, 2000).
24. Polacin, A., Kalender, W. A., Brink, J. & Vannier, M. A. Measurement of slice sensitivity profiles in spiral CT. *Medical physics* **21**, 133–140 (1994).

25. Wang, G. & Vannier, M. W. Spatial variation of section sensitivity profile in spiral computed tomography. *Medical physics* **21**, 1491–1497 (1994).
26. Radon, J. Über die Bestimmung von Funktionen längs gewisser Mannigfaltigkeiten. *Phys. Klasse, Leipzig* **69**, 262–277 (1917).
27. Schofield, R *et al.* Image reconstruction: Part 1—understanding filtered back projection, noise and image acquisition. *Journal of cardiovascular computed tomography* **14**, 219–225 (2020).
28. Hsieh, J. *et al.* Recent advances in CT image reconstruction. *Current Radiology Reports* **1**, 39–51 (2013).
29. Schlegel, W. *Medizinische Physik 2* (Springer, 2002).
30. Valentin, J. ICRP publication 103. *Ann ICRP* **37**, 2 (2007).
31. Sneha, C *et al.* ICRU report 95—Operational quantities for external radiation exposure. *Radiation Protection and Environment* **44**, 116 (2021).
32. Valentin, J. Relative biological effectiveness (RBE), quality factor (Q), and radiation weighting factor (wR): ICRP Publication 92. *Annals of the ICRP* **33**, 1–121 (2003).
33. Smith, H. ICRP publication 60. *Ann ICRP* **21** (1990).
34. Krieger, H. *Strahlenphysik, Dosimetrie und Strahlenschutz: Band 2: Strahlungsquellen, Detektoren und klinische Dosimetrie* (Springer-Verlag, 2013).
35. Pernicka, F. & McLean, I. *Dosimetry in diagnostic radiology: an international code of practice* (International Atomic Energy Agency, 2007).
36. ISO. *DIN 6800-2:2020-08: Dosismessverfahren nach der Sondenmethode für Photonen- und Elektronenstrahlung - Teil 2: Dosimetrie hochenergetischer Photonen- und Elektronenstrahlung mit Ionisationskammern* (Beuth Verlag, Berlin, 2020).
37. Petoussi-Hens, N. *et al.* Conversion Coefficients for Radiological Protection Quantities for External Radiation Exposures. *Annals of the ICRP* **40**, 1–257 (2010).
38. Gray, L. H. An ionization method for the absolute measurement of  $\gamma$ -ray energy. *Proceedings of the Royal Society of London. Series A-Mathematical and Physical Sciences* **156**, 578–596 (1936).

39. Taylor, G. & Lilley, E. The analysis of thermoluminescent glow peaks in LiF (TLD-100). *Journal of Physics D: Applied Physics* **11**, 567 (1978).
40. Buffon, G. Essai d'Arithmétique Morale. Supplement à l'Historie Naturelle. *vol 4*, 1777 (1777).
41. Metropolis, N. The beginning. *Los Alamos Science* **15**, 125–130 (1987).
42. Metropolis, N. & Ulam, S. The monte carlo method. *Journal of the American statistical association* **44**, 335–341 (1949).
43. Seco, J. & Verhaegen, F. *Monte Carlo techniques in radiation therapy* (CRC press Boca Raton, FL: 2013).
44. Bielajew, A. F. Fundamentals of the Monte Carlo method for neutral and charged particle transport. *The University of Michigan* **1** (2001).
45. Ma, C.-M. *et al.* A Monte Carlo dose calculation tool for radiotherapy treatment planning. *Physics in Medicine & Biology* **47**, 1671 (2002).
46. Mohan, R., Antolak, J. & Hendee, W. R. Monte Carlo techniques should replace analytical methods for estimating dose distributions in radiotherapy treatment planning. *Medical physics* **28**, 123–126 (2001).
47. Husby, E., Svendsen, E. D., Andersen, H. K. & Martinsen, A. C. T. 100 days with scans of the same Catphan phantom on the same CT scanner. *Journal of applied clinical medical physics* **18**, 224–231 (2017).
48. Samei, E. *et al.* Performance evaluation of computed tomography systems: summary of AAPM task group 233. *Medical physics* **46**, e735–e756 (2019).
49. Radiology Support Devices, I. *Alderson Radiation Therapy Phantom* <https://rsdphantoms.com/wp-content/uploads/2021/02/TECH-SHEET-ART-Phantom.pdf>. Accessed: 2022-02-06. 2021.
50. CIRS. *ATOM Dosimetry Phantoms* <http://www.cirsinc.com/wp-content/uploads/2019/05/701-706-ATOM-PB-120418.pdf>. Accessed: 2022-02-06. 2013.
51. White, D., Booz, J, Griffith, R., Spokas, J. & Wilson, I. ICRU Report 44: tissue substitutes in radiation dosimetry and measurement. *Journal of the International Commission on Radiation Units and Measurements* **23** (1989).

52. Kramer, R., Vieira, J., Khoury, H., Lima, F. & Fuelle, D. All about MAX: A male adult voxel phantom for Monte Carlo calculations in radiation protection dosimetry. *Physics in medicine and biology* **48**, 1239–62 (June 2003).
53. Zankl, M, Becker, J, Fill, U, Petoussi-Henss, N & Eckerman, K. GSF male and female adult voxel models representing ICRP Reference Man-the present status. *The Monte Carlo Method: Versatility Unbounded in a Dynamic Computing World* **1721** (2005).
54. Lee, C. *et al.* The UF family of reference hybrid phantoms for computational radiation dosimetry. *Physics in Medicine & Biology* **55**, 339 (2009).
55. Xu, X. G. & Eckerman, K. F. *Handbook of anatomical models for radiation dosimetry* (CRC press, 2009).
56. DeWerd, L. A. & Kissick, M. *The phantoms of medical and health physics* (Springer, 2014).
57. Snyder, W. S., Ford, M. R., Warner, G. G. & Fisher Jr, H. *Estimates of absorbed fractions for monoenergetic photon sources uniformly distributed in various organs of a heterogeneous phantom.* tech. rep. (Oak Ridge National Lab., Tenn., 1969).
58. Petoussi-Henss, N., Zankl, M., Fill, U. & Regulla, D. The GSF family of voxel phantoms. *Physics in Medicine & Biology* **47**, 89 (2001).
59. Zankl, M. Adult male and female reference computational phantoms (ICRP Publication 110). *Japanese Journal of Health Physics* **45**, 357–369 (2010).
60. Xu, X., Chao, T. & Bozkurt, A. VIP-Man: an image-based whole-body adult male model constructed from color photographs of the Visible Human Project for multi-particle Monte Carlo calculations. *Health Physics* **78**, 476–486 (2000).
61. Wong, K. V. & Hernandez, A. A review of additive manufacturing. *International scholarly research notices* **2012** (2012).
62. Hu, J. *Study on STL-based slicing process for 3D printing in 2017 International Solid Freeform Fabrication Symposium* (2017).
63. Schmidleithner, C. & Kalaskar, D. M. *Stereolithography* (IntechOpen, 2018).
64. Waheed, S. *et al.* 3D printed microfluidic devices: enablers and barriers. *Lab on a Chip* **16**, 1993–2013 (2016).

65. Stampfl, J *et al.* Photopolymers with tunable mechanical properties processed by laser-based high-resolution stereolithography. *Journal of Micromechanics and Microengineering* **18**, 125014 (2008).
66. Manapat, J. Z., Chen, Q., Ye, P. & Advincula, R. C. 3D printing of polymer nanocomposites via stereolithography. *Macromolecular Materials and Engineering* **302**, 1600553 (2017).
67. Liu, X., Zou, B., Xing, H. & Huang, C. The preparation of ZrO<sub>2</sub>-Al<sub>2</sub>O<sub>3</sub> composite ceramic by SLA-3D printing and sintering processing. *Ceramics International* **46**, 937–944 (2020).
68. Wang, X., Jiang, M., Zhou, Z., Gou, J. & Hui, D. 3D printing of polymer matrix composites: A review and prospective. *Composites Part B: Engineering* **110**, 442–458 (2017).
69. Kazemian, A., Yuan, X., Cochran, E. & Khoshnevis, B. Cementitious materials for construction-scale 3D printing: Laboratory testing of fresh printing mixture. *Construction and Building Materials* **145**, 639–647 (2017).
70. Kunert, P., Trinkl, S., Giussani, A., Reichert, D. & Brix, G. Tissue equivalence of 3D printing materials with respect to attenuation and absorption of X-rays used for diagnostic and interventional imaging. *Medical Physics* **49**, 7766–7778 (2022).
71. Kunert, P. *et al.* Reproduction of a conventional anthropomorphic female chest phantom by 3D-printing: Comparison of image contrasts and absorbed doses in CT. *Medical Physics* **50**, 4734–4743 (2023).
72. Shin, J., Sandhu, R. S. & Shih, G. Imaging properties of 3D printed materials: multi-energy CT of filament polymers. *Journal of digital imaging* **30**, 572–575 (2017).
73. Okkalidis, N., Chatzigeorgiou, C. & Okkalides, D. Assessment of 11 available materials with custom three-dimensional-printing patterns for the simulation of muscle, fat, and lung hounsfield units in patient-specific phantoms. *Journal of Engineering and Science in Medical Diagnostics and Therapy* **1** (2018).
74. Kairn, T., Crowe, S. & Markwell, T. *Use of 3D printed materials as tissue-equivalent phantoms in World Congress on Medical Physics and Biomedical Engineering, June 7-12, 2015, Toronto, Canada* (2015), 728–731.

75. Madamesila, J., McGeachy, P., Barajas, J. E. V. & Khan, R. Characterizing 3D printing in the fabrication of variable density phantoms for quality assurance of radiotherapy. *Physica Medica* **32**, 242–247 (2016).
76. Savi, M., Andrade, M. A. & Potiens, M. P. Commercial filament testing for use in 3D printed phantoms. *Radiation Physics and Chemistry* **174**, 108906 (2020).
77. Hatamikia, S. *et al.* 3D printed patient-specific thorax phantom with realistic heterogenous bone radiopacity using filament printer technology. *Zeitschrift für Medizinische Physik* (2022).
78. Dancewicz, O., Sylvander, S., Markwell, T., Crowe, S. & Trapp, J. Radiological properties of 3D printed materials in kilovoltage and megavoltage photon beams. *Physica Medica* **38**, 111–118 (2017).
79. Kaviani, F., Rashid, R. J., Shahmoradi, Z. & Gholamian, M. Detection of foreign bodies by spiral computed tomography and cone beam computed tomography in maxillofacial regions. *Journal of dental research, dental clinics, dental prospects* **8**, 166 (2014).
80. Solc, J, Vrba, T & Burianova, L. Tissue-equivalence of 3D-printed plastics for medical phantoms in radiology. *Journal of Instrumentation* **13**, P09018 (2018).
81. Villani, D, Rodrigues Jr, O & Campos, L. Dosimetric characterization of 3D printed phantoms at different infill percentages for diagnostic X-ray energy range. *Radiation Physics and Chemistry* **172**, 108728 (2020).
82. Ivanov, D. *et al.* Suitability of low density materials for 3D printing of physical breast phantoms. *Physics in Medicine & Biology* **63**, 175020 (2018).
83. Alssabbagh, M., Tajuddin, A. A., Manap, M. b. A. & Zainon, R. Evaluation of nine 3D printing materials as tissue equivalent materials in terms of mass attenuation coefficient and mass density. *International Journal of Advanced and Applied Sciences* **4**, 168–173 (2017).
84. Ceh, J. *et al.* Bismuth infusion of ABS enables additive manufacturing of complex radiological phantoms and shielding equipment. *Sensors* **17**, 459 (2017).
85. Price, G. *et al.* An open source heterogeneous 3D printed mouse phantom utilising a novel bone representative thermoplastic. *Physics in Medicine & Biology* **65**, 10NT02 (2020).

86. Tino, R., Yeo, A., Brandt, M., Leary, M. & Kron, T. The interlace deposition method of bone equivalent material extrusion 3D printing for imaging in radiotherapy. *Materials & Design* **199**, 109439 (2021).
87. Fonseca, G. P. *et al.* Dual-energy CT evaluation of 3D printed materials for radiotherapy applications. *Physics in Medicine and Biology* (2022).
88. Craft, D. F. *et al.* Material matters: analysis of density uncertainty in 3D printing and its consequences for radiation oncology. *Medical physics* **45**, 1614–1621 (2018).
89. Kontárová, S. *et al.* Printability, mechanical and thermal properties of poly (3-hydroxybutyrate)-poly (lactic acid)-plasticizer blends for three-dimensional (3D) printing. *Materials* **13**, 4736 (2020).
90. Nayak, A. K. Hydroxyapatite synthesis methodologies: an overview. *International Journal of ChemTech Research* **2**, 903–907 (2010).
91. Watanabe, Y. & Constantinou, C. Phantom materials in radiology. *Encyclopedia of medical devices and instrumentation* (2006).
92. Valentin, J. Basic anatomical and physiological data for use in radiological protection: reference values: ICRP Publication 89. *Annals of the ICRP* **32**, 1–277 (2002).
93. Bolch, W. *et al.* ICRP Publication 143: paediatric reference computational phantoms. *Annals of the ICRP* **49**, 5–297 (2020).
94. Commission, I. E. *et al.* Medical diagnostic X-ray equipment—Radiation conditions for use in the determination of characteristics. *IEC 61267* (1994).
95. ICRU. Conversion coefficients for use in radiological protection against external radiation. *ICRU Report* **57** (1998).
96. Virtanen, P. *et al.* scipy/scipy: SciPy 1.5. 3. *Zenodo* (2021).
97. Agostinelli, S. *et al.* GEANT4—a simulation toolkit. *Nuclear instruments and methods in physics research section A: Accelerators, Spectrometers, Detectors and Associated Equipment* **506**, 250–303 (2003).
98. Hernández, G. & Fernández, F. xpecgen: A program to calculate x-ray spectra generated in tungsten anodes. *J. Open Source Softw.* **1**, 62 (2016).

- 
99. White, D., Widdowson, E., Woodard, H. & Dickerson, J. The composition of body tissues.(II) Fetus to young adult. *The British journal of radiology* **64**, 149–159 (1991).
  100. Schneider, C. A., Rasband, W. S. & Eliceiri, K. W. NIH Image to ImageJ: 25 years of image analysis. *Nature methods* **9**, 671–675 (2012).
  101. Chougule, V., Mulay, A. & Ahuja, B. Clinical case study: spine modeling for minimum invasive spine surgeries (MISS) using rapid prototyping. *Bone (CT)* **226**, 3071 (2018).
  102. Morneburg, H. *Bildgebende Systeme für die medizinische Diagnostik: Röntgendiagnostik und Angiographie, Computertomographie, Nuklearmedizin, Magnetresonanztomographie, Sonographie, integrierte Informationssysteme* (Publicis MCD-Verlag, 1995).
  103. Savi, M, Potiens, M., Silveira, L., Cechinel, C., Soares, F., *et al.* Density comparison of 3D printing materials and the human body (2017).
  104. Van der Walt, M., Crabtree, T. & Albantow, C. PLA as a suitable 3D printing thermoplastic for use in external beam radiotherapy. *Australasian physical & engineering sciences in medicine* **42**, 1165–1176 (2019).
  105. Kim, S. Y., Park, J. W., Park, J., Yea, J. W. & Oh, S. A. Fabrication of 3D printed head phantom using plaster mixed with polylactic acid powder for patient-specific QA in intensity-modulated radiotherapy. *Scientific Reports* **12**, 1–10 (2022).
  106. Friedman, T., Michalski, M., Goodman, T. R. & Brown, J. E. 3D printing from diagnostic images: a radiologist’s primer with an emphasis on musculoskeletal imaging—putting the 3D printing of pathology into the hands of every physician. *Skeletal radiology* **45**, 307–321 (2016).
  107. Tino, R., Yeo, A., Leary, M., Brandt, M. & Kron, T. A systematic review on 3D-printed imaging and dosimetry phantoms in radiation therapy. *Technology in cancer research & treatment* **18**, 1533033819870208 (2019).
  108. Filippou, V. & Tsoumpas, C. Recent advances on the development of phantoms using 3D printing for imaging with CT, MRI, PET, SPECT, and ultrasound. *Medical physics* **45**, e740–e760 (2018).

109. Kamomae, T. *et al.* Three-dimensional printer-generated patient-specific phantom for artificial in vivo dosimetry in radiotherapy quality assurance. *Physica medica* **44**, 205–211 (2017).
110. Ehler, E. D., Barney, B. M., Higgins, P. D. & Dusenbery, K. E. Patient specific 3D printed phantom for IMRT quality assurance. *Physics in medicine & biology* **59**, 5763 (2014).
111. Yea, J. W. *et al.* Feasibility of a 3D-printed anthropomorphic patient-specific head phantom for patient-specific quality assurance of intensity-modulated radiotherapy. *PloS one* **12**, e0181560 (2017).
112. Craft, D. F. & Howell, R. M. Preparation and fabrication of a full-scale, sagittal-sliced, 3D-printed, patient-specific radiotherapy phantom. *Journal of applied clinical medical physics* **18**, 285–292 (2017).
113. Mille, M. M., Griffin, K. T., Maass-Moreno, R. & Lee, C. Fabrication of a pediatric torso phantom with multiple tissues represented using a dual nozzle thermoplastic 3D printer. *Journal of Applied Clinical Medical Physics* **21**, 226–236 (2020).
114. Tino, R. B., Yeo, A. U., Brandt, M., Leary, M. & Kron, T. A customizable anthropomorphic phantom for dosimetric verification of 3D-printed lung, tissue, and bone density materials. *Medical Physics* **49**, 52–69 (2022).
115. Kiarashi, N. *et al.* Development of realistic physical breast phantoms matched to virtual breast phantoms based on human subject data. *Medical physics* **42**, 4116–4126 (2015).
116. Hernandez-Giron, I., den Harder, J. M., Streekstra, G. J., Geleijns, J. & Veldkamp, W. J. Development of a 3D printed anthropomorphic lung phantom for image quality assessment in CT. *Physica Medica* **57**, 47–57 (2019).
117. Gear, J. I. *et al.* Abdo-Man: a 3D-printed anthropomorphic phantom for validating quantitative SIRT. *EJNMMI physics* **3**, 1–16 (2016).
118. Beaumont, T., Ideias, P. C., Rimlinger, M., Broggio, D. & Franck, D. Development and test of sets of 3D printed age-specific thyroid phantoms for <sup>131</sup>I measurements. *Physics in Medicine & Biology* **62**, 4673 (2017).
119. Adam, D. P. *et al.* Validation of Monte Carlo <sup>131</sup>I radiopharmaceutical dosimetry workflow using a 3D-printed anthropomorphic head and neck phantom. *Medical Physics* **49**, 5491–5503 (2022).

120. Gallivanone, F, Interlenghi, M, Canervari, C & Castiglioni, I. A fully automatic, threshold-based segmentation method for the estimation of the Metabolic Tumor Volume from PET images: validation on 3D printed anthropomorphic oncological lesions. *Journal of Instrumentation* **11**, C01022 (2016).
121. Lämpchen, T. *et al.* 3D printing of radioactive phantoms for nuclear medicine imaging. *EJNMMI physics* **7**, 1–13 (2020).
122. Shin, D.-S. *et al.* Development of a deformable lung phantom with 3D-printed flexible airways. *Medical physics* **47**, 898–908 (2020).
123. Niebuhr, N. *et al.* The ADAM-pelvis phantom—an anthropomorphic, deformable and multimodal phantom for MRgRT. *Physics in Medicine & Biology* **64**, 04NT05 (2019).
124. Jung, J. *et al.* Verification of accuracy of CyberKnife tumor-tracking radiation therapy using patient-specific lung phantoms. *International Journal of Radiation Oncology\* Biology\* Physics* **92**, 745–753 (2015).
125. Abdullah, K. A. *Optimisation of CT protocols for cardiac imaging using three-dimensional printing technology* PhD thesis (2018).
126. Pieper, S., Halle, M. & Kikinis, R. *3D Slicer* in *2004 2nd IEEE international symposium on biomedical imaging: nano to macro (IEEE Cat No. 04EX821)* (2004), 632–635.
127. Ramian, J., Ramian, J. & Dziob, D. Thermal Deformations of Thermoplast during 3D Printing: Warping in the Case of ABS. *Materials* **14**, 7070 (2021).
128. Kalra, A. in *Basic Finite Element Method as Applied to Injury Biomechanics* (ed Yang, K.-H.) 389–415 (Academic Press, 2018). ISBN: 978-0-12-809831-8.
129. Ikeda, T. Estimating age at death based on costal cartilage calcification. *The Tohoku Journal of Experimental Medicine* **243**, 237–246 (2017).
130. Lev, M. & Gonzalez, R. *Brain Mapping: The Methods* 427–484 (academic press, Dec. 2002).
131. Schneider, W., Bortfeld, T. & Schlegel, W. Correlation between CT numbers and tissue parameters needed for Monte Carlo simulations of clinical dose distributions. *Physics in Medicine & Biology* **45**, 459 (2000).
132. Batawil, N & Sabiq, S. Hounsfield unit for the diagnosis of bone mineral density disease: a proof of concept study. *Radiography* **22**, e93–e98 (2016).

133. Mei, K. *et al.* Three-dimensional printing of patient-specific lung phantoms for CT imaging: emulating lung tissue with accurate attenuation profiles and textures. *Medical physics* **49**, 825–835 (2022).
134. Okkalidis, N. & Bliznakova, K. A voxel-by-voxel method for mixing two filaments during a 3D printing process for soft-tissue replication in an anthropomorphic breast phantom. *Physics in Medicine & Biology* **67**, 245019 (2022).
135. Glick, S. J. & Ikejimba, L. C. Advances in digital and physical anthropomorphic breast phantoms for x-ray imaging. *Medical physics* **45**, e870–e885 (2018).
136. Bliznakova, K. The advent of anthropomorphic three-dimensional breast phantoms for X-ray imaging. *Physica Medica* **79**, 145–161 (2020).
137. Boita, J., Mackenzie, A., Van Engen, R. E., Broeders, M. & Sechopoulos, I. Validation of a mammographic image quality modification algorithm using 3D-printed breast phantoms. *Journal of Medical Imaging* **8**, 033502–033502 (2021).
138. He, Y. *et al.* 3D-printed breast phantom for multi-purpose and multi-modality imaging. *Quantitative imaging in medicine and surgery* **9**, 63 (2019).
139. Galstyan, A. *et al.* Applications of 3D printing in breast cancer management. *3D printing in medicine* **7**, 1–10 (2021).
140. Malliori, A., Daskalaki, A, Dermitzakis, A & Pallikarakis, N. Development of physical breast phantoms for X-ray imaging employing 3D printing techniques. *The Open Medical Imaging Journal* **12** (2020).
141. Dukov, N. *et al.* Thermoplastic 3D printing technology using a single filament for producing realistic patient-derived breast models. *Physics in Medicine & Biology* **67**, 045008 (2022).
142. Varallo, A. *et al.* Fabrication of 3D printed patient-derived anthropomorphic breast phantoms for mammography and digital breast tomosynthesis: Imaging assessment with clinical X-ray spectra. *Physica Medica* **98**, 88–97 (2022).
143. Jarry, G, DeMarco, J. J., Beifuss, U, Cagnon, C. H. & McNitt-Gray, M. F. A Monte Carlo-based method to estimate radiation dose from spiral CT: from phantom testing to patient-specific models. *Physics in Medicine and Biology* **48**, 2645–2663. <https://doi.org/10.1088/0031-9155/48/16/306> (2003).

144. Staton, R. J. *et al.* Organ and effective doses in newborn patients during helical multislice computed tomography examination. *Physics in Medicine & Biology* **51**, 5151 (2006).
145. Li, X. *et al.* Patient-specific radiation dose and cancer risk estimation in CT: part I. Development and validation of a Monte Carlo program. *Medical physics* **38**, 397–407 (2011).
146. Hoye, J. *et al.* Organ doses from CT localizer radiographs: development, validation, and application of a Monte Carlo estimation technique. *Medical physics* **46**, 5262–5272 (2019).
147. DeMarco, J. *et al.* A Monte Carlo based method to estimate radiation dose from multidetector CT (MDCT): cylindrical and anthropomorphic phantoms. *Physics in medicine & biology* **50**, 3989 (2005).
148. Fujii, K *et al.* Evaluation of organ doses in adult and paediatric CT examinations based on Monte Carlo simulations and in-phantom dosimetry. *Radiation protection dosimetry* **165**, 166–171 (2015).
149. Long, D. J. *et al.* Monte Carlo simulations of adult and pediatric computed tomography exams: validation studies of organ doses with physical phantoms. *Medical physics* **40**, 013901 (2013).
150. Fehrmann, M., Schegerer, A, Werncke, T & Schlattl, H. Comparison of experimental and numerical methods of patient dose estimations in CT using anthropomorphic models. *Radiation Protection Dosimetry* **190**, 71–83 (2020).
151. Struelens, L., Vanhavere, F. & Smans, K. Experimental validation of Monte Carlo calculations with a voxelized Rando–Alderson phantom: a study on influence parameters. *Physics in Medicine & Biology* **53**, 5831 (2008).
152. Angel, E. *et al.* Radiation dose to the fetus for pregnant patients undergoing multidetector CT imaging: Monte Carlo simulations estimating fetal dose for a range of gestational age and patient size. *Radiology* **249**, 220 (2008).
153. Kellaranta, A, Mäkelä, T, Kaasalainen, T & Kortenesniemi, M. Fetal radiation dose in three common CT examinations during pregnancy—Monte Carlo study. *Physica Medica* **43**, 199–206 (2017).

154. Gu, J., Xu, X. G., Caracappa, P. F. & Liu, B. Fetal doses to pregnant patients from CT with tube current modulation calculated using Monte Carlo simulations and realistic phantoms. *Radiation protection dosimetry* **155**, 64–72 (2013).
155. Benameur, Y., Tahiri, M., Mkimel, M., El Baydaoui, R., Mesradi, M., *et al.* Fetal organ dose assessment during pelvic CT examination using Monte Carlo/GATE simulation and pregnancy voxelized phantom Katja in *E3S Web of Conferences* **351** (2022), 01072.
156. Horowitz, D. P. *et al.* Fetal radiation monitoring and dose minimization during intensity modulated radiation therapy for glioblastoma in pregnancy. *Journal of Neuro-oncology* **120**, 405–409 (2014).
157. Labby, Z. E. *et al.* Radiation treatment planning and delivery strategies for a pregnant brain tumor patient. *Journal of applied clinical medical physics* **19**, 368–374 (2018).
158. Matsunaga, Y. *et al.* Fetal radiation dose of four tube voltages in abdominal CT examinations during pregnancy: a phantom study. *Journal of applied clinical medical physics* **22**, 178–184 (2021).
159. Maynard, M. R. *et al.* The UF Family of hybrid phantoms of the pregnant female for computational radiation dosimetry. *Physics in Medicine and Biology* **59**, 4325–4343. <https://doi.org/10.1088/0031-9155/59/15/4325> (2014).
160. Bundesärztekammer, B. Leitlinie der Bundesärztekammer zur Qualitätssicherung in der Computertomographie. *Dt. Ärzteblatt* (2022).
161. ICRP, I. Commission on Radiological Protection: Basic anatomical and physiological data for use in radiological protection: the skeleton. *ICRP-Publication* **70**.
162. Schlattl, H., Zankl, M., Becker, J. & Hoeschen, C. Dose conversion coefficients for CT examinations of adults with automatic tube current modulation. *Physics in Medicine & Biology* **55**, 6243 (2010).
163. Schlattl, H., Zankl, M., Becker, J. & Hoeschen, C. Dose conversion coefficients for paediatric CT examinations with automatic tube current modulation. *Physics in Medicine & Biology* **57**, 6309 (2012).
164. Kawrakow, I. & Rogers, D. The EGSnrc code system. *NRC Report PIRS-701*, NRC, Ottawa **17** (2000).

- 
165. Hassan, A. I., Skalej, M., Schlattl, H. & Hoeschen, C. Determination and verification of the x-ray spectrum of a CT scanner. *Journal of Medical Imaging* **5**, 013506 (2018).
166. Poludniowski, G., Landry, G., Deblois, F., Evans, P. & Verhaegen, F. SpekCalc: a program to calculate photon spectra from tungsten anode x-ray tubes. *Physics in Medicine & Biology* **54**, N433 (2009).
167. King, S. & Spiers, F. Photoelectron enhancement of the absorbed dose from X rays to human bone marrow: experimental and theoretical studies. *The british journal of radiology* **58**, 345–356 (1985).
168. Becker, J., Zankl, M., Fill, U. & Hoeschen, C. Katja—The 24th week of virtual pregnancy for dosimetric calculations. *Polish Journal of Medical Physics and Engineering* **14**, 13 (2008).
169. Osei, E., Darko, J., Faulkner, K & Kotre, C. Software for the estimation of foetal radiation dose to patients and staff in diagnostic radiology. *Journal of Radiological Protection* **23**, 183 (2003).
170. Lechel, U, Becker, C, Langenfeld-Jäger, G & Brix, G. Dose reduction by automatic exposure control in multidetector computed tomography: comparison between measurement and calculation. *European radiology* **19**, 1027–1034 (2009).
171. Dukov, N. *et al.* *Experimental evaluation of physical breast phantoms for 2D and 3D breast x-ray imaging techniques in European Medical and Biological Engineering Conference* (2020), 544–552.
172. Di Franco, F., Mettivier, G., Sarno, A., Varallo, A. & Russo, P. *Manufacturing of physical breast phantoms with 3D printing technology for X-ray breast imaging in 2019 IEEE Nuclear Science Symposium and Medical Imaging Conference (NSS/MIC)* (2019), 1–5.
173. Otake, M. & Schull, W. J. Radiation-related brain damage and growth retardation among the prenatally exposed atomic bomb survivors. *International journal of radiation biology* **74**, 159–171 (1998).



---

## 7 Appendix

Table 7.1: Print settings used for material samples for the investigation of the tissue equivalence. Some materials need a special treatment to obtain an ideal adhesion of the first print layer on the print bed (additional layer of PVA-glue).

<b>Sample name</b>	<b>Printing temperature</b> °C	<b>Build plate temperature</b> °C	<b>Printing speed</b> mm/s	<b>Additional adhesion</b>
ABS	240	100	40	yes
Carbonfil	240	60	30	no
Copperfil	220	60	30	no
Easywood	220	60	40	no
HIPS	255	110	35	no
Laybrick	190	60	30	no
Moldlay	175	30	15	no
Nylon	235	60	25	yes
PC Max	255	60	30	yes
PETG	220	75	35	yes
PLA	200	60	40	no
Polyflex	225	50	25	yes
Pure	220	65	25	no
PVA	195	50	30	yes
Concrete	200	60	35	no
Potteryclay	200	60	35	no
Granite	200	60	35	no
St. Steel	220	60	30	no
Terracotta	200	60	35	no

Table 7.2: Organ doses (mGy) obtained from measurements and simulations on a physical phantom including a 3D-printed abdomen add-on of a pregnant female and different voxel phantoms. The uncertainties for the physical phantom are given by the standard deviation of the respective TLDs, and for the virtual phantoms by the coefficient of variance.

<b>Organs</b>	<b>Physical Phantom</b>	<b>UFPF25WK</b>	<b>Katja</b>	<b>RCP-AF</b>
Brain	45.9 ± 5.9	44.3 ± 0.02	48.1 ± 0.02	49.7 ± 0.02
Eyes	71.2 ± 1.3	40.0 ± 0.1	32.5 ± 0.1	33.7 ± 0.1
Thyroid	55.8 ± 6.3	46.4 ± 0.1	44.5 ± 0.2	46.0 ± 0.2
Thymus	37.8 ± 0.6	31.7 ± 0.2	36.2 ± 0.2	36.8 ± 0.2
Esophagus	33.1 ± 1.5	26.9 ± 0.1	33.2 ± 0.1	34.2 ± 0.1
Breast	42.1 ± 1.8	27.2 ± 0.02	30.8 ± 0.03	31.5 ± 0.03
Heart	38.1 ± 3.3	30.3 ± 0.04	38.5 ± 0.03	39.1 ± 0.06
Lung	33.7 ± 3.3	32.2 ± 0.02	37.6 ± 0.03	38.6 ± 0.03
Spleen	34.4 ± 3.3	28.7 ± 0.06	38.6 ± 0.06	39.8 ± 0.07
Liver	32.0 ± 2.9	29.5 ± 0.02	37.8 ± 0.02	39.0 ± 0.02
Stomach	29.2 ± 3.6	28.5 ± 0.06	36.7 ± 0.06	38.4 ± 0.06
Pancreas	29.7 ± 0.4	27.1 ± 0.06	34.2 ± 0.06	36.5 ± 0.07
Adrenals	29.1 ± 2.1	26.5 ± 0.2	31.5 ± 0.2	32.9 ± 0.2
Kidneys	25.4 ± 3.6	31.7 ± 0.04	36.5 ± 0.04	38.9 ± 0.05
Colon	22.5 ± 2.7	30.0 ± 0.03	30.3 ± 0.03	34.8 ± 0.04
Uterus	26.8 ± 3.4	26.4 ± 0.02	27.8 ± 0.03	23.4 ± 0.06
Amniotic Fluid	24.1 ± 3.4	25.4 ± 0.02	30.5 ± 0.02	
fet. Eyes	20.0 ± 1.4	21.3 ± 0.4	24.7 ± 0.4	
fet. Brain	18.7 ± 0.9	20.5 ± 0.05	25.6 ± 0.05	
fet. residual Tissues	24.7 ± 4.1	24.6 ± 0.1	28.9 ± 0.1	
Bladder	24.2 ± 3.9	20.7 ± 0.1	26.3 ± 0.1	31.5 ± 0.1
Red Bone Marrow	22.6 ± 4.2	25.7 ± 0.02	28.4 ± 0.01	29.4 ± 0.01
Skin	15.2 ± 1.2	10.3 ± 0.01	17.2 ± 0.01	14.9 ± 0.01

---

## 8 Curriculum Vitae

### Patrizia Kunert

**Birth name:** Kruse  
**Sex:** Female  
**Nationality:** German

### Employments

**2022 - current** *Scientific officer*, Federal Office for Radiation Protection, Oberschleißheim, Germany  
**2019 - 2022** *Doctoral student*, Federal Office for Radiation Protection, Oberschleißheim, Germany

### Education

**2016 - 2018** Master of Science in medical physics, Martin-Luther-University Halle-Wittenberg  
Masters thesis: *"Implementation of new diffusion weighted magnetic resonance imaging methods"*; date of final examination 2018-10-25  
**2013 - 2016** Bachelor of Science in medical physics, Martin-Luther-University Halle-Wittenberg  
Bachelors thesis: *"Flash-DSC Untersuchungen an Lysozym"*; date of final examination 2016-09-15  
**2005 - 2013** General university entrance qualification, Gymnasium der Stadt Rahden

München, den 21. August 2023

---

Patrizia Kunert

## 8.1 List of publications

### Journal articles

Kunert, P., Schlattl, H., Trinkl, S., Giussani, A., Klein, L., Janich, M., Reichert, D., Brix, G. (2023), "Reproduction of a conventional anthropomorphic female chest phantom by 3D printing: Comparison of image contrasts and absorbed doses in CT", *Medical Physics* 50: 4734-4743, <https://doi.org/10.1002/mp.16587>

Kunert, P., Trinkl, S., Giussani, A., Reichert, D., Brix, G. (2022), "Tissue equivalence of 3D printing materials with respect to attenuation and absorption of X-rays used for diagnostic and interventional imaging", *Medical Physics* 49: 7766-7778, <https://doi.org/10.1002/mp.15987>

### Conference talks

Kunert, P. et al. (2023), "Validierung von individualisierten 3D-Druck-Phantomen am Beispiel einer CT-Untersuchung an einer schwangeren Patientin" (accepted), *DGMP Jahrestagung*, 29-09-2023, Magdeburg

Kunert, P. et al. (2022), "Comparison of 3D-printed phantom parts with a conventional anthropomorphic phantom", *European Congress of Radiology*, 07-17-2022, Vienna

Kunert, P. et al. (2021), "Evaluation of x-ray tissue-equivalence of 3D-printing materials using geant4-based reference values", *Joint conference of the ÖGMP, DGMP and SGSMP*, 09-21-2021, Vienna

### Conference posters

Kunert, P. et al. (2023), "Herstellung und Evaluation von 3D-gedruckten anthropomorphen Phantomen für Anwendungen in der diagnostischen und interventionellen Röntgenbildgebung", *SSK-Klausurtagung 2023*, 03-24-2023, Mainz

Kunert, P. et al. (2022), "An evaluation of 3D-printed anthropomorphic phantoms for diagnostic and interventional X-ray imaging", *ICRP 2021+1, 6th international symposium on the system of radiation protection 2022*, 11-10-2022, Vancouver

---

## 9 Danksagung

Diese Arbeit wurde in der Arbeitsgruppe für externe und interne Dosimetrie, Biokinetik unter der Leitung von Dr. Augusto Giussani am Bundesamt für Strahlenschutz in der Abteilung für medizinischen und beruflichen Strahlenschutz angefertigt. Die universitäre Betreuung erfolgte durch Prof. Dr. Detlef Reichert an der Martin-Luther-Universität Halle-Wittenberg.

- Mein besonderer Dank gilt Dr. Augusto Giussani, der das interessante Thema für diese Doktorarbeit bereitgestellt hat, sowie Dr. Helmut Schlattl und Sebastian Trinkl. Alle drei haben mich über die Jahre hinweg hervorragend betreut und standen immer für fachliche Diskussionen zur Verfügung. Sie haben mir nicht nur einmal bei der Lösung kleinerer und größerer Probleme geholfen.
- Herrn Prof. Dr. Gunnar Brix, Leiter der Abteilung für medizinischen und beruflichen Strahlenschutz, danke ich für die konstruktive Unterstützung bei der Veröffentlichung meiner Ergebnisse und dem großen Interesse das er meiner Arbeit stets entgegengebracht hat. Dies hat die Qualität meiner Arbeit enorm verbessert und mir die wissenschaftliche Arbeitsweise nähergebracht.
- Herrn Prof. Dr. Detlef Reichert danke ich für die gute Betreuung meiner extern durchgeführten Doktorarbeit, sowie die hilfreichen Anregungen in unseren regelmäßigen Diskussionsrunden, die mir immer eine neue Sichtweise auf Probleme gegeben haben.
- Herrn Dr. Patrick Woidy und Herrn Oliver Meisenberg danke ich für die Einführung in den 3D-Druck und die Bereitstellung des Ultimaker 3D-Druckers.
- Frau Ursula Lechel und Frau Tina Weiß danke ich für die Einführung in die Grundlagen der Thermolumineszenz-Dosimetrie und die Unterstützung bei meiner Arbeit im Labor.

- Frau Prof. Dr. Christiane Kuhl von der Klinik für diagnostische und interventionelle Radiologie des Universitätsklinikums Aachen danke ich für die freundliche Bereitstellung zahlreicher Brust-CT-Datensätze.
- Herrn Prof. Dr. Wesley Bolch und Herrn Dr. Choonsik Lee von der Universität Florida danke ich für die freundliche Bereitstellung der Phantomdatensätze.
- Herrn Maximilian Göppel, Herrn Dr. Hugo de las Heras Gala und Frau Iris Wölvitsch danke ich herzlich für das Korrekturlesen dieser Arbeit, welches der Qualität sehr zugutegekommen ist.
- Dem Bundesamt für Strahlenschutz danke ich für die Möglichkeit meine Promotion unter hervorragenden Bedingungen in einem spannenden Arbeitsumfeld durchgeführt haben zu können. Insbesondere der Arbeitsgruppe MB3 danke ich für das freundschaftliche Verhältnis.
- Nicht zu Letzt danke ich meiner Familie, besonders meinem Ehemann Moritz, für die kontinuierliche Unterstützung auf meinem Lebensweg.

---

# Eidesstattliche Erklärung

Hiermit erkläre ich, dass ich die vorliegende Doktorarbeit selbständig verfasst und keine anderen als die angegebenen Quellen und Hilfsmittel benutzt und die aus fremden Quellen direkt oder indirekt übernommenen Gedanken als solche kenntlich gemacht habe. Ich habe bisher keine vergeblichen Promotionsversuche unternommen und diese Arbeit in keinem anderen Prüfungsamt in gleicher oder vergleichbarer Form vorgelegt. Ich erkläre mich damit einverstanden, dass diese Arbeit mit Hilfe eines Plagiatserkennungsdienstes auf enthaltene Plagiate überprüft wird.

Desweiteren erkläre ich, dass gegen mich weder wegen des Verdachts einer Straftat ein gerichtliches Strafverfahren oder ein staatsanwaltliches Ermittlungsverfahren anhängig ist noch wegen eines Verbrechens oder Vergehens eine gerichtliche Bestrafung vorliegt, die Inhalt eines deutschen erweiterten Führungszeugnisses werden könnte.

München, den 21. August 2023

---

Patrizia Kunert